THE EFFECTS OF SUPPRESSION OF DILATION ON THE SHEAR STRENGTH OF SANDS

TIM HOUSE

A THESIS SUBMITTED TO
THE FACULTY OF GRADUATE STUDIES
IN PARTIAL FULFILLMENT OF THE REQUIREMENTS
FOR THE DEGREE OF
MASTER OF SCIENCE

GRADUATE PROGRAM IN CIVIL ENGINEERING
YORK UNIVERSITY
TORONTO, ONTARIO

MAY 2019

Abstract

It is known that peak angle of friction (φ'_p) for sands decreases as normal stress increases until critical state. The suppression of dilation of sands as normal stresses increase results in particle breakage, which contributes to this reduction in peak strength. There is still disagreement regarding how suppression of dilation and particle breakage affects sand's critical state angle of friction (φ'_{cs}). A total of 178 direct shear tests on three different sand types were completed to investigate the effects of suppression of dilation on the shear strength of sands, as well as effects of particle size, shape and sample size. φ'_p decreased with suppression of dilation as expected. In general, φ'_{cs} decreased by 7-9.5^o as dilation was suppressed, and was found to decrease with increasing particle size. Particle shape showed less influence on φ'_{cs} as dilation was suppressed. The effects of particle shape and sample size on φ'_{cs} were more difficult to quantify

Acknowledgements

I would first like to thank my supervisor, Dr. Jit Sharma for giving me the opportunity to complete my Masters at York University. He has given me guidance when I needed it (but not always when I wanted it), which helped me develop more independence, critical thinking, and confidence when tackling a challenging engineering problem – for this, I thank him. I would also like to thank Dr. Lal Samarasekera for his cooperation and support as a committee member. For my lab work, I owe a sincere thank you to the laboratory technician Kunjan Rupakheti for his help and support in all aspects of my lab work and during my Teaching Assistant work at York. I would like to recognize Abhi Pamnani for his support and LabView programing expertise in setting up our automatic data collection. This was a huge help, for it allowed for more efficient collection and management of the lab testing data and greatly improved the data quality. The search for natural crushable soils in the GTA proved to be more difficult than expected, and so I thank the Ministry of Transportation Ontario (MTO) for providing Kling sand that was used for this research.

Finally, I thank my Mom for encouraging me to stick with it during the difficult moments, my girlfriend Virginia for her constant support, and my friends Mariana, Seun, Rodrigo, Sebnem, Fiaz and many other of my classmates who helped support me throughout my time at York.

Table of Contents

List of Tables

List of Figures

List of Notations and Abbreviations

ASTM	American Standard for Testing and Materials
$\overline{\sigma}_t$	Average particle tensile strength (kPa)
B	Breakage index
v	Breakage parameter
B_p	Breakage potential
C_c	Coefficient of curvature
C_u	Coefficient of uniformity
A	Constant of proportionality
φ'_{cs}	Critical state friction angle based on effective stresses (^{o})
CSL	Critical state line
τ_{cs}	Critical state shear strength (kPa)
q	Deviatoric stress (kPa)
α	Dilation angle (^{o})
DSA	Direct shear apparatus
DEM	Discrete element method
F_c	Force at which crushing occurs (kN)
D	Fractal dimension
$\varphi'_{12\%}$	Friction angle at 12% shear strain (based on effective stresses) (^{o})
GAG	Gap graded
GSD	Grain size distribution
W_{crit}	Input work required for crushing to begin
ING	Intermediately graded

φ_u	Interparticle friction angle (°)
LSDS	Large scale direct shear
σ'_1	Major principal effective stress (kPa)
MGM	Manufactured granular materials
$M(L < d)$	Mass of particles with size L finer than size d
d_L	Maximum particle size (i.e. largest sieve size)
e_{max}	Maximum void ratio
p'	Mean effective stress (kPa)
d_m	Mean particle diameter
d_{50}	Mean particle diameter, or diameter corresponding to 50% finer on grain size curve
e_{min}	Minimum void ratio
MTO	Ministry of Transportation of Ontario
σ'_3	Minor principal effective stress (kPa)
φ'_m	Mobilized friction angle based on effective stresses (°)
τ_m	Mobilized shear strength (kPa)
NAG	Narrowly graded
$(\sigma'_n)_f$	Normal effective stress at failure (kPa)
ε_z	Normal strain in z (vertical) direction (mm/mm)
$N(L > d)$	Number of particle fragments with size L larger than size d
d	Particle size (i.e. sieve size opening)
σ_t	Particle tensile strength (kPa)
α_p	Peak dilation angle (°)
φ'_p	Peak friction angle based on effective stresses (°)
K_o	Principal stress ratio

W/D_{max}	Ratio of shear box width to maximum particle diameter
V_0	Reference volume
B_r	Relative breakage
γ_{zx}	Shear strain along the zx plane (mm/mm)
v_i	Slope of the initial grain size distribution in log-log scale
v_u	Slope of the ultimate grain size curve
SSDS	Small scale direct shear
G_s	Specific gravity
$P_s(V)$	Survival probability
σ_0	Tensile stress where 37% of total number of tested blocks survive (kPa).
B_t	Total breakage
M_T	Total mass of particles
USCS	Unified Soil Classificaiton System
σ_z'	Vertical effective stress (kPa)
V	Volume of block of material
m	Weibull modulus
WG	Well graded

Chapter 1 – Introduction

1.1 Motivation

Sand may contract or dilate during shear depending on its state of compaction. Reynolds (1885) was the first to determine experimentally that loose sands tend to contract, while dense sands tend to dilate during shear. Casagrande (1936) built on this by showing that regardless of soil density, soils eventually reach a critical density whereby shear stresses remain constant at a constant volume (i.e. critical state). Furthermore, Taylor (1948) discovered that sands behaved differently depending on its relative density and dilatancy. He showed that dense sands mobilize a peak shear strength followed by strain softening. He also showed that loose sands develop strain hardening until critical state, and tend not to mobilize peak strength that is larger than its critical state strength. It became evident that the relationship between soil strength and dilatancy was important in understanding soil behaviour, and became the foundation of critical state soil mechanics.

If the effective confining stress on a sand sample is large enough, the tendency for the sample to dilate during shearing becomes suppressed. Practical examples of where suppression of dilation could occur include bearing capacity failure beneath large earth dams or at the tip of a deep end-bearing pile. These large normal (confining) stresses can have a variety of effects on the stress-strain response of sand, depending upon its composition (Roscoe et al., 1958) and initial relative density (Taylor, 1948). It is well established that peak shear strength for sands, typically expressed as Coulomb's peak angle of friction (φ'_p), decreases as normal load increases until the critical state is achieved (Budhu, 2011). However, there is some disagreement among researchers regarding the critical state friction angle (φ'_{cs}). Barden et al. (1969) conducted plane strain tests on cubic samples of Welland River sand and found that φ'_{cs} did not vary appreciably with confining stresses ranging from 140-5700 kPa. Similarly, Negussey et al. (1988)

performed ring shear tests on various granular materials and found that φ'_{cs} was independent of normal stress. However, Lings and Dietz (2004) performed direct shear tests on Leighton Buzzard sand found that φ'_{cs} decreased by 3-4^{o} as normal load increased from <50 to 250 kPa. Hamidi et al. (2009) found similar results using direct shear tests, and attribute the decrease in φ'_{cs} to the effects of particle crushing and resulting change in gradation. Therefore, more research exploring the effects of suppression of dilation on φ'_{cs} in direct shear, and the resulting particle breakage is needed. This research must also consider the effects of particle shape (Guo & Su, 2007), particle size/gradation (Dai et al., 2016; Simoni & Houlsby, 2006), and sample size (Bareither et al., 2008), which all have been found to influence shear strength and stress-dilatancy behaviour of sands.

The direct shear test is a relatively simple method for obtaining shear strength parameters of sand, and is used extensively in practice and research; it is also the primary laboratory test used in this research project. Despite its widespread use, researchers are skeptical of the reliability of the direct shear test for obtaining shear strength parameters. Some drawbacks of the test include having the soil fail on a pre-determined plane, and having a non-uniform stress distribution within the shear box (Dounias & Potts, 1993), which generally results in a different stress state than what is observed in the field. Furthermore, direct shear tests performed on sand samples commonly result in an overestimation of peak shear strength (Dounias & Potts, 1993; Lings & Dietz, 2004), which can lead to inadequate geotechnical designs. Regardless of whether the stress state in the direct shear test matches real field conditions, the failure of a granular soil in direct shear is still governed by Coulomb's friction model, as is demonstrated in the results of this thesis. Therefore, results from direct shear tests are still useful for real problems where dilation is suppressed, such as failure at the tip of a pile.

There is clearly a need for more laboratory research on the root causes of the inherent errors in the direct shear test. In addition, the interplay of particle composition, particle breakage and suppression of dilation and their effects on the shear strength of sand need to be better understood.

1.2 Purpose

The purpose of this thesis is to investigate the effects of suppression of dilation on the shear strength of sands through series of direct shear tests conducted under high normal stresses. The following hypotheses will be tested through the research project:

1. Suppression of dilation during shear does not only affect the magnitude of peak shear strength, but can also affect the magnitude of critical state (large strain) shear strength of granular materials.
2. Suppression of dilation is more critical for rounded sands than it is for angular sands.
3. Size of the shear box (vis-à-vis particle size of the sand) is more critical for tests in which the normal loading suppresses the sand's tendency to dilate.

1.3 Outline

This thesis contains five (5) chapters. Chapter 1 provides the motivation and purpose for this research. Chapter 2 provides further background on the theory and mechanisms at play for direct shear testing of sand. This chapter also discusses the current state of knowledge of the factors that affect the shear strength of sands, including suppression of dilation, particle crushing, sample size, particle shape, and particle size/gradation. Chapter 3 provides details on the methodology used for experimentation, including a description of the equipment, testing method and procedure, and sample preparation method. Chapter 4 includes the results from the testing program and discussion of the results. Chapter 5 provides conclusions and recommendations that arise from this research.

Chapter 2 – Literature Review

2.1 Introduction

The following is a literature review of the major topics pertinent to this thesis. Topics covered in this chapter include:

- The use of the direct shear apparatus (DSA) for determining the shear strength and dilatancy of sands.
- The various aspects of soil behaviour and composition that affect its shear strength.
- A summary of previous studies where normal loading suppresses dilation.
- The effects of particle breakage on sand behaviour, including shear strength.

2.2 Direct Shear Testing

The direct shear test is a simple laboratory method for determining the shear strength of soils. The modern apparatus comprises a shear box, displacement cart, and loading frame, which applies a vertical load on the specimen. The shear box consists of two halves, which can move relative to each other. Typically, the lower half of the box is fixed to a rolling cart, which applies a controlled horizontal strain on the sample, while the load frame applies a normal load onto a rigid top cap. A schematic showing a typical direct shear box set-up is shown in Figure 2.1.

Coulomb conducted the earliest known shear testing of soil in 1776 (Lambe & Whitman, 1969). In 1846, French engineer Alexandre Collin also determined shear strength soils using an apparatus similar to that of the modern DSA (Coduto, 2001). The version that is typically used today was first developed by Bell in 1915, who was also the first researcher to publish shear tests on a variety of soil types (Skempton, 1958). Bell's apparatus worked on the 'load-controlled' principle, where known shear loads were applied

incrementally until the sample reached failure. Gilboy at MIT introduced the 'strain-controlled' direct shear test in 1936, which is now the most commonly used method since it allows the measurement of post-peak behaviour (Lings & Dietz, 2004).

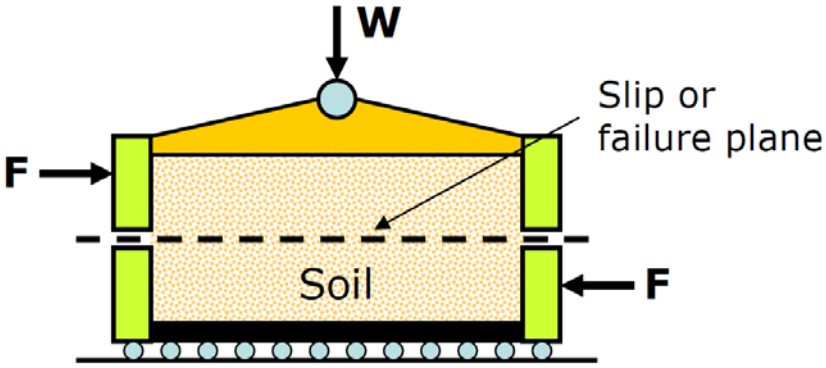

Figure 2.1 – Schematic of a typical direct shear box and resultant forces applied during a test (from Sharma, 2010).

Direct shear tests are advantageous because they are simple and inexpensive to conduct, and can provide a reasonable estimate of shear strength when conducting drained tests on sand (Coduto, 2001). However, there are several inherent problems with the test. Firstly, the shear box forces the soil specimen to shear on a pre-determined horizontal plane, which does not necessarily represent the weakest plane of shearing. Second, the stresses within the shear box are non-uniform, which make it difficult to know the exact state of stresses within the shear zone (Zhang & Thornton, 2007). According to Dyer (1985), the shear load is applied to the soil through the end walls of the shear box. In addition, there is little to no shear stress applied to the soil from the upper and lower boundaries (Jewell, 1989). This results in the upper shear box and soil contained within to generate a force couple, which causes the sample to rotate in order to restore moment equilibrium. A depiction of how the shear forces are mobilized in a conventional direct shear test is shown below in Figure 2.2. The non-uniformity is due to non-coincidence of the principle axes during rotation of principal stresses in the initial stages of shearing, as well as side friction along the walls of the shear box; both of which cause an increase in mobilized shear strength along the central plane (Jewell, 1989). This non-uniformity also cause variations in density throughout the

sample, which further exacerbate the non-uniformities in shear and normal stresses and make it more difficult to interpret volume change (Shibuya et al., 1997).

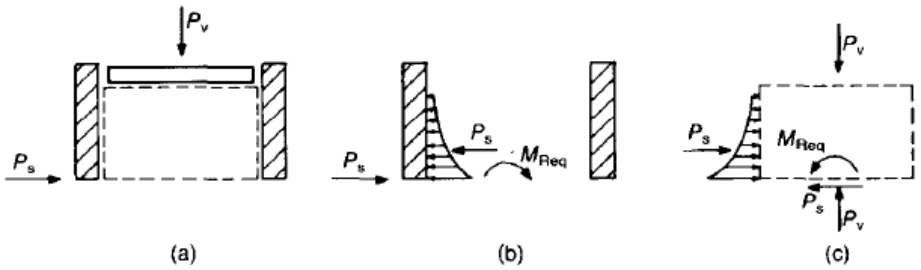

Figure 2.2 – Illustration of shear forces and mobilization of moment couple in a conventional direct shear test (from Jewell, 1989). (a) Configuration of upper shear box prior to shearing with free-to-move top cap, (b) counter clockwise rotation of the upper shear box, and (c) clockwise rotation of the sand within the upper shear box.

Many researchers agree that the conventional direct shear test provides an overestimate of the peak friction angle (φ_p'), and underestimate of the peak dilation angle (α_p) (Lings & Dietz, 2004). Section 2.3.1 provides more details on how φ_p' and α_p are obtained. Jewell (1989) argues that this error is in large part due to the observed non-uniformities. Several studies have attempted to modify the conventional DSA in order to reduce the non-uniformities, most using simple shear tests as the benchmark when comparing shear strength values. For example, Jewell (1989) found that having the rigid top cap fixed to the upper shear box after the normal load had been applied created more symmetry, reduced non-uniformities and eliminated the tendency for rotation. This 'symmetrical' set-up resulted in a reduction in φ_p' and increase in α_p that more closely matched simple shear behaviour and helped counter the overestimation. Shibuya et al. (1997) further improved the 'symmetrical' set-up by fixing the entire upper frame (including the top cap) from moving vertically or rotating, which was found to reduce the occurrence of progressive failure. Lings and Dietz (2004) developed a 'winged' DSA, which applied the shear force along the same plane as the plane of shearing and utilized the 'symmetrical' set-up from Jewell (1989). A schematic of the winged DSA apparatus is shown below in Figure 2.3. The winged apparatus showed a reduction of rotation in the upper frame compared to the conventional DSA; however, rotation was not completely mitigated as suggested by Jewell (1989). Furthermore, the reduced rotation was not

shown to significantly influence the resulting shear strength (Lings & Dietz, 2004). Potts et al. (1987) conducted finite element analysis of the direct shear test and came to similar conclusions that the freedom of the top cap to rotate had little influence on behaviour. The findings of both Lings and Dietz (2004) and Potts et al. (1987) are in disagreement with those of Jewell (1989). Therefore, more research is needed to better understand the mechanisms contributing to inherent errors observed in the direct shear test.

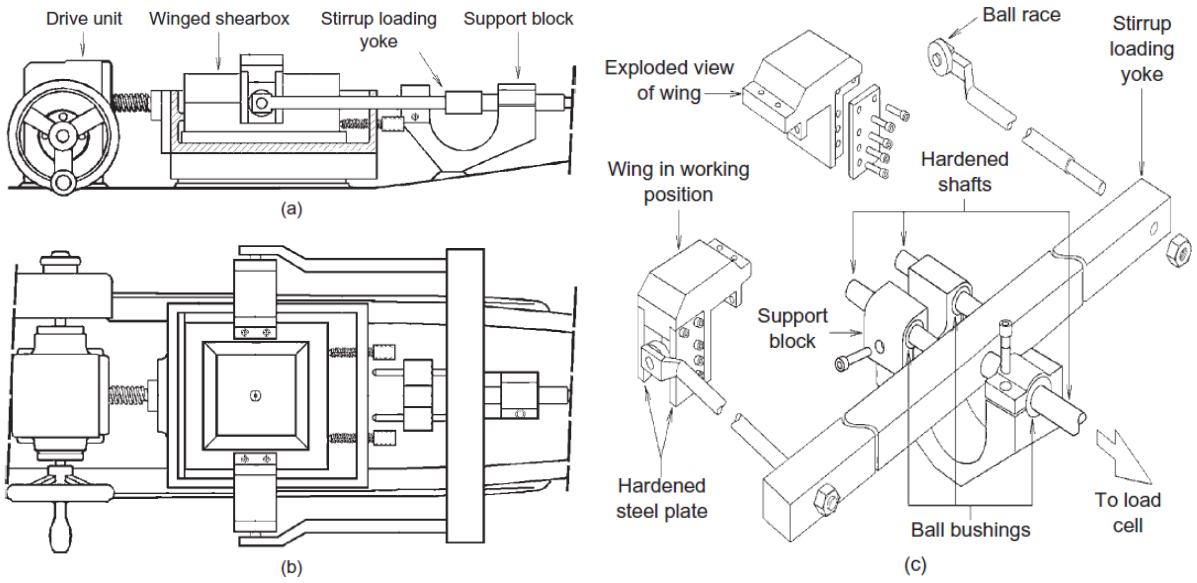

Figure 2.3 – Schematic of 'winged' direct shear apparatus developed by Lings and Dietz (2004): (a) section; (b) plan; (c) perspective.

2.3 Shear Strength and Dilation

Understanding the relation between shear strength and dilation is essential to the correct interpretation of data obtained from direct shear tests. Dilation or contraction of a granular sample occurs because of inter-particle sliding within the zone of shearing. Samples that are densely packed have increased interlocking of particles along the shear plane, and are forced to 'climb over' adjacent particles, thereby causing dilation or expansion of the sample. Conversely, loosely-packed samples tend to contract during shear since consolidation of particles occurs within the shearing zone (Reynolds, 1885). The soil is said to be at 'critical state' when dilation or contraction of the sample is completed (i.e. at constant

volume) (Casagrande, 1936). The shear strength measured during this point of the test is called the critical state shear strength (τ_{cs}). Generally, tests such as direct shear or triaxial compression are completed using a range of normal effective stress values so that the critical state angle of friction (φ'_{cs}) of the soil can be determined.

There are two well-known constitutive models, which characterize the relationship between dilation and shear strength of soils: Coulomb's Friction Model, and Taylor's Model (Taylor, 1948). The following sections will discuss them both.

2.3.1 Coulomb's Friction Model

Coulomb's friction model defines shear strength of the soil at critical state as the inverse tan of the coefficient of friction along a pre-defined failure plane (Budhu, 2011). In terms of stresses, Coulomb's friction model for soils can be written as:

$$\tau_{cs} = (\sigma'_n)_f \tan \varphi'_{cs} \quad [2.1]$$

where τ_{cs} and $(\sigma'_n)_f$ are the shear stress at critical state and normal effective stress at failure, respectively. Depending on whether the soil is in a loose or dense state, it will either contract or dilate during shear before reaching critical state. The response of a typical soil during direct shear is shown graphically in Figure 2.4 (Budhu, 2011). In dense or 'Type B' soils, additional shear strength is mobilized due to interlocking of particles, and a peak shear strength (τ_p) or φ'_p is reached first before reducing to the critical state. Normal strains compress slightly, and then undergo dilation until critical state is reached. For loose or 'Type A' soils, there is a gradual increase in shear strength and normal strain until critical state is reached. φ'_p is a function of the soil type and the degree of compaction, while the critical state angle of friction is considered a fundamental property of the soil (Budhu, 2011).

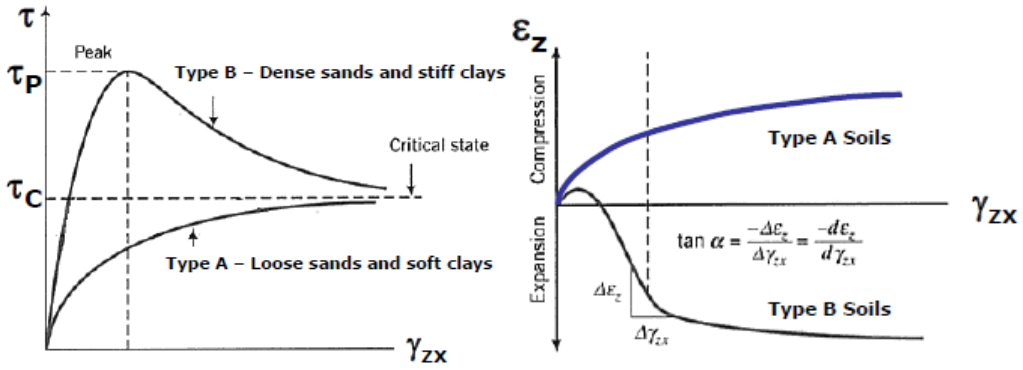

Figure 2.4 – Response of Type A and Type B soils during direct shear (from Budhu, 2011).

In either case, the mobilized shear strength (τ_m) or mobilized angle of friction (φ'_m) may be smaller or larger than that found at the critical state, depending on the angle of dilation (α). In a direct shear test, α is a measure of the change in vertical strain with respect to the change in shear strain (Budhu, 2011), and can be defined as:

$$\alpha = \tan^{-1}\left(\frac{-\Delta\varepsilon_z}{\Delta\gamma_{zx}}\right) \qquad [2.2]$$

This relationship is also shown in Figure 2.4. Therefore, [2.1] can be re-written to account for the effects of dilation angle on shear strength as follows (Budhu, 2011):

$$\tau_m = \sigma'_n tan(\varphi'_{cs} + \alpha) \qquad [2.3]$$

α is positive when the soil is dilating, and negative when contracting. Figure 2.5 shows the relationship between shear stress and normal stress when considering φ'_{cs}, or $(\varphi'_{cs} + \alpha)$. Line OA represents φ'_{cs} determined using [2.1]. In a dense soil where $\alpha > 0$, the soil can mobilize higher shear strength at low normal stresses, represented by the curved failure envelope determined using [2.3]; however, Figure 2.5 shows the effects of dilation reduce (i.e. α becomes smaller) as normal stress increases. Hence, dilation becomes suppressed as normal stress increases. The Coulomb friction model is best used for overconsolidated soils or soils where a pre-failure plane exists (Budhu, 2011), such as the forced failure plane that occurs in the direct shear test.

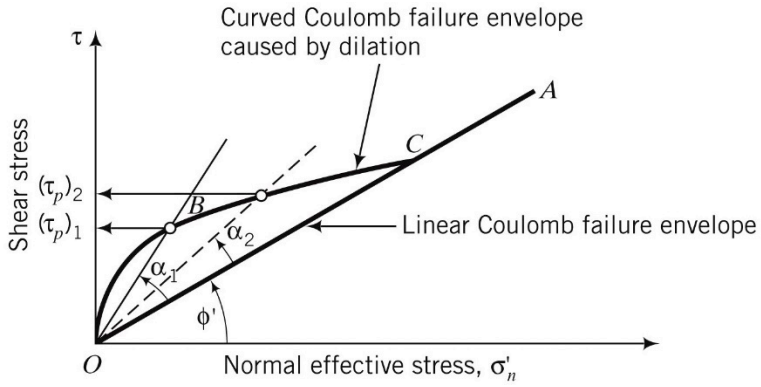

Figure 2.5 – Stress relationship of Coulomb's friction model with and without considering effects of dilation (from Budhu, 2011).

2.3.2 Taylor's Model

Taylor (1948) also assumes that soil mobilizes shear strength due to sliding friction and particle interlocking. However, it differs from the 'sliding block' approach used by Coulomb in that it is based on the principles of external (force) and internal (friction) work and energy. The following equation can be used to model shear strength of soils at critical state (Budhu, 2011):

$$\left(\frac{\tau}{\sigma'_z}\right)_{cs} = tan\,\varphi'_{cs} \qquad [2.4]$$

where σ'_z is the vertical effective stress at critical state. Note that this is different from σ'_n normal effective stress, which acts normal to the shear plane. Taylor's model does not require a pre-defined failure plane, and can therefore be applied at any loading stage for soil that is homogeneous and undergo 'simple shear' (Budhu, 2011). To clarify, Figure 2.6 shows the difference between direct shear and simple shear (Sharma, 2010). Unlike Taylor's model, the Coulomb friction model requires 'direct shear', which has a pre-defined failure plane.

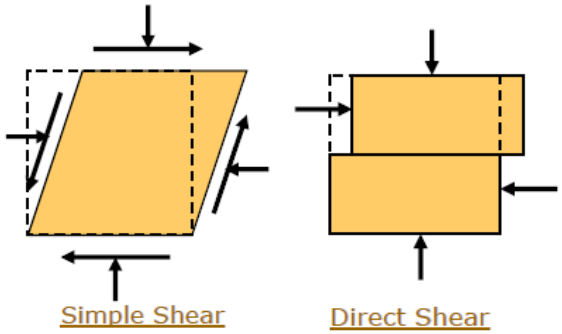

Figure 2.6 – Schematic illustrating the difference between simple shear and direct shear (from Sharma, 2010).

The effects of dilation or contraction on the mobilized shear strength can also be considered using α as expressed in the following equation (Budhu, 2011):

$$\left(\frac{\tau_m}{\sigma_z'}\right)_m = tan\ \varphi_{cs}' + tan\ \alpha \qquad [2.5]$$

Taylor's model is ideal for modeling short-term and long-term strength of homogenous soils (Budhu, 2011).

2.3.3 Four-Stage Shearing Model

Li and Aydin (2010) studied the behaviour of rounded granular materials through direct shear testing, with attention on the fluctuations in stress ratio and vertical displacement that are commonly observed during shearing. They asserted that these fluctuations were due to the net effect of the movement of particles into voids (local contraction) and particle interlocking (leading to local dilation as the particles climb over each other). Figure 2.7 shows the material response during shear, and the division of the shearing process into four (4) distinct stages, as defined by Li and Aydin (2010). Stage 1 (end zone deformation) is predominated by particles, particularly at the boundaries of the shear zone, moving into nearby voids, causing local contraction to dominate. This is reflected in the data by an initial dip in vertical displacement. In Stage 2 (particle interlocking), particles in the shear zone have to overcome interlocking as they come in contact with each other, causing local dilation to dominate. Dilation continues into Stage 3 (shear zone formation), while the relative movement of particles in the shear zone increases, resulting

in a relatively looser layer. In this stage, smaller particles tend to migrate into voids while larger particles roll aside, resulting in a changing structure of the shear zone to reduce internal resistance. Finally, Stage 4 (steady shear) begins at point B, where local dilation and contraction within the shear zone are roughly in equilibrium, and shear strength remains constant. This is often interpreted as the 'critical state' of the soil.

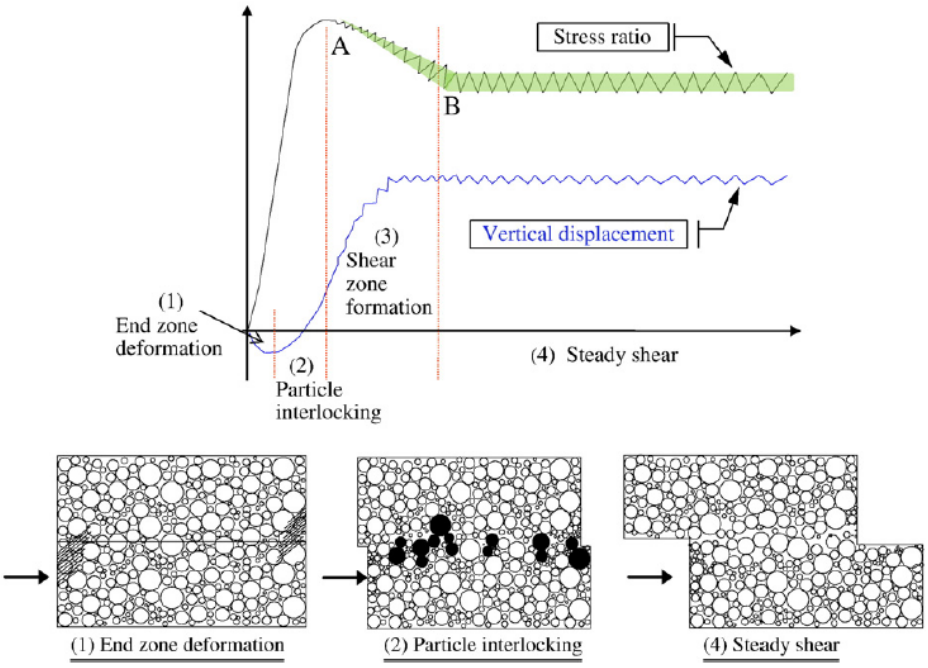

Figure 2.7 – Four-stage model for shearing of granular material in direct shear (from Li & Aydin, 2010).

It was also observed that increasing normal stresses caused both the wavelength and amplitude of these fluctuations to increase, and that the breadth of these fluctuations are related to the breadth of the shear zone. It was concluded that the observed fluctuations could be an indicator of inherent soil properties, and that current methods of averaging this data can lead to loss of valuable information. It should be noted that the normal force was limited to < 400 kPa in the abovementioned study, and that essentially no particle breakage was observed. The effects of particle crushing will be addressed in Section 2.5 of this thesis.

2.4 Suppression of Dilation

Suppression of dilation occurs when soils undergo shear and are unable to expand due to confinement. This can be accomplished during a direct shear test by applying a relatively high normal load on the sample prior to shearing. Figure 2.5 in Section 2.3.1 of this thesis (Budhu, 2011) provides a good visual representation of suppression of dilation using Coulomb's theory. For a dense sand sample, the angle of dilation (α) will increase with relative density and will provide additional 'peak' strength to the sand. As normal stress is increased, α eventually reduces to zero, and the dense soil then behaves like a loose one. Another method would be to restrict vertical/upward movement of the top cap, so that the soil can shear at a constant volume. Shibuya et al. (1997) and Qui et al. (2000) have developed direct shear equipment that enable shear at a constant volume; however, true constant volume proved difficult to achieve due to limited rigidity in the loading frames.

It should be noted that suppression of dilation may be partial or total. Partial suppression of dilation simply means the normal stress is large enough to cause a reduction in α, but $\alpha > 0$. Total suppression of dilation would result in $\alpha = 0$. Also note that while vertical displacement of the sample may change from positive (dilation) to negative (contraction), α cannot be less than zero.

According to McDowell and Bolton (1998), particle breakage is the predominant mechanism that allows for suppression of dilation to occur during shear. If the soil sample is unable to expand via soil particles rolling and 'climbing over' each other, then the soil particles break into smaller particles, fill the adjacent voids, and the sample contracts. Arslan et al. (2009) demonstrates this by performing direct shear tests on manufactured granular materials (MGM), having different particle crushing strengths. Figure 2.8 shows how vertical displacement of the sample varies with shear strain for each material. Material FA has the lowest particle crushing strength and is therefore most susceptible to breakage, followed by FC10, FC20, with FC30 having the highest strength. From Figure 2.8, it is evident that the dilatancy of material FA is suppressed, while the other materials with stronger grains were free to dilate. For this reason, it is

important to consider the effects of particle breakage in this thesis, which is explored in more detail in the following section.

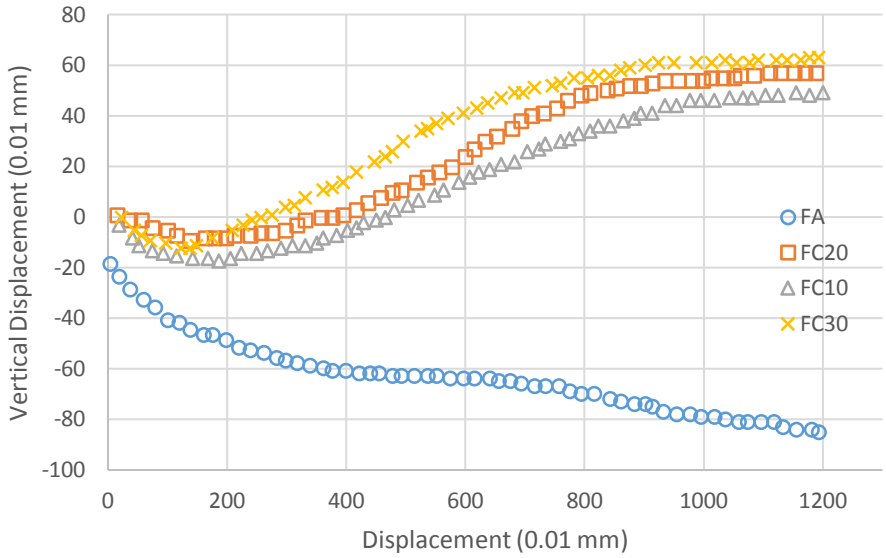

Figure 2.8 – Comparison of dilatant behaviour of MGM under 100 kPa normal pressure (modified from Arslan et al. 2009).

2.5 Particle Breakage

Particle breakage or particle crushing can occur when soils are sheared under high confining pressures or are simply confined under a static load, whereby localized stresses on a given particle exceed its tensile strength. Particle breakage can change the structure and gradation of the soil and has the potential to significantly change the engineering properties of the soil, depending on the extent of breakage (Hardin, 1985). Examples of where particle breakage can occur in the field include beneath large structures such as earth dams, or at the tip of deep end-bearing piles. The following subsections will discuss the current state of the literature on particle breakage, its driving mechanisms, how it can be quantified, and how it can affect the behaviour of sand during shear.

2.5.1 Mechanisms (Fractals, Force Chains and Creep)

There are two predominant mechanisms for particle breakage under static load: 1) Attrition, which involves the breakage of small asperities on the outer surface of a particle upon loading, creating

mostly dust, and 2) Rupture, which is the tensile splitting of a larger particle in to smaller pieces, producing a minimal amount of dust (Ezaoui et al., 2011). It is generally accepted that dominant mode of failure of a spherical particle under compression is tensile failure via rupture (McDowell & Bolton, 1998). Lee (1992) conducted crushing tests on individual grains of Leighton Buzzard sand, oolitic limestone and carboniferous limestone and determined the tensile stress at failure by compression between two flat platens, a method developed by Jaeger (1969). Lee (1992) noticed that as displacement of the platens increased, there were initial failure points caused by attrition on the particle surface, but that the main catastrophic failure (rupture) occurs later, accompanied by tensile splitting of the particle. It was found that the tensile strength was not constant for a given particle size, but had some statistical variation about a mean value (Lee, 1992). This is due to the presence of internal flaws, which will vary from particle to particle (Lade et al., 1996). In addition, it was found that as the mean particle size (d_{50}) increased, the value of mean tensile strength decreased, which is consistent with many previous and subsequent experiments (Lee, 1992). In other words, larger particles are weaker than smaller particles, because larger particles also tend to have larger flaws.

These observations from Lee (1992) led to the application of Weibull (1951) statistics of fracture to describe the tensile strength of soil particles by McDowell, Bolton and Robertson (1996). Weibull (1951) statistics is based on the principal that a block of material is as strong as its weakest link; in other words, a grain of sand will remain intact under tension until one of its weakest internal elements begins to fracture. Weibull's 'survival probability' formula for a block of material under tension is given by:

$$P_s(V) = exp\left[-\frac{V}{V_0}(\frac{\sigma}{\sigma_0})^m\right] \quad [2.6]$$

where V is the volume of the block, σ is the applied tensile stress, $P_s(V)$ is the survival probability, and σ_0 is the value of tensile stress where 37% of the total number of tested blocks survive. V_0 is a reference volume where:

$$P_s(V_0) = exp\left[-(\frac{\sigma}{\sigma_0})^m\right] \quad [2.7]$$

The above relationship is depicted graphically in Figure 2.9. The exponent m is termed the Weibull modulus, and ranges between about 5 for soils with highly variable tensile strength (such as calcareous sands) and 10 for such materials as engineered ceramics, which has much less variable tensile strength (McDowell & Bolton, 1998). As the value of m increases, the slope of the probability function becomes much steeper, and therefore varies in probability over a much narrower range of tensile stresses. Using the data from Lee (1992), McDowell and Bolton (1998) were able to prove that Weibull (1951) statistics provides an accurate framework for measurement of tensile strength of soil particles.

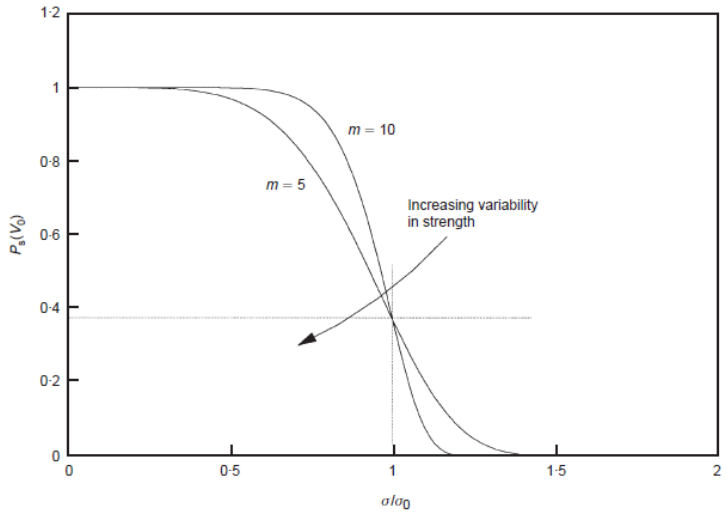

Figure 2.9 – Weibull (1951) distribution (from McDowell & Bolton, 1998).

However, a more thorough mathematical framework was needed to accurately describe the changing of particle sizes of a soil during particle breakage. Turcotte (1986) observed that a variety of crushed materials had size distributions that could be described using fractal theory. A fractal is a mathematical concept developed by Mandelbrot (1982) that describes and quantifies a repeating pattern which is independent of scale, that is often observed in nature (e.g. trees, leaves, landforms etc.). The fractal theory says that the number of particle fragments which has size L greater than size d follows a power law relationship given by:

$$N(L > d) = Ad^{-D} \quad [2.7]$$

where A is the constant of proportionality, and D is the fractal dimension. Tyler and Wheatcraft (1992) developed another relationship that enables one to use results from routine grain size analysis to determine its fractal behaviour:

$$\frac{M(L < d)}{M_T} = \left(\frac{d}{d_L}\right)^{3-D} \quad [2.8]$$

where $M(L < d)$ is the cumulative mass of particles with size *L* finer than size d, M_T is the total mass of particles, *d* is the particle size (i.e. sieve size opening) and d_L is the maximum particle size (i.e. largest sieve size). The fractal dimension for most materials under pure normal compression is approximately 2.5. This has been determined experimentally by Turcotte (1986), and confirmed through mathematical modeling by Steacy and Sammis (1991) and Palmer and Sanderson (1991). While [2.7] can model fractals over an infinite range of particle sizes, it is important to note that this range must have a limit in order to model real behaviour. The upper limit would be the original size of the particle, while the lower limit would be some size d_s, which gets smaller as normal stress increases and the larger particle successively splits (McDowell & Bolton, 1998).

Vallejo et al. (2005) carried out 1D-compression tests on 5.0 mm glass beads at various loading increments and compared normal loading with fractal dimension (*D*) determined using [2.8]. Results indicated that the distribution of the force chains, as well as the intensity pattern of the force chains are fractal in nature. Therefore, it seems that the fractal theory can provide a common framework for many aspects of crushing in granular materials, from describing the crushing of individual particles to characterizing the loading mechanisms of force chains. Vallejo et al. (2005) also found that the value of *D* increased with increasing applied compressive stress and therefore, particle breakage; meaning *D* could be used as a means of quantifying the extent of particle breakage. Further discussion on methods of quantifying particle breakage can be found in section 2.5.2.

According to McDowell et al. (1996), the probability of fracture of a soil particle increases as normal stress increases, but reduces as the number of inter-particle contacts (coordination number) increases. This is because a higher coordination number means more adjacent particles are able to share the loading, thereby reducing the local contact stresses per particle (Jaeger, 1969). Therefore, despite smaller particles having higher individual tensile strength than larger particles, McDowell et al. (1996) argues that smaller particles must have the highest probability of fracture since they have the fewest contacts (i.e. lowest coordination number). Alternatively, large particles in a non-uniform soil mixture tend to be surrounded by many smaller particles, giving a high coordination number. This assumption was found to model the typical behaviour of crushing granular material quite well (McDowell et al., 1996).

The term 'force chain' is used to describe the mechanism by which individual soil particles transfer a globally applied load to its adjacent particle or particles along a chain-like network (see Figure 2.10) (Vallejo et al., 2005). Some force chains may carry a large portion of the applied load, others may carry much less, and some particles in between may carry no load at all. Coordination number and particle size will have an effect on how the force chains arrange themselves. Particle breakage begins when the particles in the highest loaded force chains begin to fracture, which then split into smaller pieces and migrate in to nearby voids. This rearrangement of particles causes an overall settlement of the soil sample and changes its grain size distribution (GSD). As crushing continues, the permeability of the granular material decreases and it becomes more resistant to crushing (Vallejo et al., 2005). This gradual stabilization and settlement of granular materials through particle breakage under an applied normal load is also known as 'creep'.

Jardine et al. (1999) describe the process of creep in granular materials in terms of force chains and particle rearrangement. Force chains that are weakly loaded tend to collapse/rearrange during 1D compression, which effectively removes the lateral support from the adjacent highly loaded force chains, thereby causing yielding or buckling. Over time, this process gradually slows down as the network of highly

loaded force chains strengthen and coordination number in the sample gradually increases. Therefore, creep in granular materials is directly related to particle breakage (Karimpour & Lade, 2010).

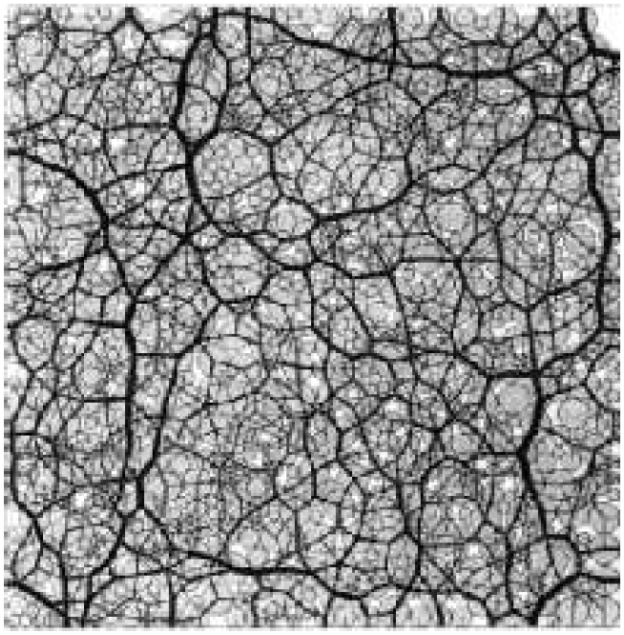

Figure 2.10 – Force chains having varying intensity in 2D DEM model for discs under a static load (from Vallejo et al. 2005).

2.5.2 Quantifying Particle Crushing

Many different particle breakage factors have been developed over the years. The earliest was by Marsal (1967), who developed a breakage index, *B*, which is based on the change in individual particle sizes before and after crushing. The value of *B* is determined by comparing the percent retained on each sieve, and determining the sum of the differences having the same sign. Lee and Farhoomand (1967) proposed a different breakage factor based on the ratio of 15% finer (d_{15}) before and after crushing (d_{15} (initial)/d_{15} (final)). Hardin (1985) introduced three new breakage parameters, which are based on a comparison of the entire grain size curve. These parameters are called the breakage potential (B_p), total breakage (B_t), and relative breakage (B_r), which are shown graphically in Figure 2.11 below. Breakage potential is a theoretical value based on the resulting change in grain size curve if every particle was crushed to a size smaller than 0.075 mm. Total breakage corresponds to the area formed between the

before and after grain size curves. Relative breakage is defined as the total breakage divided by the breakage potential (B_t/B_p). Hardin (1985) affirms that using these breakage parameters can greatly simplify analysis when trying to isolate the effects of breakage from effects of effective stresses, effective stress path, initial void ratio, particle shape and particle hardness. This is also one of the more widely used parameters in the literature today due to its stability and robustness (i.e. all sieve sizes are used in its determination).

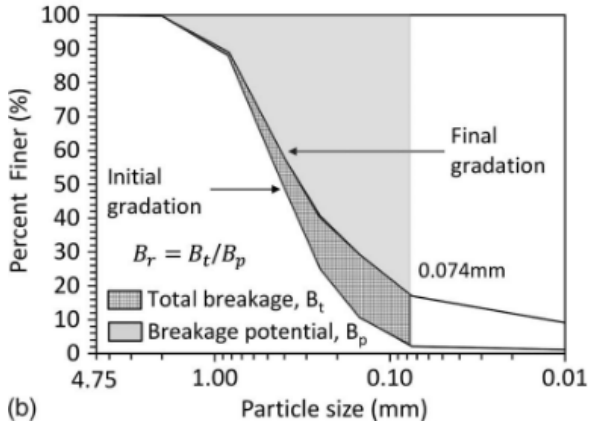

Figure 2.11 – Example GSD curves illustrating Hardin's relative breakage parameters (from Mun & McCartney, 2017).

Lade et al. (1996) have developed their own particle breakage factor, with a focus on being able to correlate particle crushing with soil permeability, based on D_{10}:

$$B_{10} = 1 - \frac{D_{10f}}{D_{10i}} \quad [2.9]$$

where B_{10} = particle breakage factor, D_{10f} = effective grain size after crushing (final), and D_{10i} = effective grain size before crushing (initial). The author's analysis determined that this breakage factor is stable and effects of scatter are reduced in comparison to those previously mentioned.

At the microscale, one could quantify particle breakage by determining the crushing strength of individual particles. This has been done by many researchers previously including Jaeger (1969), Lee (1992) and more recently by Arslan et al. (2009). Arslan et al. (2009) conducted experiments using MGM

which allows for more flexibility in controlling the crushing strength. Crushing (tensile) strength was determined using the single aggregate crushing test outlined by ISO/DIS 11273-1:

$$\sigma_t = \frac{F_c}{A_m} = \frac{F_c}{\left(\frac{\pi}{4} d_m^2\right)} \quad [2.10]$$

where:

$$d_m = \frac{d_1 + d_2 + d_3}{3} \quad [2.11]$$

and σ_t = particle tensile strength, F_c = force at which crushing occurs, A_m = mean area of particle, d_1, d_2 and d_3 are the maximum, intermediate and minimum principal dimensions of the particle, respectively, and d_m= mean particle diameter. This approach is based on the point load tests conducted by Jaeger (1969).

More recently, Konrad and Salami (2017) provided a framework for modeling particle breakage in soils or other crushable granular material. The model can predict the progression of particle crushing based on mechanical conditions, initial grain size distribution (GSD), and individual particle crushing strength. The method relies on the breakage parameter '*ν*', which is defined as the slope of the GSD when plotted on log-log scale (see Figure 2.12). The value of *ν* decreases as the extent of crushing increases due to increasing confining pressure.

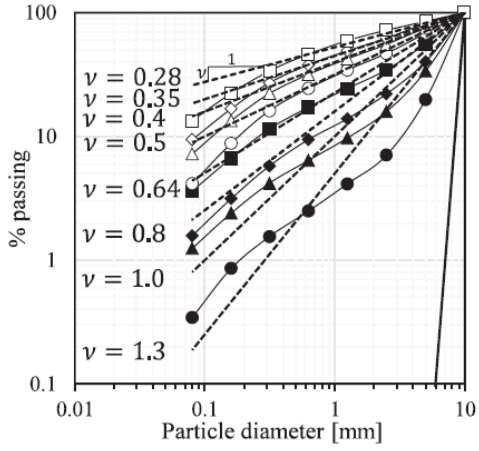

Figure 2.12 – Definition of new breakage parameter (from Konrad & Salami, 2017).

Figure 2.13 below shows the model concept developed by Konrad and Salami (2017) graphically, plotted in terms of breakage parameter, *v*, and input work per unit volume. The model is based on the principle that crushing occurs in three distinct stages: AB, where there is a negligible amount of grain breakage; BC, where significant grain breakage occurs; and CD, where grain breakage stabilizes and an ultimate GSD is reached, denoted by parameter v_u.

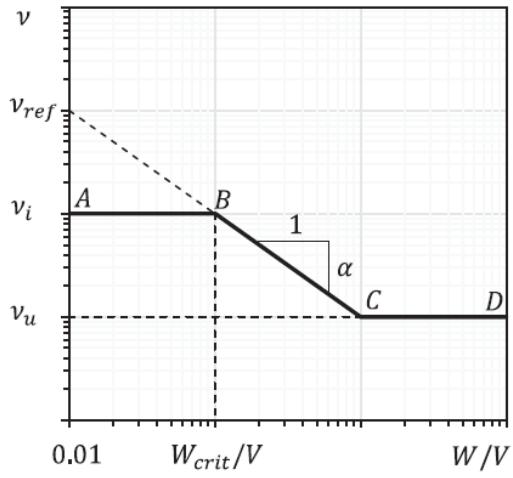

Figure 2.13 – Conceptual breakage model for an assemblage of particles (from Konrad and Salami, 2017).

Four parameters are required to properly model the changes in *v*: v_i = slope of the initial GSD in log-log scale; v_{ref} = reference value of *v* at a reference value of W_{ref}/V = 0.01MPa; α = slope of segment BC; and v_u = ultimate GSD. In addition, W_{crit} = input work required for crushing to begin and V = volume of the element under consideration. The following system of equations describes the conceptual model proposed by Konrad and Salami (2017):

$$\begin{cases} v = v_i & \text{for } W < W_{crit} \\ \log\left(\frac{v}{v_i}\right) = -\alpha \log\left(\frac{W}{W_{crit}}\right) & \text{for } W \geq W_{crit} \end{cases} \quad [2.12]$$

where $W_{crit} = 0.01*(v_{ref}/v_i)^{1/\alpha}$ (in MPa). Individual particle strength plays an important role in predicting v_u. The following formula derived from the work of Turcotte (1997) is based on fractal theory, and can be used to determine v_u from the average particle strength, $\overline{\sigma_t}$:

$$v_u = 0.190 ln(\overline{\sigma_t}/\overline{\sigma_{ref}}) - 0.14 \quad [2.13]$$

where $\overline{\sigma_t}$ is the tensile strength of the d_{50} sized particle (i.e. average tensile strength), and $\overline{\sigma_{ref}}$ is introduced for the purposes of homogeneity, and is equal to 1 MPa. This model is advantageous because it uses common engineering parameters, and the use of grain strength helps to represent aspects of soil behaviour that are missed using existing breakage models. It appears that the breakage parameter, *v*, can be predicted fairly well; however the value of this is limited (as with other mentioned breakage parameters) in that a single parameter cannot fully describe the GSD (Konrad & Salami, 2017).

2.5.3 Factors That Affect Extent of Breakage

Generally, larger amounts of particle breakage occur at higher stress levels, and when large strains occur within these high stresses (Lade et al., 1996). According to Hardin (1985), the amount of particle breakage that occurs in an element of soil under stress depends on several factors: 1) particle size and GSD; 2) particle shape; 3) state of effective stress; 4) effective stress path; 5) void ratio; 6) particle hardness; 7) presence or absence of water. The following sections describe each of the above factors in more detail.

2.5.3.1 Particle Size and Grain Size Distribution (GSD)

The GSD of a soil will inevitably change after undergoing breakage. However, the reverse effect is also true: a soil's initial GSD will affect the total amount of breakage that takes place. Lee and Farhoomand (1967) determined that uniform soils compress and crush more than well-graded soils with the same maximum particle size. This is because well-graded soils have a greater amount of inter-particle contacts, which thereby reduces the magnitude of localized contact stresses, resulting in less particle breakage. Maximum particle size or average particle size is also known to affect extent of breakage. It is understood that sands with a larger average particle size have a higher potential for breakage (Lade et al., 1996) because larger particles generally have larger defects within them, making them structurally weaker than smaller particles. One recent study by Wang et al. (2015) examines the effects of particle size and compaction on Hardin's relative breakage parameter for a crushed sandstone-mudstone mixture. The

authors observed that as the median particle size increased, the average relative breakage also increased, which confirms the earlier observations from Lee and Farhoomand (1967). However, as was mentioned in Section 2.5.2, coordination number tends to dictate which particles in a given soil mixture will fracture first. Since smaller particles have a lower coordination number, these particles tend to break first, while the largest particles with high coordination numbers will break last (McDowell et al., 1996).

2.5.3.2 Particle Shape

Research has shown that angular particles tend to break more easily than rounded particles. This is because stresses become concentrated along their most narrow dimension as well as their angular contact points, resulting in fracture (Lade et al., 1996). This was determined experimentally by Lee and Farhoomand (1967), and was in agreement with results of previous 1D compression tests on sand. Figure 2.14 illustrates this by comparing grain size curves of angular and sub-rounded coarse sand having the same mineralogy, before and after crushing, and at the same loading conditions. However, at very large stress levels, angular and rounded particles behave more or less the same, i.e. they tend to result in similar breakage and compression (Lee & Farhoomand, 1967).

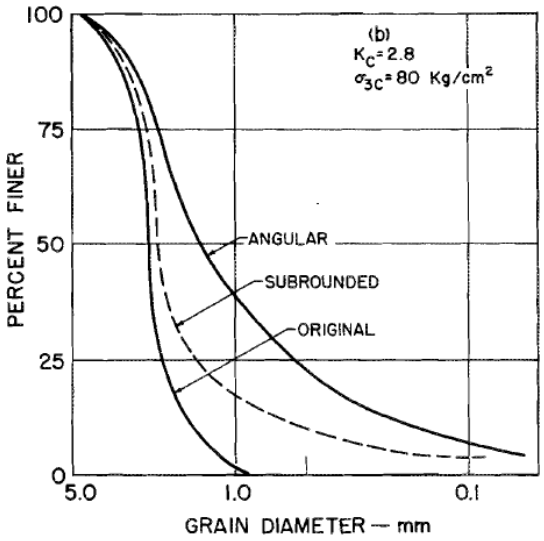

Figure 2.14 – Comparison of crushing of angular and sub-rounded coarse sand (from Lee & Farhoomand, 1967).

2.5.3.3 Effective Stresses

In 1996, Lade and Yamamuro co-authored 'sister' studies where they conducted a series of axisymmetric tests on dense Cambria sand under high confining pressures. Samples were confined under drained isotropic compression with pressures that ranged between 6.4 and 68.9 MPa, followed by drained shearing. The results show that as the initial confining pressure (effective stress) increases, particle breakage increases as the grain size curves progressively become more well graded (see Figure 2.15). The largest amount of particle breakage occurred at normal stresses between 5 and 30 MPa. At higher stresses, the amount of particle breakage became constant (Lade & Yamamuro, 1996).

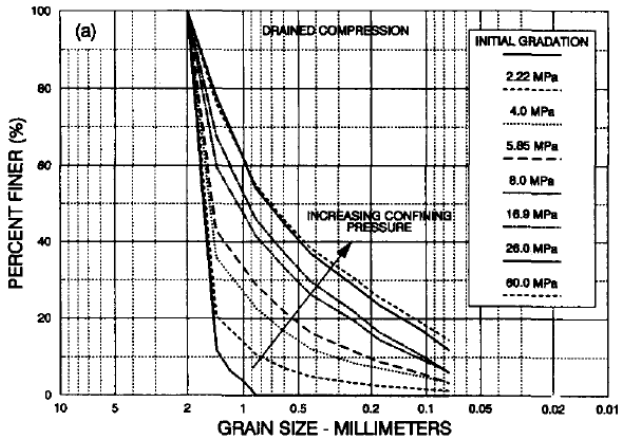

Figure 2.15 – GSD curves for high-pressure drained triaxial compression tests of varying confining pressures on dense Cambria sand (from Lade & Yamamuro 1996).

2.5.3.4 Stress Path

Hardin (1985) demonstrated that effective stress path also has an effect on particle breakage using samples of crushed granite tested by Lee and Farhoomand (1967). Samples were loaded at three different principal stress ratios ($K_o = \sigma'_1/\sigma'_3$), which were kept constant during the tests. It was shown that as the K_o increased, so did the relative breakage. Based on this, Hardin (1985) and Konrad and Salami (2017) ensured that their breakage parameters could quantify breakage independent of stress path.

2.5.3.5 Void Ratio

The void ratio of a sand can change either by consolidation upon normal loading, or during shearing. During consolidation, void ratio reduces due to rearrangement of particles and if the normal loading is large enough, particle crushing can contribute to this reduction in void ratio. Additional energy induced during shearing also contributes to the rearrangement and breakage. Results from Yamamuro and Lade (1996) on Cambria sand demonstrates this, as shown in Figure 2.16. Hardin's relative breakage (B_r) and void ratio at failure for a variety of drained triaxial tests are plotted against effective mean normal stress at failure. It can be seen that the point at which the void ratio at failure begins to sharply decrease coincides with the point at which B_r sharply increases. The author explains that at high stresses, the densification caused by isotropic consolidation dominates and that which is caused by shearing is minimal. This means that the difference in void ratio at failure caused by changing stress paths becomes less pronounced when normal stresses become very high.

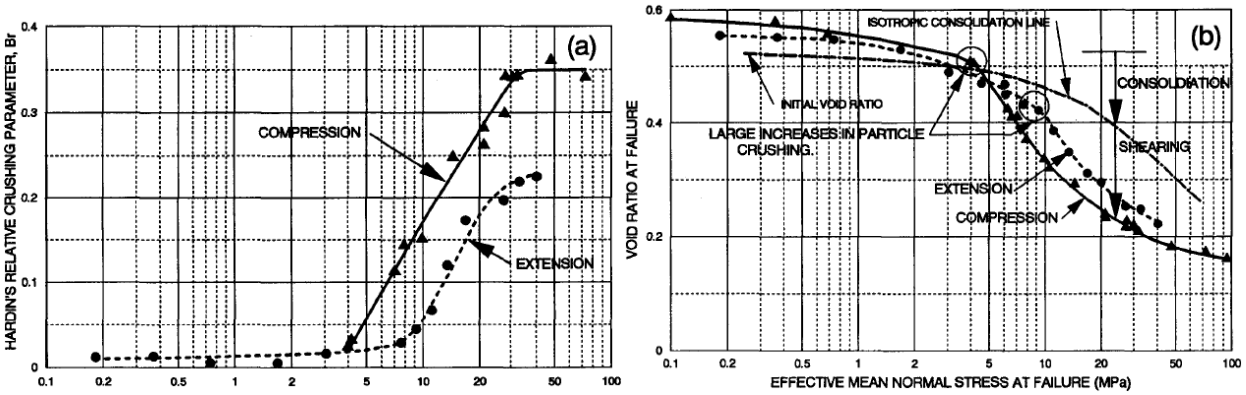

Figure 2.16 – Drained compression and extension tests on dense Cambria sand: (a) Hardin's relative breakage parameter Br, and (b) void ratio at failure (from Yamamuro & Lade, 1996).

Initial void ratio has also been shown to affect particle breakage. One study by Ezaoui et al. (2011) demonstrates this through four (4) triaxial compression tests performed on crushable MGM, having the same stress path and particle hardness, but with two different initial void ratios e_{max} (loose) and e_{min} (dense). One might think that a looser sample should result in less breakage since there are more voids for particles to rearrange themselves and increase the number of inter-particle contacts before

succumbing to fracture; however, this was not the case. Relative breakage was found to be higher for the loose sample than for the dense sample. Since the same stresses were applied to both samples, this result is likely due to the looser sample having less inter-particle contacts and, therefore, higher local stresses per particle than the denser one (Ezaoui et al., 2011).

2.5.3.6 Particle Hardness

Ezaoui et al. (2011) performed a series of triaxial compression, oedometer, and annular shearing tests on MGM, having the same gradation and void ratio to assess the effects of particle hardness on relative breakage. It should be noted that individual MGM grains were strength tested and were found to be much weaker than natural mineral soils. It was found that relative breakage was higher for the material that had a lower individual particle hardness. This is consistent with the stress-strain curves produced, i.e. the material with the lowest particle strength resulted in a stress-strain curve positioned lower than its higher strength counterpart. The author also noted that the deviatoric stress (q) seems to dominate the effects on relative breakage, compared to the mean stress (p'); however the effect of p' seems to be more related to particle hardness, since B_r showed a more dramatic increase with p' in the weaker particles.

2.5.3.7 Addition of Water

Lee and Farhoomand (1967) reference a study by Sowers, Williams and Wallace (1965), which examined the settlement and compressibility of rockfill. Laboratory tests showed that the addition of water increases the rate and extent of compression and particle crushing. Nobari and Duncan (1973) conducted a study, which analyzed the effects of reservoir filling on strength and movements within rockfill dams, and found that particle crushing increased with rising water levels, thereby causing movement of the dam.

2.6 Factors that affect Shear Strength

There are many factors that can affect the engineering properties of sands. According to Mitchell and Soga (2005), these can be divided into two groups: compositional factors and environmental factors. Compositional factors include mineralogy, particle shape, particle size, and GSD. The influence these items have on shear strength can be studied using disturbed, or reconstituted samples prepared in the laboratory. Environmental factors include density, confining pressure, temperature and soil fabric, which require undisturbed samples obtained from field investigations to study properly. This thesis is focused on studying the effects of compositional factors using reconstituted sand samples; however, effects of scale (i.e. sample size) and confining pressure (leading to particle breakage) are also considered in this study despite using reconstituted samples, because they are used as part of routine direct shear testing in practice.

2.6.1 Particle Shape

Particle shape can have a significant effect on the mechanics of soils, and is typically described in terms of 'sphericity' and 'roundness'. Sphericity is the ratio of the diameter of a sphere having equal volume to a particle to the diameter of a sphere that circumscribes that same particle. Roundness is the ratio of the average radius of curvature of the corners and edges of the particle to the radius of the maximum sphere that can be inscribed (contained) in that particle (Mitchel & Soga, 2005). Methods for describing particle shape have been developed by Krumbein and Sloss (1963) and Powers (1953) and charts are provided below in Figure 2.17.

It has been determined through experimentation that φ'_{cs} depends not only on inter-particle surface friction, but also on particle shape. Sands that have angular particles tend to have higher shear strength than those with rounded particles (Guo & Su, 2007). Koerner (1970) found that particle angularity may contribute to the variation of φ'_{cs} up to 8°, since angularity creates an interlocked fabric and provides

additional resistance to particle rotation, thus also increasing dilatancy. Chan and Page (1997) and Sukumaran and Ashmawy (2001) have come to similar conclusions. Ni et al. (2000) reported both peak and critical state shear strength increased with inter-particle friction and with decreasing sphericity. It was also found that materials having a broader range of sphericity (i.e. have a mix of flat-elongated and more spherical particles) tend to be less efficient at packing, thereby affecting their initial void ratio. This can cause a material to behave more like a 'loose' soil compared with a material that has more uniform sphericity that achieves a denser packing (Cho et al., 2006).

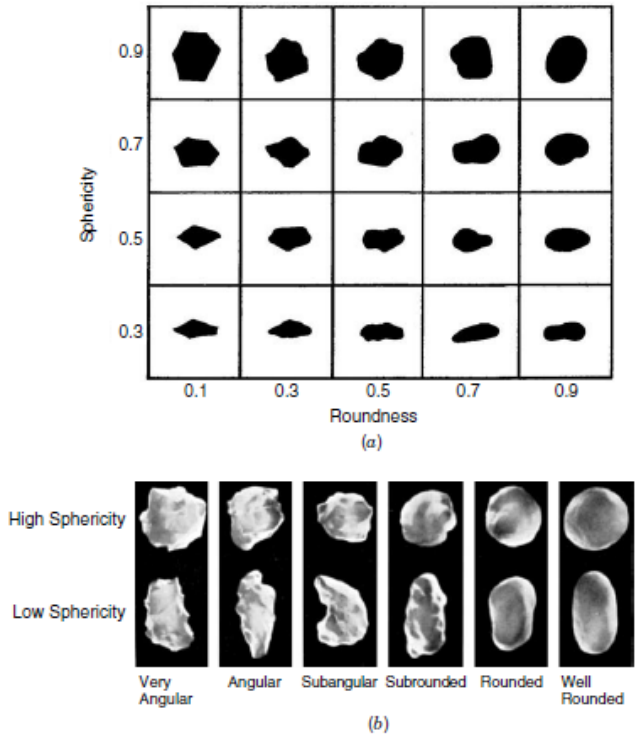

Figure 2.17 – Charts for describing particle shape: a) Roundness and sphericity chart (Krumbein & Sloss, 1963). b) Particle shape characterization (Powers, 1953). (from Mitchel & Soga, 2005).

2.6.2 Particle Size and Gradation

Characterizing soils by particle size and gradation (i.e. grain size distribution) is fundamental for geotechnical engineers. Gradation of a soil is often described using the slope of the GSD curve, or coefficient of uniformity (C_u):

$$C_u = \frac{d_{60}}{d_{10}} \quad [2.14]$$

where d_{60} and d_{10} represent the particle size in which 60 and 10 percent of the particles are smaller than (Mitchel & Soga, 2005). A soil with C_u between 5 and 10 is considered well graded, while values outside of this range indicate a poorly graded soil. Particle sizes are given standard definitions as well through the Universal Soil Classification System (USCS). Coarse sands have particle sizes ranging in diameter from 2-4.75 mm, medium sands from 0.420-2 mm, and fine sands from 0.075-0.420 mm.

According to Simoni and Houlsby (2006), drained triaxial tests were conducted by Leslie (1969) on well-graded alluvial gravels, who found that peak shear strength increased significantly with an increase in C_u (by approximately 2.5°, with C_u changing from 3 to 8); much more significant than the increase in shear strength observed from increasing the maximum particle size (approximately 1°). Kirkpatrick (1965) observed similar effects due to changing the maximum particle size of a fine to medium-grained sand (from 0.3-2 mm), but effects of gradation on peak strength were inconclusive. Dai et al. (2016) conducted 96 direct shear tests on glass beads of different particle sizes and found that both φ'_p and φ'_{cs} increased with increasing mean particle size. However, Marachi et al. (1972) conducted laboratory tests on rockfill materials and showed that shear strength decreased with increasing mean particle size. Therefore, the effects of particle size on shear strength is still an open question (Simoni & Houlsby, 2006).

Regarding gradation, Igwe et al. (2012) found that initial relative density might be a determinant factor on how initial gradation affects shear strength. The authors performed ring shear tests both loose and medium-dense samples having four different gradations: narrowly graded (NAG), intermediately graded (ING), well graded (WG) and gap graded (GAG). They concluded that for loose samples, WG specimens show higher peak and residual shear strengths than poorly graded ones, while for med-dense samples, WG specimens produced the highest peak shear strength, but had the lowest residual strength (Igwe et al., 2012). In conclusion, further research is required to better understand the effects of particle size and gradation on shear strength of sands.

2.6.3 Scale Effects

In direct shear testing, scale effects refer to the ratio of the size of the individual soil particles being tested to the size of the shear box, and the effects this ratio might have on the stress-dilatancy response of the granular soil. According to Harehdasht et al. (2018), this problem arises from the artificial restraints introduced to the sample via the rigid boundaries of the shear box. Previous studies indicate that there are two specific issues worth investigating: the effects of shear box size on macroscopic shear stress ratio, and extent of the shear zone developed inside the box (Harehdasht et al., 2018).

Bareither et al. (2008) conducted a study in which friction angles of thirty (30) sand backfill materials obtained from small-scale (64 mm square) and large-scale (305 mm square) direct shear tests (SSDS and LSDS tests) were compared. Triaxial compression tests were also completed on four (4) of the sand samples. Failure envelopes determined from the SSDS and LSDS tests and triaxial tests were essentially the same (i.e. no significant scale effects were observed), provided that gravel content was less than 30%. In another study, Cerato and Lutenegger (2006) conducted direct shear tests on five different sand types in three square shear boxes of various sizes; each at a dense, medium, and loose state. The authors found that φ'_{cs} decreased or remained constant as the size of the shear box increased. Also, there was little to no specimen size influence on φ'_{cs} when the W/D_{max} ratio (width of shear box divided by the maximum particle diameter) was greater than 50. It was observed that the largest variations in φ'_{cs} occurred where the W/D_{max} ratio was at its lowest. The authors concluded that sand characteristics such as particle size shape and gradation seemed to have the greatest influence on the scale effect (Cerato & Lutenegger, 2006). Ni et al. (2000) conducted 3D numerical modeling of a direct shear test containing up to 50,000 particles to assess scale effects. This data was compared to real direct shear testing on Leighton Buzzard sand having a similar GSD as the model. It was found that φ'_{cs} decreased by about 24% when the number of particles was increased from 5000 to 50000, while φ'_{p} increased more modestly at about 3.7% (Ni et al., 2000). More recently, Harehdasht et al. (2018) conducted 276 'symmetrical' direct shear tests

(after Shibuya et al., 1997; Lings & Dietz, 2004) using round basalt microspheres, and two additional sands (Peribonka and Eastmain) having different angularities, and using 55 mm x 55 mm and 88.5 mm x 88.5 mm shear boxes. They found that there was no significant effect of shear box size on the shear strength and dilation behaviour of the 'symmetrical' shear box. Also, using discrete element method (DEM) analysis, the authors found that within the shear zone of the two different shear boxes, deformation was uniform and progressive failure effects were minor, which is in agreement with findings from Potts et al. (1987).

There is some disagreement in the results between these studies. In addition, it is unclear in Bareither et al. (2008) whether the friction angle under study was at peak or critical state. Therefore, studying scale effects on the shear strength of sands for this research project will be useful.

2.6.4 Particle Breakage

Numerous studies have focused on how particle breakage effects the shear strength of granular materials. Ghafghazi et al. (2014) states that particle breakage causes additional compressibility and volume change, resulting in uncertainty in defining the critical state condition. Barden et al. (1969) conducted plane strain tests on River Welland sand under a wide range of confining pressures. They found that for confining stresses between 140 – 5860 kPa, φ'_{cs} did not vary appreciably with normal pressure. Since inter-particle friction angle (φ_u) is known to decrease with decreasing inter-particle forces (Rowe, 1962), it was believed that the increase in the number of inter-particle contacts caused by breakage counteracted this, resulting in a constant friction angle.

Arslan et al. (2009) also examined the effects of particle breakage on shear strength with MGM using direct shear tests. They found that shear strength parameters of the MGM were dependant on the extent of particle breakage. The four types of MGM tested shared similar physical properties, except for the crushing strength of individual particles. Values of φ'_p ranged between 29.8° and 42.5°, where the difference was due only to the crushing strength of individual particles. However, Ezaoui et al. (2011)

performed a similar study using direct shear and MGM and found that φ'_p was not mainly related to particle breakage, and that the strength of individual particles had no significant effect on φ'_p. It was found here that the effect of deviatoric stress (*q*) seemed to be the major factor affecting the Hardin's breakage parameter B_r, while the mean effective stress (*p'*) may be more related to particle hardness (Ezaoui et al., 2011).

Hamidi et al. (2009) studied the effects of particle breakage on shear strength of sand-gravel mixtures using uniform Caspian Sea beach sand as the base material, while adding various amounts of rounded gravel particles less than 25.4 mm in diameter. A series of large-scale direct shear tests were performed at normal loads ranging from 150 to 450 kPa. They found that φ'_{cs} decreased with an increase in normal stress, which is due to the effects of particle crushing and the resulting change in gradation. φ'_p was also found to slightly decrease with increasing normal stress. The authors conclude that this phenomenon is directly related to particle breakage. Similar findings were made by Kikumoto et al. (2010).

Sadrekarimi and Olson (2011) examined φ'_{cs} of sands under various stress paths. They performed triaxial compression and ring shear tests on three sands: Ottawa 20/40 sand, Illinois River sand, and Mississippi River sand. Results indicated that the effects of particle breakage on φ'_{cs} largely depended on the magnitude of normal stress and extent of crushing. It was determined that an initial, constant value of φ'_{cs} was reached at low normal stresses (<100 kPa) where there was little influence from crushing and particle rolling and sliding dominated. When normal stresses increased to >150-200 kPa, crushing began to dominate and φ'_{cs} began to slightly increase as the soil's gradation progressed and angularity increased. At normal stresses > 200 kPa, φ'_{cs} eventually became constant again. This differs from results from Hamidi et al. (2009), where φ'_{cs} was found to decrease even at normal stresses >200 kPa. Scale effects, sand characteristics, test method, and/or the presence of gravel may attribute to this difference. Hattamleh et al. (2010) performed direct shear tests on Aqaba sand and found that the critical state friction angle increased with increasing particle crushing, regardless of the level of applied normal stress.

Ghafghazi et al. (2014) says that measurable breakage only starts after the soils contraction capacity is exhausted, and that breakage causes a downward parallel shift in the critical state line (CSL) which is in agreement with Daouadji et al. (2001), Muir Wood and Maeda (2008), and the magnitude of the CSL shift is directly correlated with the increase in the fines content. Overall, there seems to be some discrepancy in the literature related to the effects of crushing on the peak and critical state friction angles. More research is needed on this subject to help increase understanding.

2.6.5 Summary

This literature review explored a variety of topics related to this thesis including inherent errors in direct shear testing, various aspects of soil behaviour and composition that affect shear strength, and ways in which this behaviour can be modeled and quantified. Coulombs friction model (section 2.3.1) is an adequate method for describing stress-dilatancy behaviour of granular material in direct shear (Budhu, 2011), while the stages of shearing can be described using the 4-stage shearing model outlined by Li and Aydin (2010) for soils that do not experience significant particle breakage. Coulomb's friction model (Figure 2.5) can be used to describe the behaviour of dilatant granular soils and the effects of suppression of dilation under high confining pressure, where particle breakage is the main mechanism that allows for suppression of dilation (McDowell & Bolton, 1998). Particle crushing is predominantly caused by the tensile splitting of individual particles, which tend to vary statistically about a mean value due to the varying extent of internal flaws per particle. This variance can be described using Weibull (1951) statistics (Lee, 1992), while the breakage pattern of a group of particles behaves according to the fractal theory (Turcotte, 1986). As loading on a soil sample increases, force chains are mobilized within the soil matrix which find more efficient loading pathways as the particles within them are crushed and rearrange themselves. This process causes settlement which decreases slowly with time, and is known as 'creep'.

Budhu (2011) considers φ'_{cs} to be a fundamental soil property, unique to a particular soil type; however, others report it can vary due to a number of factors. Particle shape has been shown to affect

φ'_{cs} and φ'_{p}. It is generally agreed that granular soils with more angular particles tend to have larger peak and critical state shear strength and that these effects have less influence as particle breakage increases; however, other factors such as particle size, gradation, scale effects, and particle breakage/suppression of dilation have shown less agreement in the literature. There has also been disagreement over the cause of the inherent errors present in the direct shear test. It was thought by Jewell (1989) that the non-uniformities resulting in rotation within the sample cause a reduction in shear strength, while Lings and Dietz (2004) and Potts et al. (1987) found that reducing sample rotation had little to no affect on shear strength.

Overall, the mechanical behaviour of granular soils has been well researched, but there are still open questions. This thesis attempts to provide additional laboratory research to investigate some of these questions with the hope of furthering the understanding of this topic.

Chapter 3 – Methodology

3.1 Introduction

A total of 178 direct shear tests, both large scale and small scale, were completed on three (3) different sand types having two (2) different size fractions during this laboratory testing program in order to investigate the effects of suppression of dilation on shear strength. The following sections describe the soil materials, laboratory equipment, and testing procedures used to complete the laboratory component of this thesis project.

3.2 Equipment

Direct shear tests were conducted using both a large-scale direct shear (LSDS) and small-scale direct shear (SSDS) apparatus with shear box dimensions of 12” x 12” (4” depth) and 3” x 3” (1” depth), respectively. Photographs of both the LSDS and SSDS apparatuses during testing are shown in Figure 3.1. Both devices operate under strain-controlled conditions and use a pneumatic loading system for application of normal loads. The LSDS apparatus can apply normal loads using a low load attachment (0-100 kPa) and a high load attachment (250-1000 kPa), which are transmitted to the sample through an articulated ball connection and free-to-rotate rigid top plate. A close up photograph of both loading attachments for the LSDS is shown in Figure 3.2. For the low load attachment, air pressure is controlled using a regulator mounted to the side of the shear box carriage and is fed into the piston chamber of the low load attachment through one of the two t-valve connections. A pressure transducer connected to the other t-valve connection measures the air pressure inside the piston chamber. A calibration chart is used to determine the internal pressure required to exert the desired normal load through the piston on the top plate. The high load attachment works in a similar fashion as described above, except it uses a

permanently mounted pressure transducer that is calibrated to directly provide the applied load in kN, without requiring a calibration chart. The high load attachment has a more robust frame design and is secured to the sturdy outer carriage using shear pins, while the low load attachment is mounted to the upper shear box using threaded ½ inch bolts.

The SSDS apparatus uses a dual high load and low load internal piston system to apply a full range of normal stresses (0-1600 kPa). Load is transferred through two bolts connected to a loading yoke which lowers onto the top cap. In a conventional test, the load from the yoke is transferred to the top cap through a steel ball in a 'ball and socket' type connection, allowing free rotation of the top cap during the test. A close up photograph of the conventional SSDS free-to-rotate top cap used in this study is shown in Figure 3.3. This photo also shows an aluminum plate used to extend the upper surface of the top cap to allow for measurement of top cap rotation using two linear potentiometers on the upstream and downstream sides of the top cap. Dilation and contraction were recorded through this configuration by taking an average of the two displacement readings. The photos from Figure 3.2 show a similar configuration of the linear potentiometers for measuring top cap rotation in LSDS tests.

Two modifications were made to the SSDS apparatus. Firstly, a button-type load cell was installed beneath the loading yoke on the SSDS so that the applied normal load could be measured throughout the test. This enabled a more accurate measurement of the applied stress at any given time and also allowed observation of changes in normal loading during shear. For conventional tests, an aluminum loading block was designed to properly transfer the load from the button load cell through the 'ball and socket' connection to the top cap (see Figure 3.3). Second, a new rigid top cap was fabricated to fit snugly in upper shear box and to properly seat the tip of the button load cell. A setscrew was installed, which could be tightened to create a more rigid connection between the top cap and load cell/loading yoke system, thereby restricting rotation of the top cap. Limiting the rotation of the top cap is thought to limit unwanted

dilation, and may help reduce non-uniformities and increase symmetry in the test as suggested by Jewell (1989).

Data from the potentiometers, button load cell and shear (S-type) load sell were collected using a Phidget Bridge (1046_0B) and LabVIEW 2018 software at approximately 1 second intervals. A schematic and photograph showing the SSDS apparatus including modifications are shown in Figure 3.4. Due to time constraints, similar modifications were not completed for the LSDS apparatus.

Figure 3.1 – Photographs of the LSDS with the high load attachment (left) and SSDS (right) apparatuses.

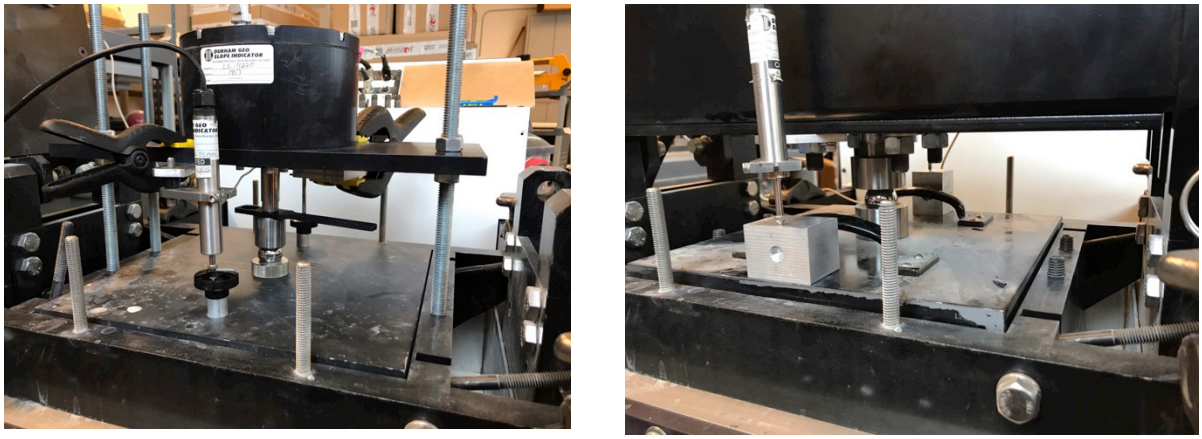

Figure 3.2 – Photographs of the low load attachment (left) and high load attachment (right) for the LSDS apparatus. Configuration of the linear potentiometers used to measure dilation and rotation of the top cap are also shown.

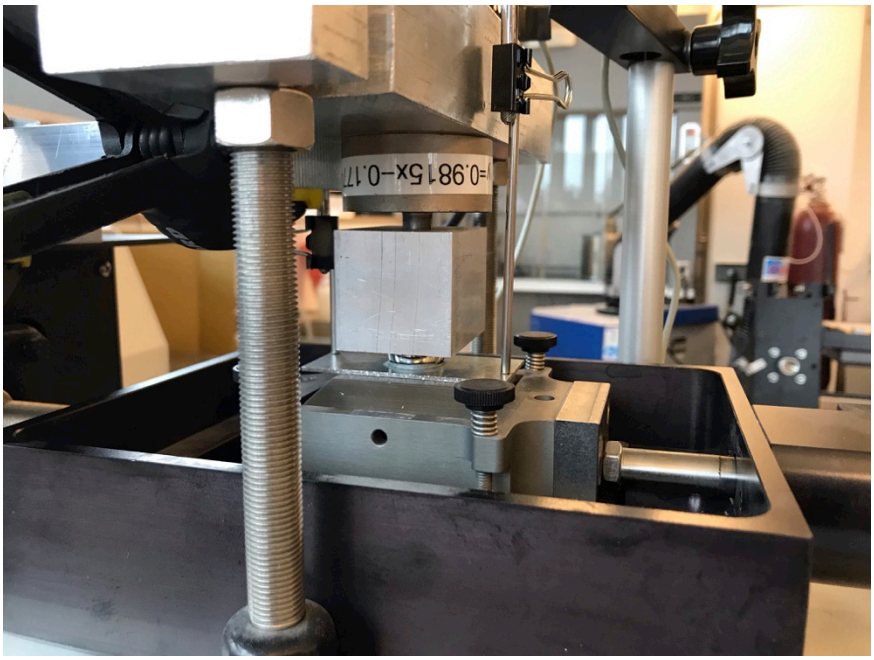

Figure 3.3 – Photograph of SSDS test setup using conventional free-to-rotate top cap, showing the configuration of the linear potentiometers for measuring dilation and top cap rotation.

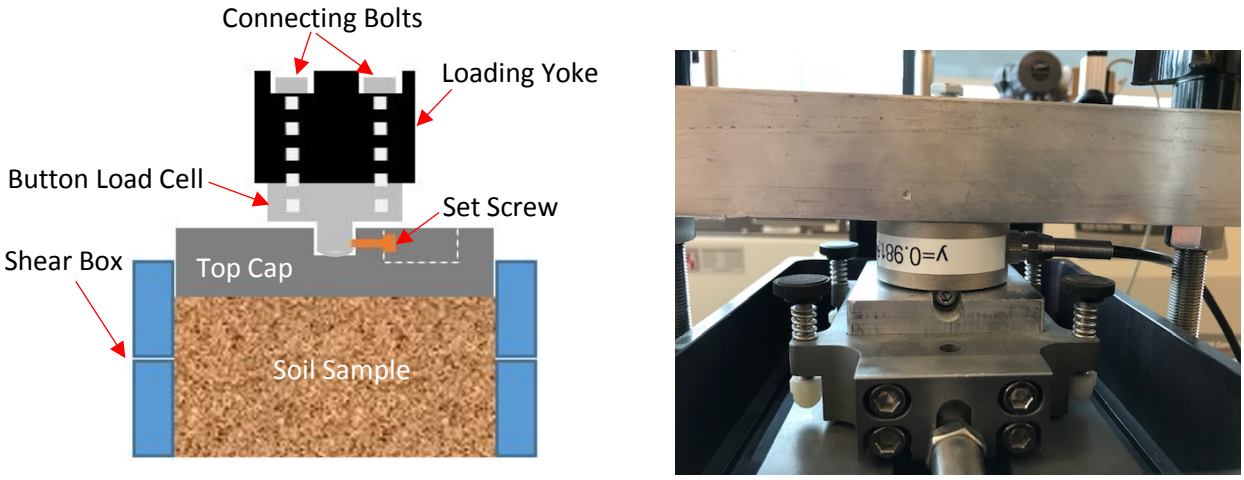

Figure 3.4 – Schematic (left) and photograph (right) of SSDS shear box with modified top cap ready for testing.

3.3 Materials

Particle breakage is known to be the dominant mechanism in the suppression of dilation at high loads. Therefore, the soils selected for this study were required to be crushable and to show a significant amount of particle breakage during shearing within the range of normal stresses capable of the SSDS and LSDS equipment at the Bergeron Center. 1-D crushing tests were performed on nine (9) different sand

types materials to determine their crushability. Of these, three (3) were determined to be suitable for this study: crushed limestone sand, Kling sand, and Poraver expanded glass beads. Crushed limestone is carbonate sand having a sub-angular to angular shape and low sphericity as defined by Powers (1953). Kling sand was provided by the Ministry of Transportation of Ontario (MTO) and is approximately 85% carbonate and 15% silicate rock and mineral types with sub-rounded to sub-angular particles. Poraver expanded glass has rounded particles and generally has a high sphericity. A summary of the material properties for the abovementioned soils is shown in Table 3.1. It should be noted that the specific gravity for Poraver was determined on beads crushed into a powder and so would be much lower when the particles are porous and intact. Limestone and Kling sands were separated into a coarse fraction (2.36 – 4.75 mm) and medium fraction (1.18 – 2.36 mm) using a Gilson mechanical sieve shaker (see Figure 3.5), while the manufacturer had separated the Poraver into slightly different coarse (2 – 4 mm) and medium (1 – 2 mm) fractions. The range of each soil fraction is small enough such that the gradation is relatively uniform (i.e. poorly graded). Gradation curves for each soil type are shown in Figure 3.6 and magnified photographs of each soil type are shown in Figure 3.7.

Table 3.1 – Soil properties for the granular materials tested in this study.

Soil	Fraction	Range (mm)	G_s	D_{50}	C_u	C_c	Crushability
Kling	Medium	1.18 - 2.36	2.76	1.4	1.36	1.02	Medium
	Coarse	2.36 - 4.75		3.2	2.69	1.85	
Limestone	Medium	1.18 - 2.36	2.73	1.4	1.36	0.87	High
	Coarse	2.36 - 4.75		3.2	2.83	1.79	
Poraver	Medium	1.0 - 2.0	2.37*	1.2	1.81	1.29	Very High
	Coarse	2.0 - 4.0		2.2	1.3	0.85	

*Specific gravity for Poraver expanded glass was determined with porous beads crushed into powder form

Figure 3.5 – Gilson sieve shakers used to separate coarse and medium fractions of limestone and Kling sand.

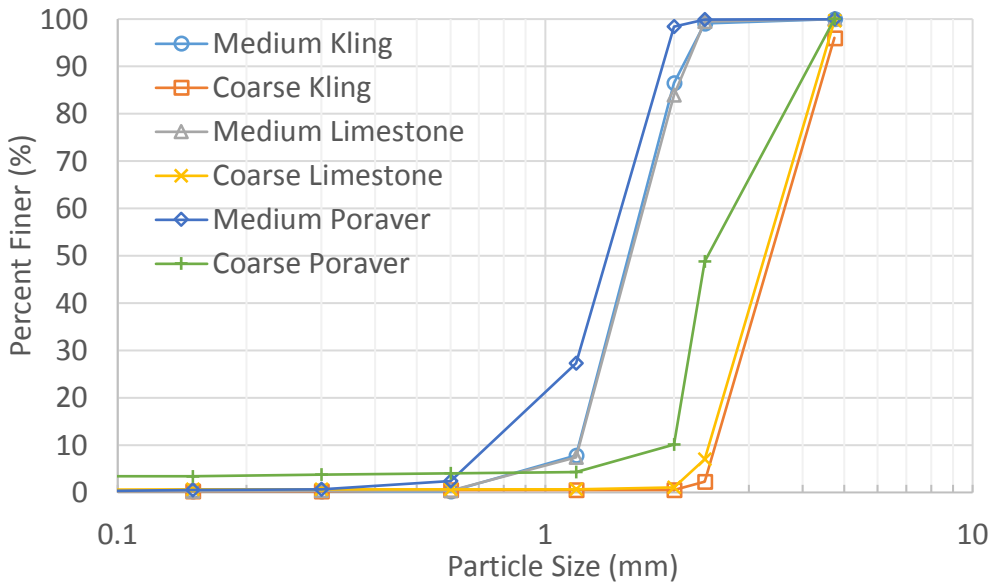

Figure 3.6 – Gradation curves for the six (6) soils used in this study.

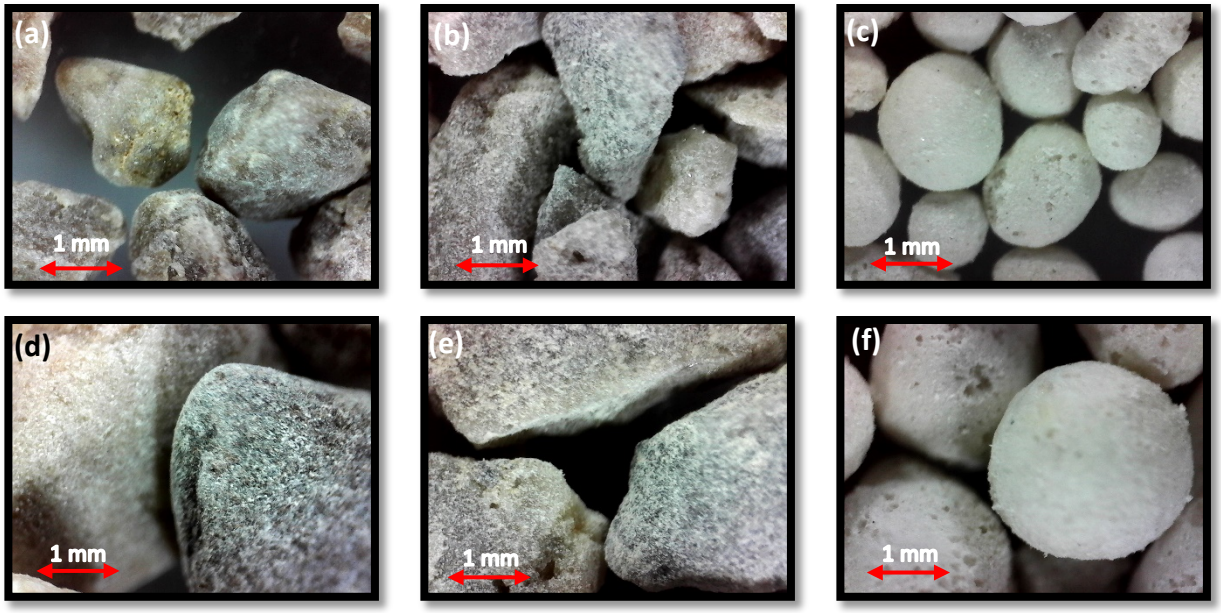

Figure 3.7 – Magnified photographs (86x) of the soils used in this study. a) Medium Kling, b) Medium Limestone, c) Medium Poraver, d) Coarse Kling, e) Coarse Limestone, and f) Coarse Poraver.

3.4 Sample Preparation and Test Procedure

For the SSDS testing, soil samples were poured into the shear box in an air-dried state using a scoop and funnel, keeping a constant drop height of about 1 cm. Given the larger sample size for the LSDS, soil was placed directly using the scoop while maintaining a similar drop height. Photographs showing the soil placement technique for both SSDS and LSDS tests are shown in Figure 3.8. Soil was placed in three (3) equal layers and compacted 20 blows per layer using a plate tamper to achieve a consistent medium-dense compaction. The middle layer was positioned such that its centerline was approximately located along the plane of shearing. Care was taken to level the sample surface prior to tamping each lift to ensure uniform compaction of the sample, and to have a level surface for the top cap to transfer a relatively uniform (initial) normal stress on the sample. 160 direct shear tests were performed at normal stresses of 25, 50, 75, 400, 500, and 600 kPa for both the SSDS and LSDS in order to capture the soil behaviour in both low load range and high load range where suppression of dilation and particle breakage could be observed. Normal stresses were limited to <600 kPa in order to avoid overstressing of the shear load cell on the LSDS apparatus. In general, SSDS tests were performed in triplicate and LSDS tests were performed

in duplicate for additional accuracy when determining friction angles. Sieve analyses were performed before and after shearing using 8" standard ASTM sieves and mechanical sieve shaker (see Figure 3.9) to determine the extent of particle breakage. The sieves were carried out on combined samples from triplicate or duplicate tests in order to capture the average representative gradation change at each normal load. Triplicate SSDS samples when combined were generally small enough to sieve the entire combined samples. Duplicate LSDS samples when combined were much larger and so were quartered, and then split multiple times using a sample splitter until the sample was reduced to 200-500 g. A shearing rate of 1.27 mm/min was used for both SSDS and LSDS tests. Soils were air-dry during testing.

Figure 3.8 – Photographs showing sample placement technique for medium Kling sand in SSDS (left) and medium limestone in LSDS (right).

Figure 3.9 – Photograph of 8" ASTM sieve stack and mechanical rotary sieve shaker used during the lab program.

Six (6) additional SSDS tests and 1D compression tests were completed using the same 3" square shear box at normal stress of 1600 kPa, in order to compare extent of particle breakage caused by shearing versus that caused only by compression. Twelve (12) cyclic SSDS tests were added towards the end of the testing program to provide additional clarity regarding the soil behaviour at critical state for select samples.

A gap was created between the upper and lower shear boxes prior to shearing for both SSDS and LSDS tests. This gap was generally made after the application of the normal load to minimize disturbance near the plane of shearing, with the exception of the low load LSDS tests. The low load frame for the LSDS is physically attached to the upper shear box, and so the upward movement of the upper shear box must be locked and finalized prior to applying the normal load. Therefore, some additional disturbance near the shear zone due to boundary friction may be present.

Chapter 4 – Results and Discussion

4.1 Introduction

Results from the direct shear tests, 1D compression tests and subsequent sieve analyses on the six (6) different soil specimens are presented in the following sections. Discussion of the results is focused on the effects of suppression of dilation on shear strength (both peak and critical state) as they relate to particle shape, particle breakage, and sample size. Results on the effectiveness of restricting rotation of the top cap are also presented and discussed.

4.2 Direct Shear Results

A total of 178 direct shear tests, both small-scale (SSDS) and large-scale (LSDS), were performed on Kling sand, crushed limestone, and Poraver expanded glass beads. The results of these tests, including pre and post-shearing sieve analyses are presented in this section. Results from the six (6) 1D compression tests completed using the SSDS shear box and loading mechanism are also included in this section. LSDS tests were not conducted on Kling sand due to limited time and material quantity. A complete set of sieve analysis results, including at low normal stresses, can be found in Appendix A, while a table summarizing the shear strength data from all 178 direct shear tests can be found in Appendix B.

Direct shear tests were completed at 25, 50 and 75 kPa in the low load range and 400, 500 and 600 kPa in the high load range, with one test completed at 1600 kPa on the SSDS apparatus to compare with 1D compression data, which was also performed at 1600 kPa using the SSDS shear box. Generally, measured normal stresses were within 5 kPa of the nominal value for both high load and low load SSDS tests. For the LSDS apparatus, normal stresses were within 1 kPa of the nominal value for low load tests and 10 kPa from the nominal value for high load tests. It should be noted that while the nominal normal

stress values are shown when presenting the data, the average normal stress measured by load cells/pressure transducers were generally used when compiling the data. It is also worth noting that initially, shear displacements for LSDS tests were set at 35 mm and later changed to 50 mm to try and better capture large strain behaviour. Due to time constraints, it was not feasible to retest those run at 35 mm. Stress-strain curves are presented using shear stress values normalized by normal stress.

4.2.1 Kling Sand

Graphs showing the stress-strain and dilatancy behaviour of Coarse Kling sand after a series of SSDS tests are presented in Figure 4.1. Figure 4.1a and 4.1b shows the normalized shear strength versus shear strain relationship at the low and high normal stress range, respectively. Coarse Kling exhibited peak behaviour followed by strain softening, typical of a medium-dense or Type B granular soil (Budhu, 2011). Fluctuations in shear strength are observed as the sand was sheared, which are more prominent at lower normal stresses. This is due to the net effect of the movement of particles into voids (local contraction) and particle interlocking (leading to local dilation) (Li & Aydin, 2010). This effect is muted at higher normal stresses since the movement of individual particles is more restricted, and particle breakage begins to occur.

Figures 4.1c and 4.1d show the vertical displacement versus shear displacement relationship. Typical geotechnical sign convention is used where dilation is negative and compression is positive. Although it is difficult to tell from the graph, a very small initial contraction occurs followed by dilation until critical state or constant volume is reached. This is also typical of Type B soil behaviour (Budhu, 2011). It is evident from Figure 4.1c and 4.1d that increasing normal stress results in suppression of dilation. Approximately 1 mm of dilation was suppressed in the high stress tests when compared to low stress. This majority of this reduction can be attributed to forced particle rearrangement, since only a minor amount of particle breakage was observed in the high stress range, as shown from the sieve analyses performed before and after shearing in Figure 4.2.

While it appears that a (reasonably) constant volume has been achieved from the dilation curves, the stress-strain curves show inconsistent critical states at low stresses and that the critical state has yet to be reached at high stresses. Cyclic tests were performed to attempt to better quantify the critical state for Coarse Kling sand. The results of these tests will be presented and discussed in Section 4.5.1.

Normalized stress-strain and dilatancy curves determined from SSDS tests on Medium Kling sand are shown in Figure 4.3. Figure 4.3a and 4.3b show Type B soil behaviour similar to that observed for Coarse Kling; however, the fluctuations in shear strength observed for both low and high stresses are noticeably less. Particle size is likely the reason for this, since smaller particles can rearrange themselves with less overall movement than larger particles. Another trend that is more noticeable in the Medium Kling sand, although also present in Coarse Kling (see Figure 4.1), is that peak normalized shear strength reduces as the normal stress increases. Dilatancy is also observed to decrease with increasing normal stress as shown in Figure 4.3c and 4.3d (and Figure 4.1c and 4.1d). This behaviour can be explained through Coulomb's friction model presented in Chapter 2 (Figure 2.4 and Figure 2.5). The failure envelope for soils that exhibit Type B behaviour is actually curved until dilation is fully suppressed. Once dilation is fully suppressed, a Type B soil will begin to behave more like a Type A soil. Therefore, for Kling sand, larger normal stresses are required to fully suppress dilation, and for the stress-dilatancy behaviour to become more like a Type A (i.e. strain hardening).

From the sieve analyses presented in Figure 4.4, particle crushing also seems to have minimal impact on the behaviour for Medium Kling sand.

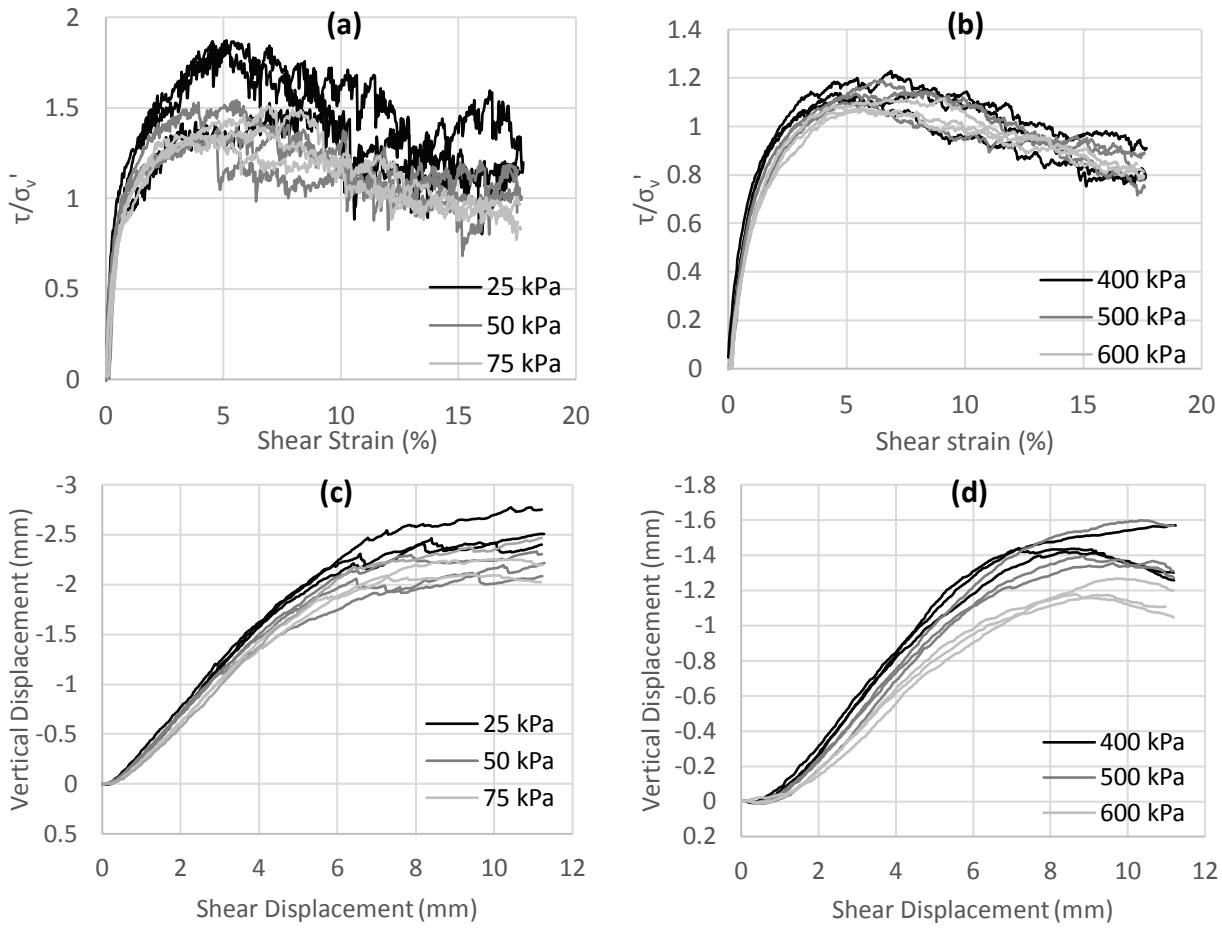

Figure 4.1 - Data from SSDS tests performed on coarse Kling sand. Normalized shear stress vs. shear strain (a and b) and vertical displacement vs. shear displacement (c and d).

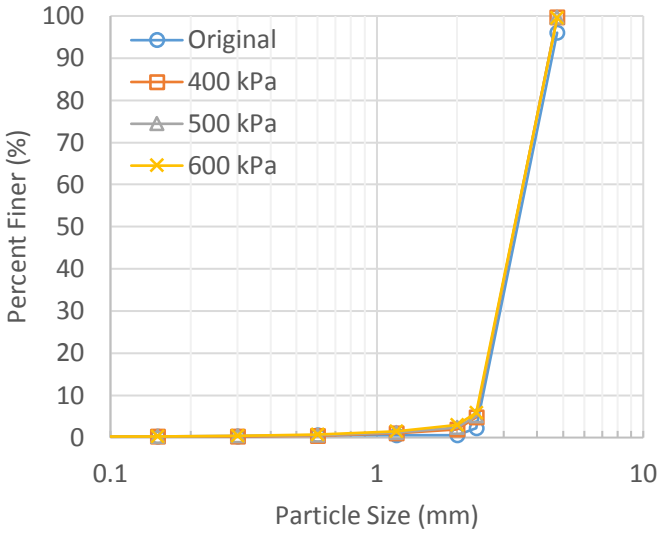

Figure 4.2 - Sieve analyses for Coarse Kling sand after high stress SSDS tests.

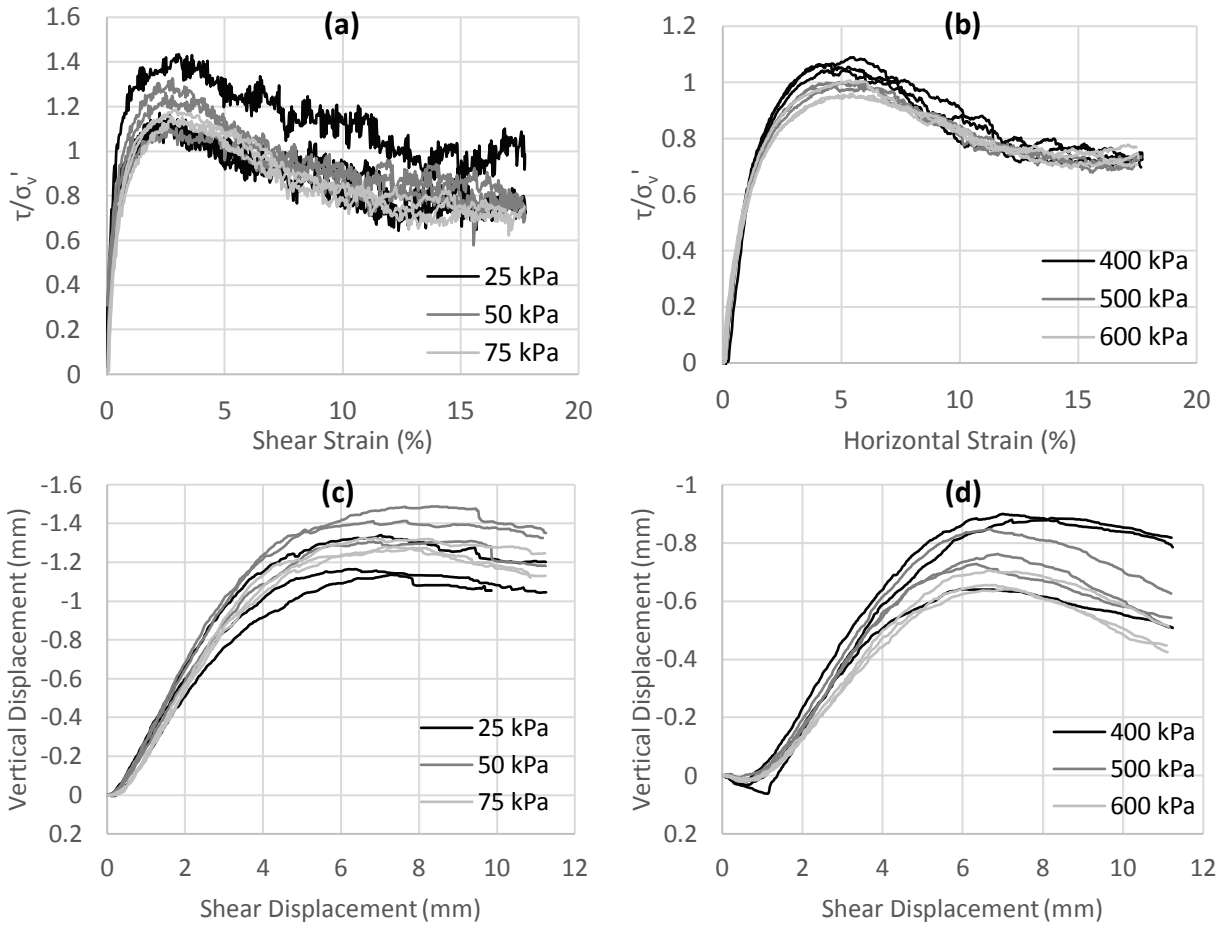

Figure 4.3 – Data from SSDS tests performed on Medium Kling sand. Normalized shear stress vs. shear strain (a and b) and vertical displacement vs. shear displacement (c and d).

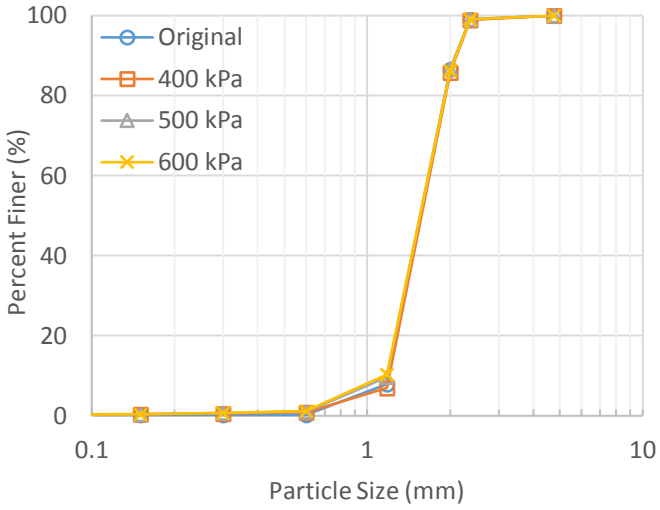

Figure 4.4 – Sieve analyses for Medium Kling sand after high stress SSDS tests.

4.2.2 Crushed Limestone

Both SSDS and LSDS tests were conducted on Coarse and Medium Limestone sand. The results of these tests are presented and discussed in the following subsections.

4.2.2.1 SSDS Tests

Stress-strain curves and dilatancy curves from SSDS tests conducted on Coarse Limestone are presented below in Figure 4.5. Compared to Coarse Kling sand, the stress-strain curves for Coarse Limestone have a less pronounced peak (Figure 4.5a and 4.5b). For this to be true at lower normal stresses, sample void ratio likely plays a role. Average bulk density of Coarse Kling was 1.57 g/cm^3, and 1.43 g/cm^3 for Coarse Limestone. Since particle size, compaction effort and specific gravity are similar for both materials, the difference in density is related to void ratio (i.e. packing). Limestone particles have a broader range of sphericity (mix of both spheroidal and elongated) than that of Kling, making them less efficient for packing (Cho et al., 2006) and therefore behaves more like a 'loose' or Type A soil than Kling sand. This might also explain the lack of well-defined peak for high stress cases in Figure 4.5b. However, when viewed in conjunction with the dilatancy curves (Figure 4.5c and 4.5d), it appears that stress-strain behaviour may be near the transition from Type B to Type A. This is because suppression of dilation is nearly total at a normal stress of 600 kPa.

Figure 4.5c and 4.5d both show suppression of dilation increasing with increasing normal stress. For the high stress cases, contractive behaviour is more prevalent for Coarse Limestone than for Coarse Kling. This is because limestone is more susceptible to particle breakage, as shown by the sieve results in Figure 4.6. Significant changes in gradation were observed after shearing, even for normal stresses <600 kPa.

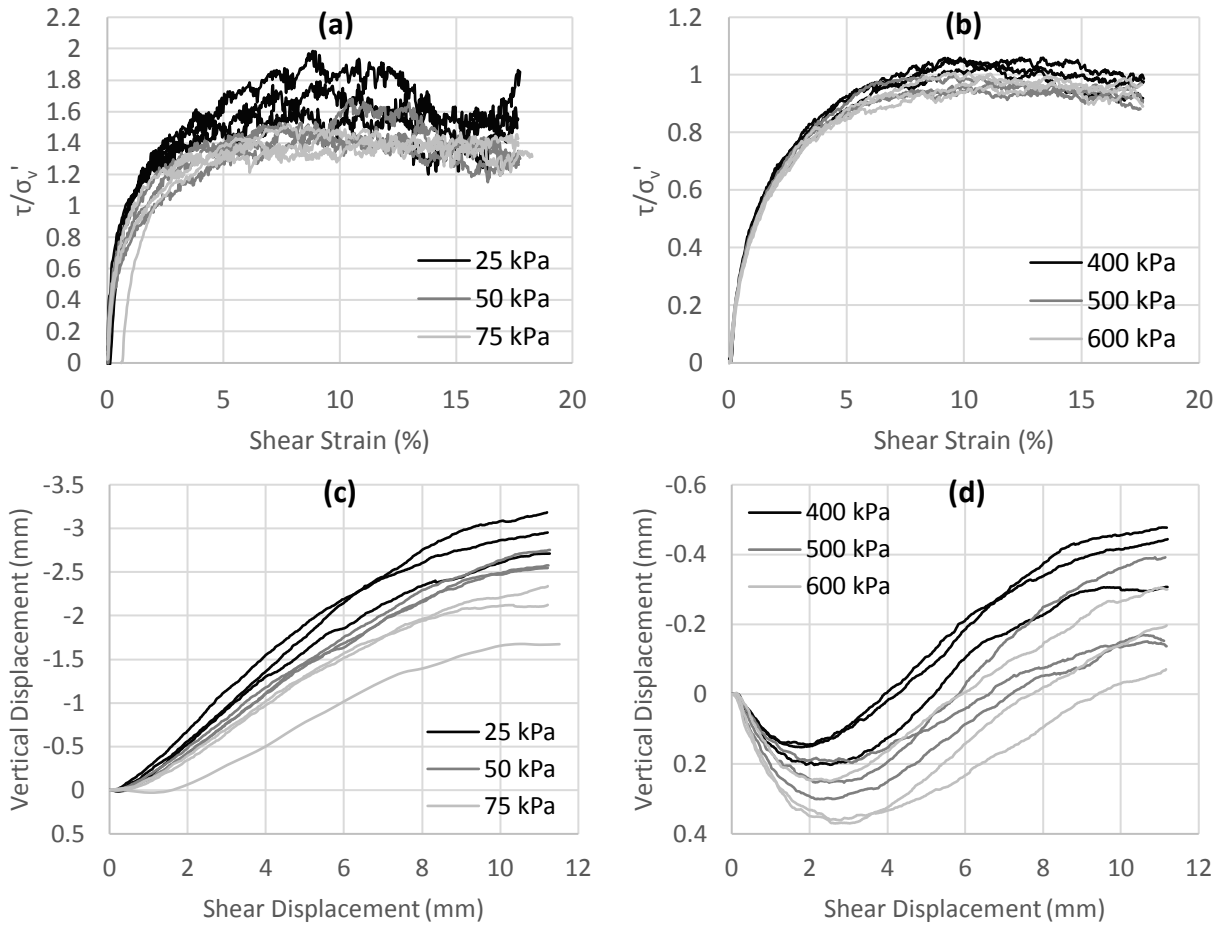

Figure 4.5 – Data from SSDS tests performed on Coarse Limestone sand. Normalized shear stress vs. shear strain (a and b) and vertical displacement vs. shear displacement (c and d).

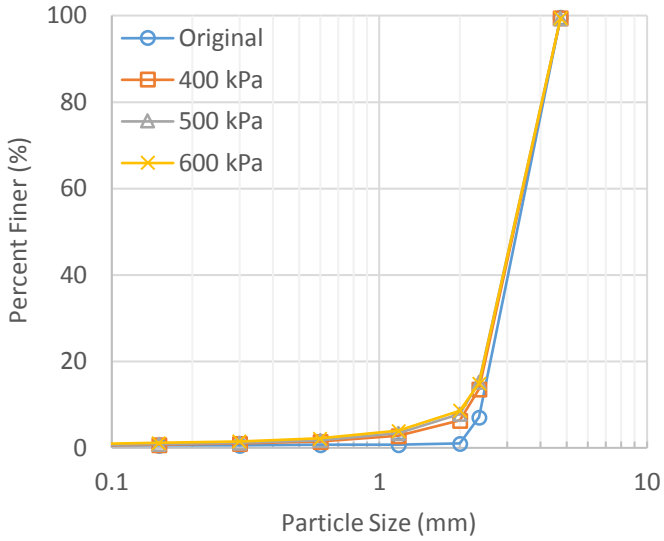

Figure 4.6 – Sieve analyses for Coarse Limestone sand after high stress SSDS tests.

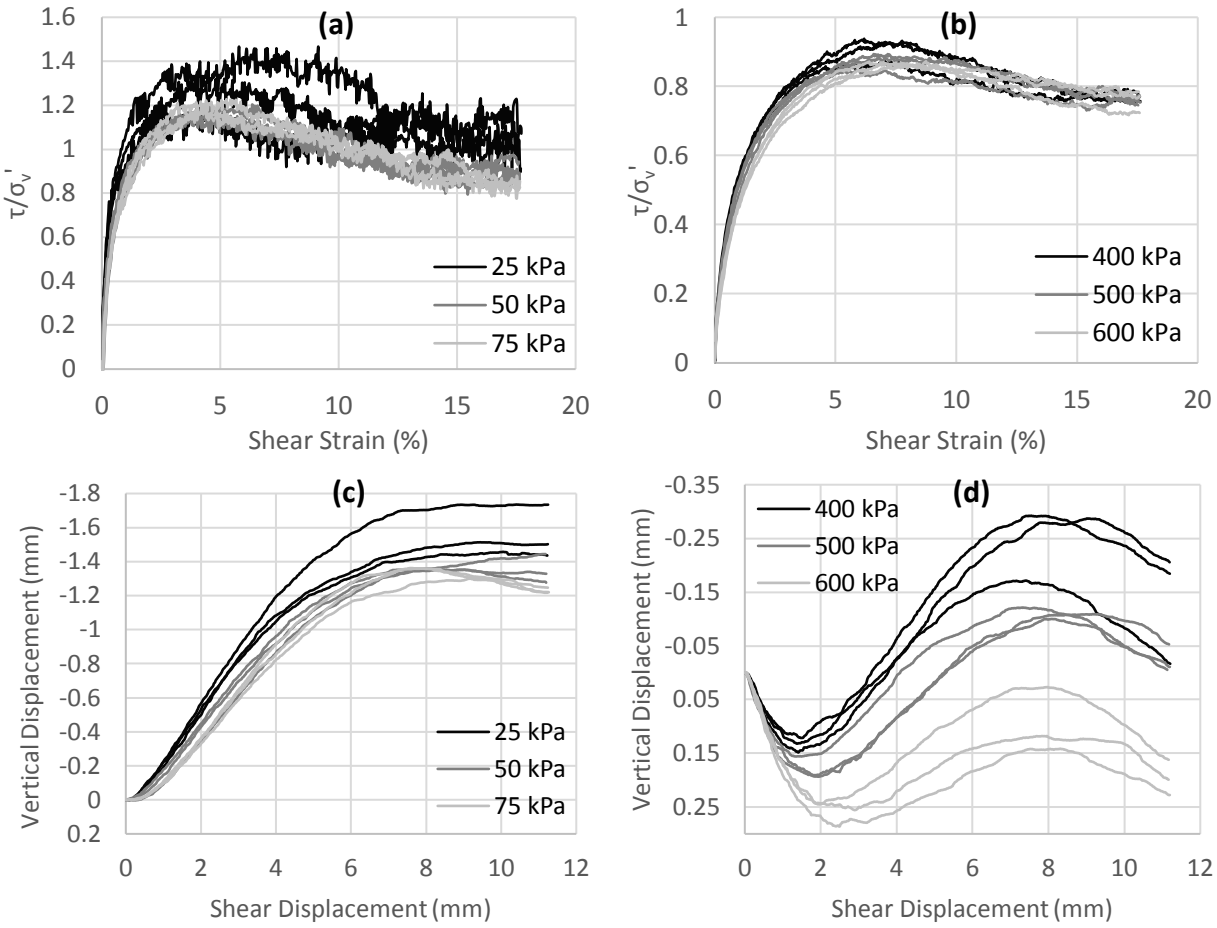

Figure 4.7 – Data from SSDS tests performed on Medium Limestone sand. Normalized shear stress vs. shear strain (a and b) and vertical displacement vs. shear displacement (c and d).

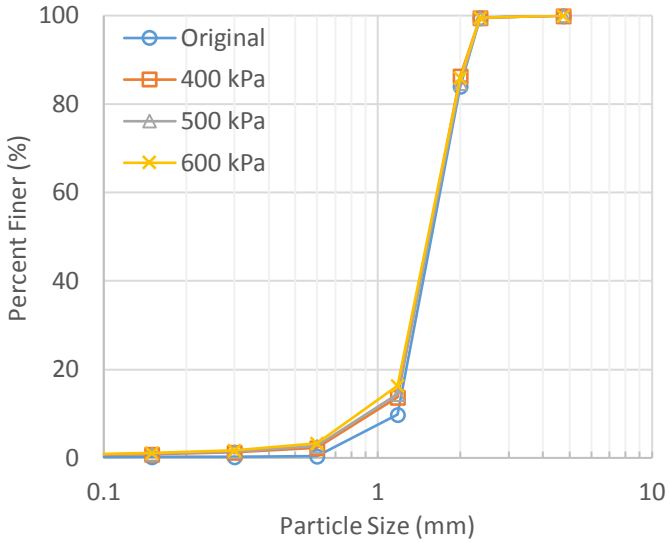

Figure 4.8 – Sieve analyses for Medium Limestone sand after high stress SSDS tests.

Stress-strain and dilation curves from SSDS tests on Medium Limestone are shown in Figure 4.7. Both low and high stress cases show more pronounced peak behaviour in Figure 4.7a and 4.7b. This is likely because Medium Limestone is able to achieve a more efficient packing (i.e. have less void space) than Coarse Limestone. At low stresses, Medium Limestone results in nearly half as much dilation as Coarse Limestone (Figure 4.5c and 4.5c), which is directly caused by the difference in particle size and smaller initial void space. For the same reason, there is also less overall dilation and therefore more contractive behaviour observed in Medium Limestone at high stresses (Figure 4.5d and 4.7d), although the maximum magnitude of contraction was slightly larger for Coarse Limestone than for Medium Limestone. The shapes of the dilation curves for both Medium and Coarse Limestone are similar; however, it appears that constant volume is reached sooner (i.e. at smaller shear strains) for Medium Limestone. This is likely due to the smaller contact surface and particle circumference, which can be overcome using less energy than larger particles.

Particle breakage for Medium Limestone depicted in Figure 4.8 appears to be similar to that of Coarse Limestone. This will be explored further in Section 4.3.

4.2.2.2 LSDS Tests

LSDS tests were conducted on Limestone and Poraver beads in order to investigate scale effects on the mechanical behaviour of crushable granular soils. Figure 4.9 shows the LSDS stress-strain and dilative behaviour of Coarse Limestone. At low stresses, varying degrees of peak stress-strain behaviour is observed along with typical Type B dilative behaviour (Figure 4.9a and 4.9c), with some minor fluctuations in shear stress due to particle rearrangement. These fluctuations seem to be significantly less when using the large shear box. It was observed that increasing normal stress results in greater suppression of dilation and reduced normalized shear stress, similar to what was observed for Coarse Limestone in the SSDS tests.

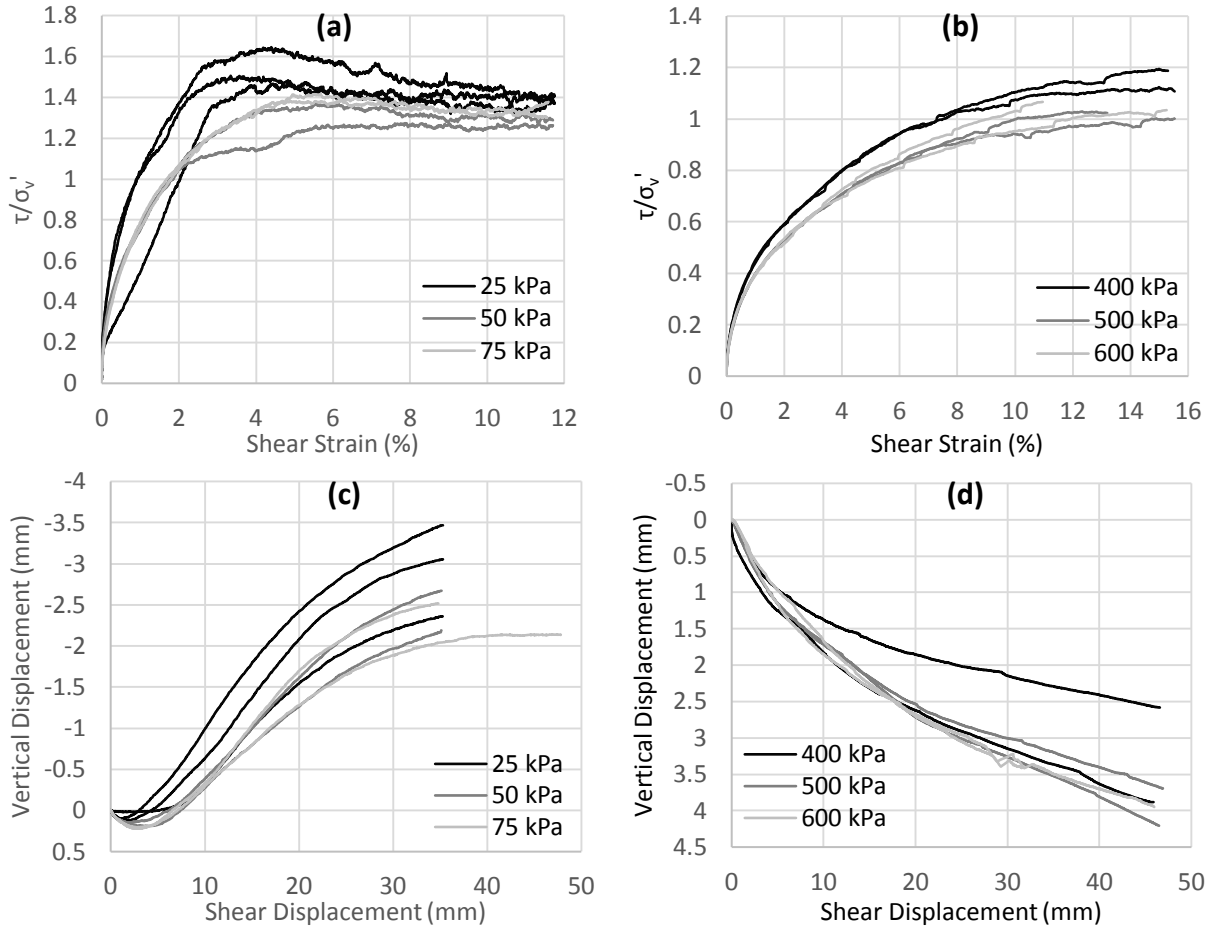

Figure 4.9 – Data from LSDS tests performed on Coarse Limestone sand. Normalized shear stress vs. shear strain (a and b) and vertical displacement vs. shear displacement (c and d).

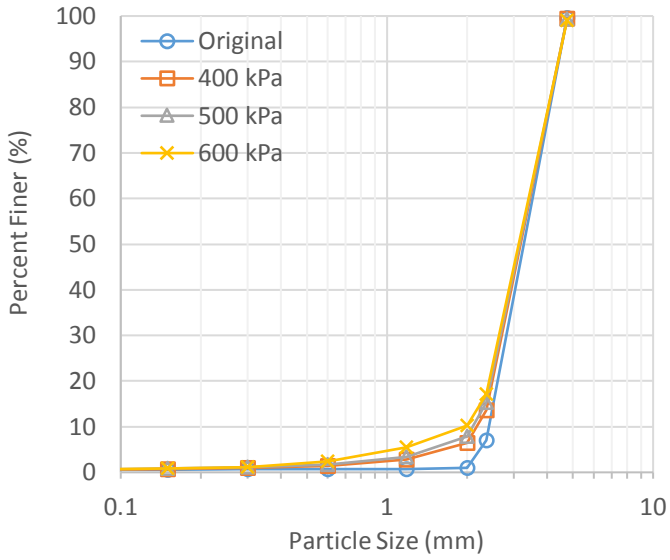

Figure 4.10 – Sieve analyses for Coarse Limestone sand after high stress LSDS tests.

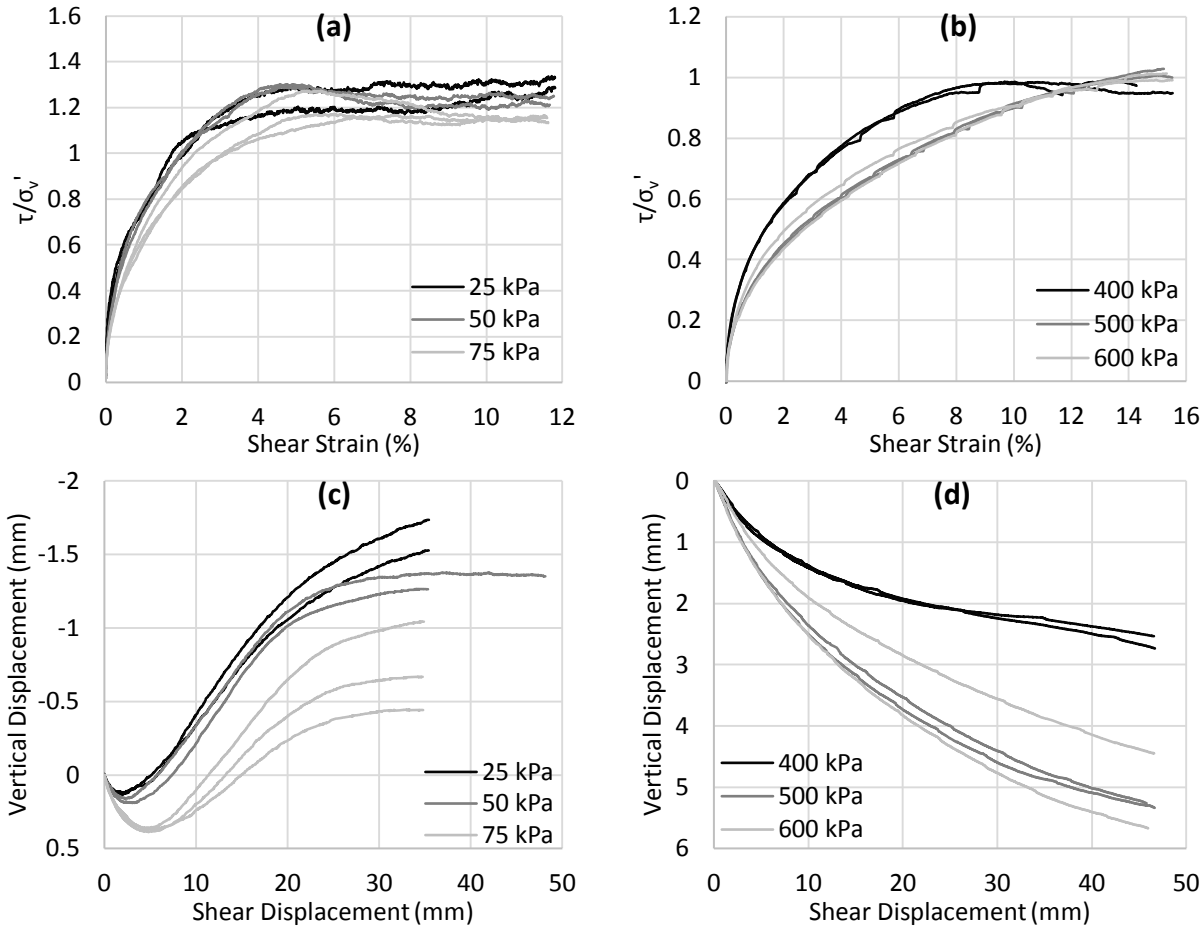

Figure 4.11 – Data from LSDS tests performed on Medium Limestone sand. Normalized shear stress vs. shear strain (a and b) and vertical displacement vs. shear displacement (c and d).

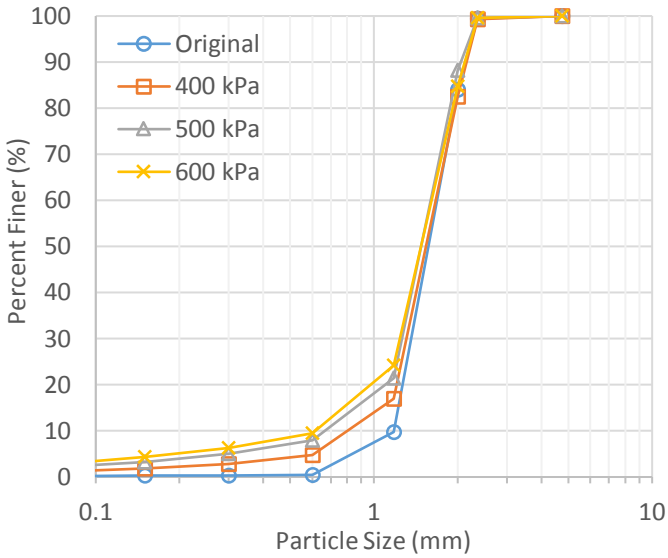

Figure 4.12 – Sieve analyses for Medium Limestone sand after high stress LSDS tests.

At high stresses, suppression of dilation is much greater for Coarse Limestone during LSDS than in SSDS tests. Figure 4.9d shows purely contractive behaviour for normal stress 400-600 kPa, meaning dilation is fully suppressed for all high load cases. Conversely, Figure 4.5d shows mostly dilative behaviour at 400 and 500 kPa, and shows a net contractive behaviour at 600 kPa while still exhibiting some dilatancy. Therefore, it appears that sample size has a significant effect on suppression of dilation. Particle breakage was also observed to increase for Coarse Limestone in the LSDS test when compared to the SSDS Test (see Figure 4.6 and Figure 4.10). This will be explored in more detail in section 4.3. Now that dilation is fully suppressed and contractive behaviour dominates, stress-strain curves shown in Figure 4.9b depict Type A behaviour.

Results from LSDS tests performed on Medium Limestone are presented in Figure 4.11 and Figure 4.12. Nearly 1.5 times more contraction was observed for Medium Limestone than Coarse Limestone using the same large shear box (Figure 4.9d and 4.11d). Reducing particle size causes reduced dilation and increased contraction behaviour in both SSDS and LSDS tests.

4.2.3 Poraver Expanded Glass Beads

Both SSDS and LSDS tests were conducted on Coarse and Medium Poraver expanded glass beads. The results of these tests are presented and discussed in the following subsections.

4.2.3.1 SSDS Tests

Stress-strain and dilatancy behaviour from SSDS tests performed on Coarse Poraver are shown below in Figure 4.13. At low stresses, typical Type B stress-strain and dilatancy behaviour were observed (Fig. 4.13a and 4.13c), while full contractive behaviour and associated Type A stress-strain curves were observed at high stresses (Fig. 4.13b and 4.13d). In all cases, increasing normal stress causes a greater reduction in normalized shear stress and suppression of dilation compared to Limestone, and an even greater reduction when compared to Kling sand. This seems to be related to the extent of particle

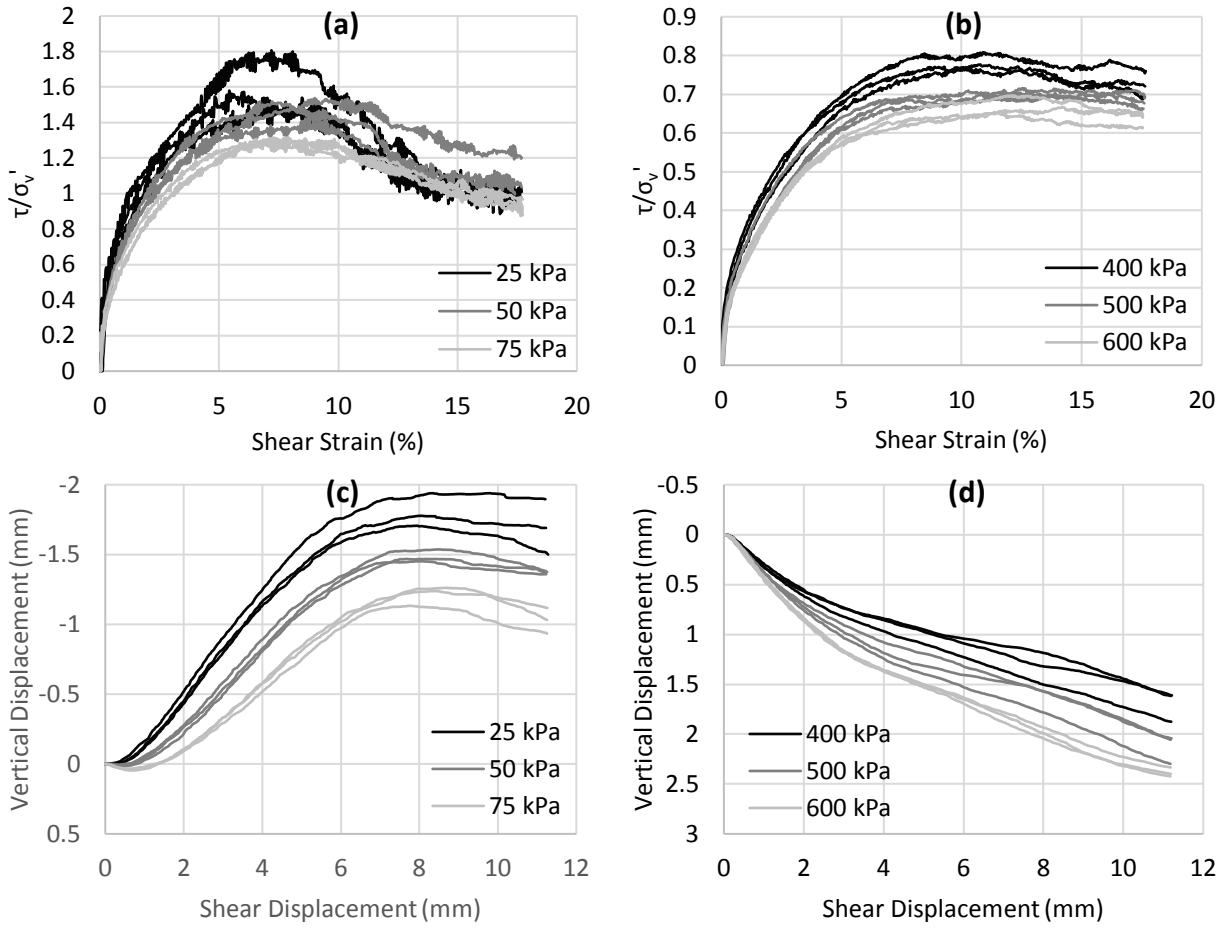

Figure 4.13 – Data from SSDS tests performed on Coarse Poraver. Normalized shear stress vs. shear strain (a and b) and vertical displacement vs. shear displacement (c and d).

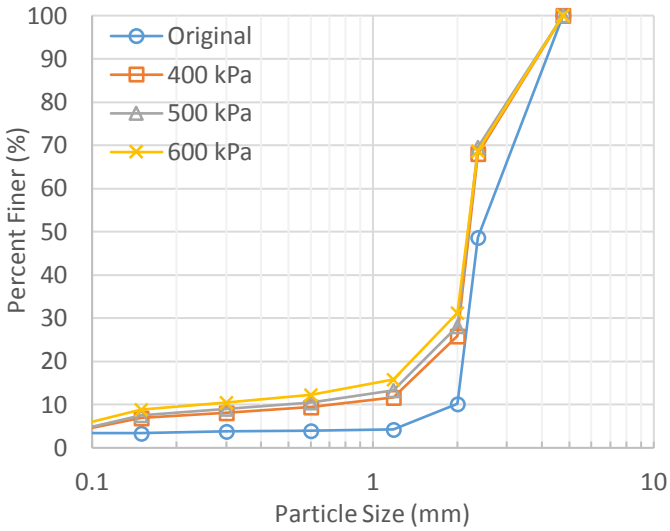

Figure 4.14 - Sieve analyses for Coarse Poraver after high stress SSDS tests.

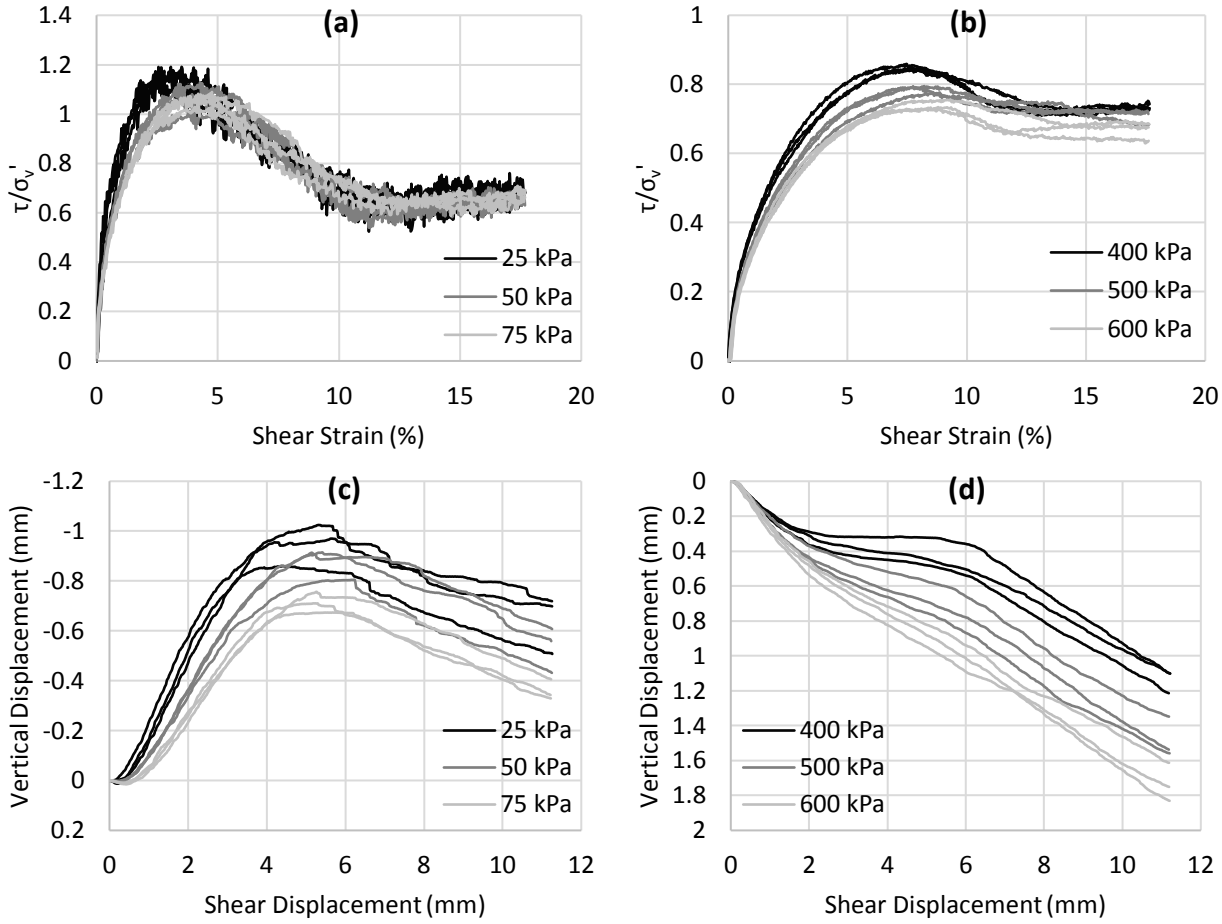

Figure 4.15 – Data from SSDS tests performed on Medium Poraver. Normalized shear stress vs. shear strain (a and b) and vertical displacement vs. shear displacement (c and d).

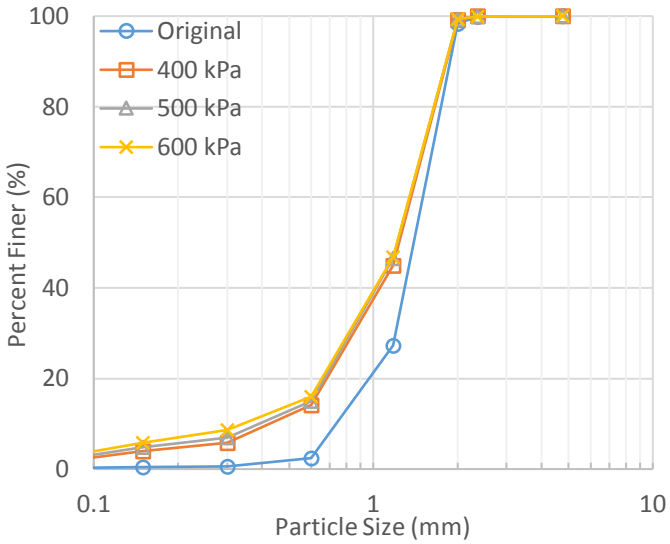

Figure 4.16 – Sieve analyses for Medium Poraver after high stress SSDS tests.

breakage exhibited by each soil type. Figure 4.14 shows the sieve analyses before and after SSDS tests for Coarse Poraver. Coarse Poraver clearly results in the largest amount of particle breakage of the three soils.

Results for SSDS tests performed on Medium Poraver are shown in Figure 4.15. As was observed with the other two soils, Medium Poraver has a better-defined peak in the stress-strain curve than Coarse Poraver (Fig. 4.15a and 4.15b), which is likely the result of more efficient packing. Despite dilation being fully suppressed under high stresses (Fig. 4.15d), peak behaviour is still observed (Fig. 4.15b). The dilation response at high stresses show plateaus that correspond to the peaks in the stress-strain curves. The plateaus indicate that some resistance to contraction is taking place, and that there must be some localised rearrangement of particles occurring during this stage of shearing. The plateaus become steeper as normal stress increases, while the peaks in the stress-strain curve also become smoothed out. At 600 kPa, Medium Poraver is nearly at the transition between Type A and Type B behaviour.

The crushability of Medium Poraver appears to be similar to that of Coarse Poraver, as shown by the sieve analysis performed before and after SSDS tests in Figure 4.16.

4.2.3.2 LSDS Tests

The stress-strain and dilation response from LSDS tests performed on Coarse Poraver are presented below in Figure 4.17. The main difference between the results of the SSDS and LSDS tests is that LSDS tests resulted in a significant increase in the suppression of dilation for both low and high stresses. This same observation was made for Limestone sand. However, since Poraver is a more crushable material, an even greater effect on suppression of dilation was observed. The reason for this likely has to do with boundary effects in the shear box. In the large shear box there is 9 inches of additional room laterally, and 3.5 inches vertically, for particles to rearrange themselves before the sides of the shear box or top cap begin to restrict this movement. In addition to this, the overall volume of voids in the LSDS sample is larger, which allows for a larger reduction in sample height when particles rearrange themselves during shear. Another factor could be that total shear displacement for all LSDS tests were 3 to 5 times

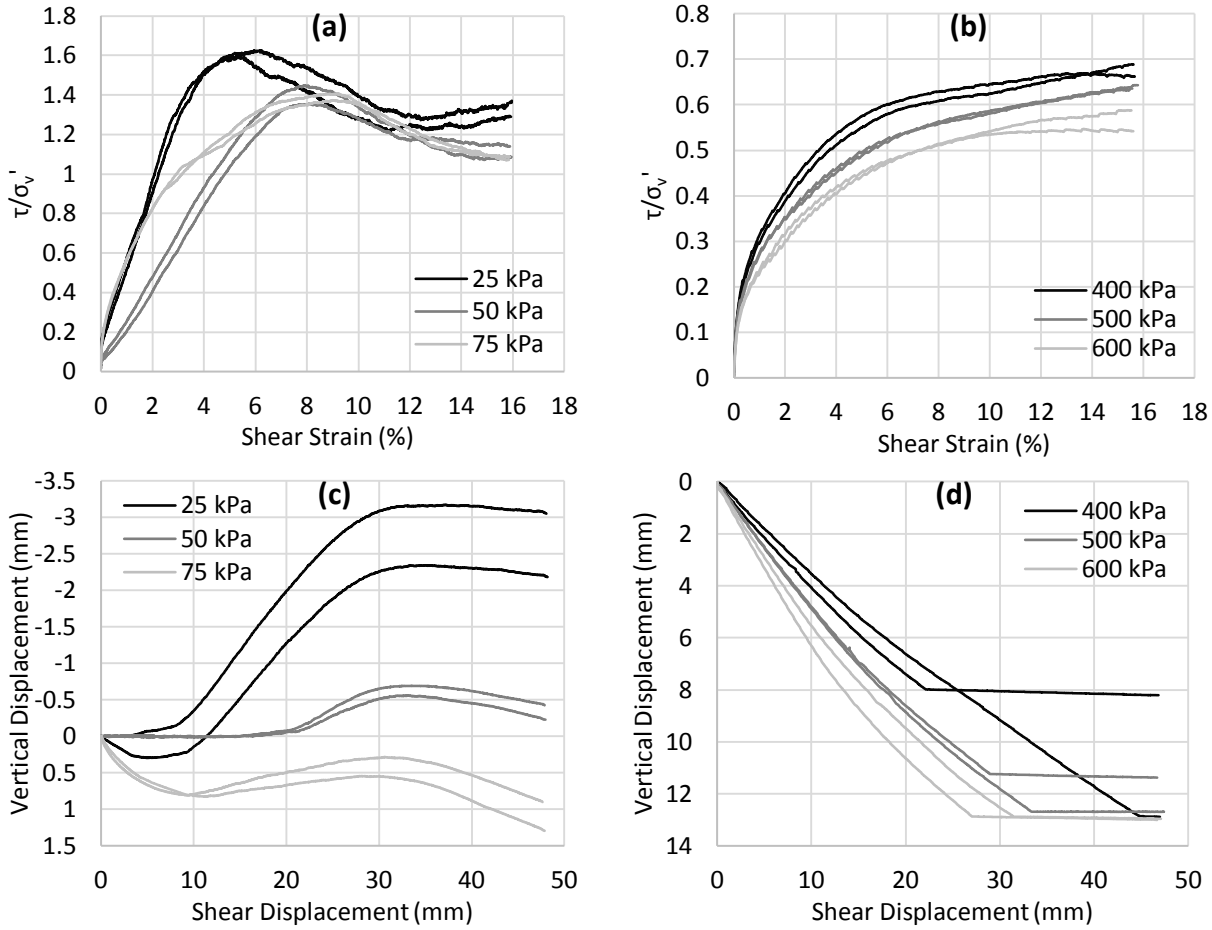

Figure 4.17 – Data from LSDS tests performed on Coarse Poraver. Normalized shear stress vs. shear strain (a and b) and vertical displacement vs. shear displacement (c and d).

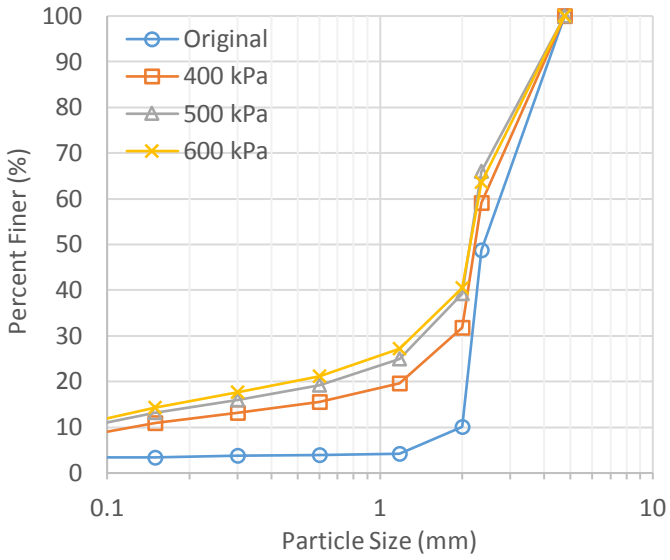

Figure 4.18 – Sieve analyses for Coarse Poraver after high stress LSDS tests.

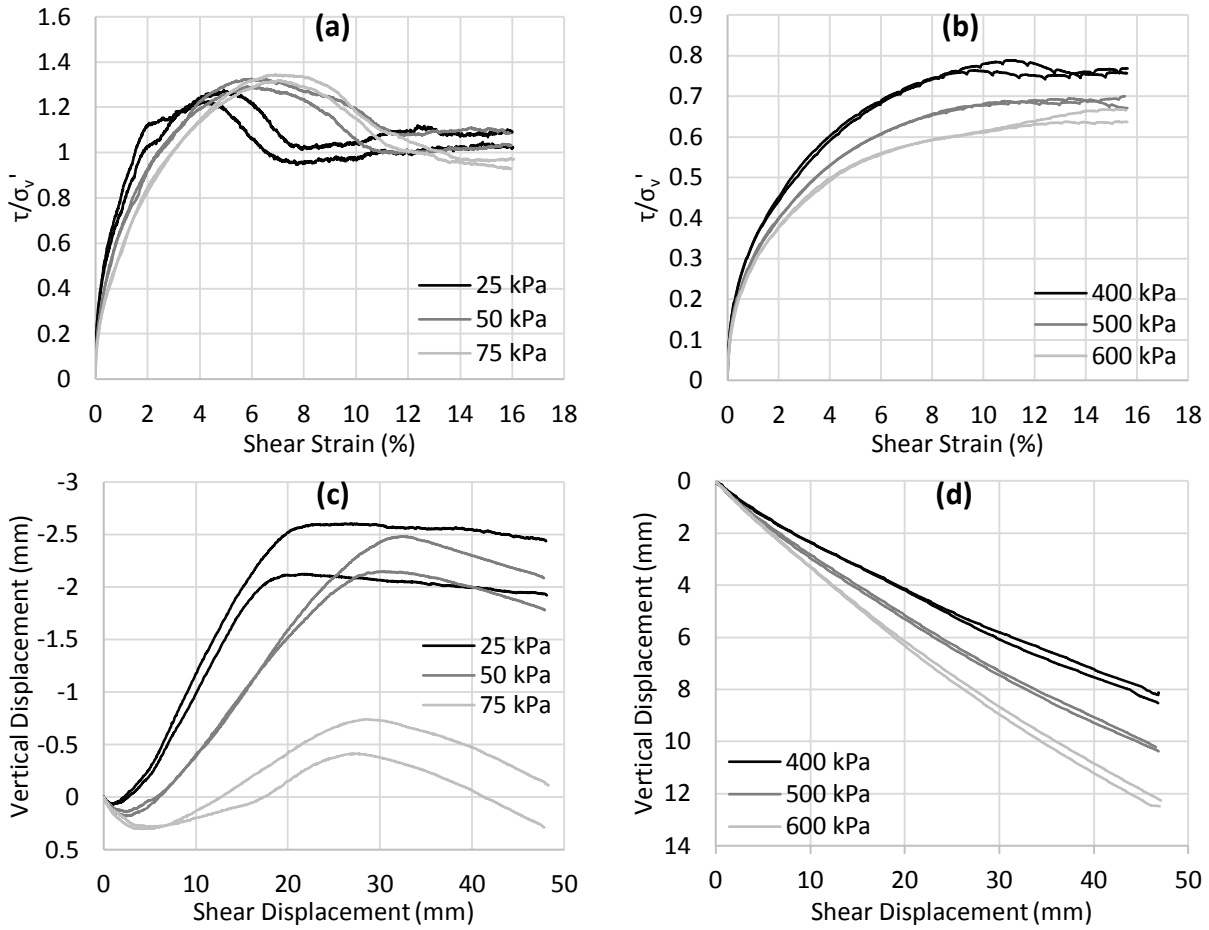

Figure 4.19 – Data from LSDS tests performed on Medium Poraver. Normalized shear stress vs. shear strain (a and b) and vertical displacement vs. shear displacement (c and d).

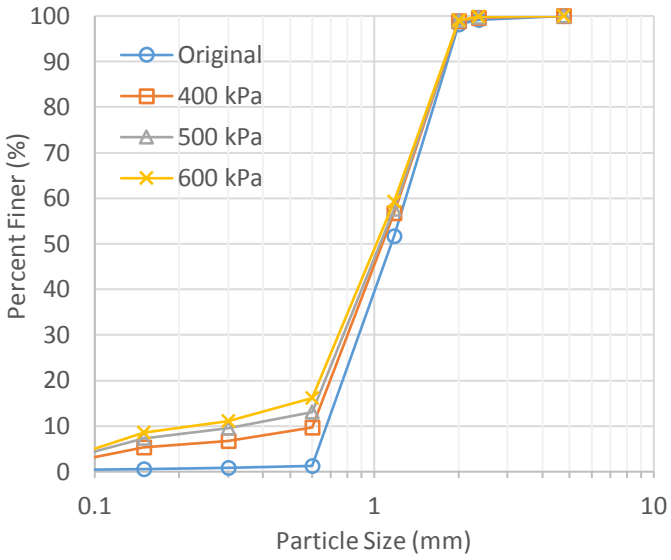

Figure 4.20 - Sieve analyses for Medium Poraver after high stress LSDS tests.

greater than SSDS tests, which would amplify the effects of dilation and crushing. For Coarse Poraver, net contractive behaviour was observed at a normal stress of 75 kPa (Fig. 4.17c). Contractive behaviour observed at higher stresses were so large they exceeded the range of the linear potentiometers used to record the displacement (Fig. 4.17d). LSDS tests on Coarse Poraver also show a notable increase in particle breakage when compared with SSDS tests (Fig. 4.18).

Results showing stress-strain and dilatancy curves for LSDS tests performed on Medium Poraver are shown below in Figure 4.19. The behaviour appears to be similar to that of Coarse Poraver, except that Medium Poraver shows less overall dilation and contraction (Fig. 4.19c and 4.19d). This is similar to what was observed in Limestone, and can be attributed to the smaller particle size of the Medium Poraver. The crushability of Coarse Poraver is larger than Medium Poraver based on the sieve analyses shown in Figure 4.18 and Figure 4.20.

4.3 Particle Breakage

To quantify the extent of particle breakage, Hardin's relative breakage (B_r) was determined for each test based on the sieve analyses performed before and after shearing. A plot of relative breakage versus normal stress is presented below in Figure 4.21. The most crushable material was found to be Poraver, followed by Limestone, with Kling sand being the least crushable. It should be noted that negligible particle breakage was detected for Limestone and Kling sand at low stresses, and so B_r values were considered not applicable and do not appear in the graph. Sieve analyses at low stresses that show negligible crushing are provided in Appendix B. Photographs of the particle breakage after SSDS tests at 600 kPa normal stress are shown in Figure 4.22. The extent of crushing is also visible from the photos, with Kling having the least amount and Poraver having the most. Photos taken at additional normal stresses can be found in Appendix C.

For SSDS tests, medium fractions for all materials appear to be slightly more crushable than the coarse fractions. This is contrary to previous studies, which observed that relative breakage increases as mean particle size increases (Lee & Farhoomand, 1967; Wang et al., 2015; Marachi et al., 1972). Since the specimens in this study are relatively uniform, the theory by McDowell et al. (1996) where the smallest particles should fracture first will not be relevant here. For Kling and Limestone sand, the medium fractions have a lower coefficient of uniformity (C_u) than the coarse gradations, and it is known that extent of crushing reduces as a soil becomes more 'well graded' (Lee & Farhoomand, 1967). However, for Poraver, the medium fraction has a higher C_u than the coarse fraction, yet it still results in more crushing. It could also be that since medium particles generally reach the post-peak stage faster than coarser particles, medium particles tend to have more time to experience crushing and thus result in higher B_r values.

For LSDS tests, it was observed that Medium Limestone had significantly more particle breakage than Coarse Limestone after LSDS tests, while the opposite was true for Poraver. Caution should be used though, when comparing the crushing behaviour of Limestone and Poraver since their material structure is fundamentally different. Limestone is a natural calcareous material, while Poraver is a manufactured material with a very porous internal structure. One interesting aspect of Poraver's crushing behaviour was observed by comparing sieve analyses before and after 1D compression tests and SSDS tests under an applied normal stress of 1600 kPa. The results of these sieve analyses are shown in Figure 4.23. Figure 4.23a and 4.23b show that particle breakage for Kling and Limestone was predominately caused by shearing, with Limestone having a slightly greater proportion caused by 1D compression. For Poraver the opposite is true (Fig. 4.23c), where a much larger proportion of the particle breakage was caused by 1D compression. In addition, 1D compression contributed to an even larger portion of particle breakage for Coarse Poraver than Medium Poraver, while the difference between Coarse and Medium Limestone/Kling was marginal. It seems that Poraver has fundamentally different crushing behaviour than Limestone or

Kling sand, which is likely due to its porous microstructure, and that its particle size effects will not necessarily follow the same behaviour as natural soils as described by fractal theory (McDowell et al., 1996). It is possible that the proportion of particle breakage caused by 1D compression might increase for Kling and Limestone at normal stresses that create a similar degree of breakage exhibited by Poraver here; however, it would almost certainly remain less than the proportion observed in Poraver.

It is also worth comparing the effects of the sample size on particle breakage for the same soil types. For example, Coarse Limestone has similar B_r values for both SSDS and LSDS tests, with a minor increase in B_r observed in the LSDS test at 600 kPa normal stress. Conversely, Medium Limestone had significantly higher B_r values in LSDS tests compared to SSDS tests. Again, with Poraver the opposite is true. Coarse Poraver had significantly higher B_r values for LSDS tests when compared with SSDS tests, while Medium Poraver had higher B_r values from SSDS tests than LSDS tests. There is clearly some effect from sample size on the amount of particle crushing, but the mechanics behind it are uncertain.

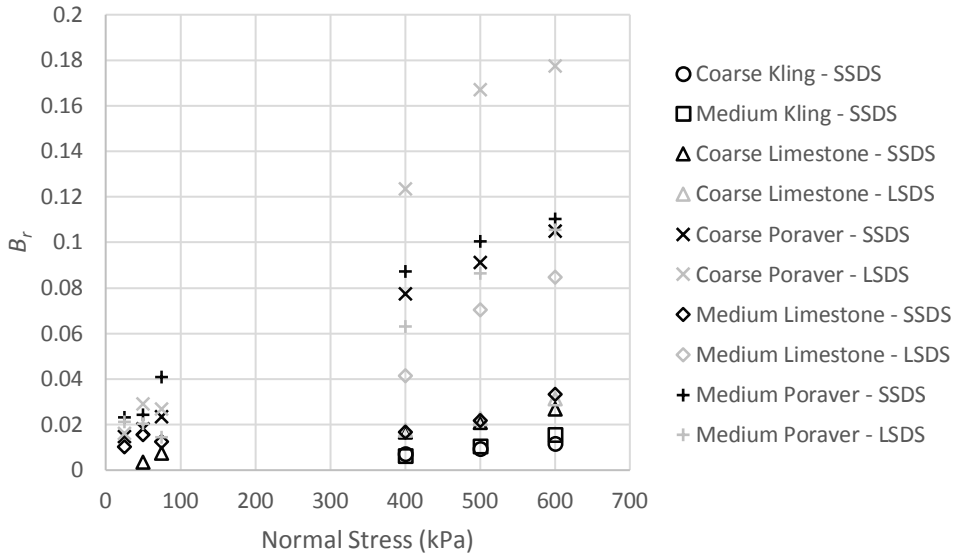

Figure 4.21 – Hardin's Relative Breakage (B_r) for various crushable soils after SSDS and LSDS tests.

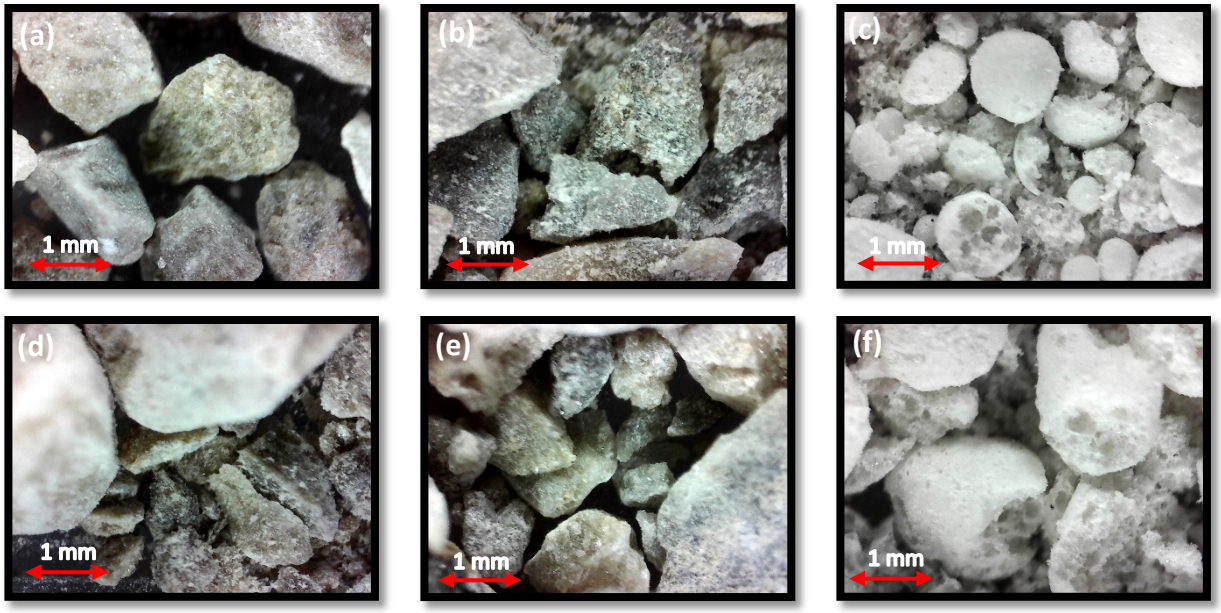

Figure 4.22 - Magnified photographs (86x) of granular materials sheared with 600 kPa of applied normal stress. a) Medium Kling, b) Medium Limestone, c) Medium Poraver, d) Coarse Kling, e) Coarse Limestone, and f) Coarse Poraver.

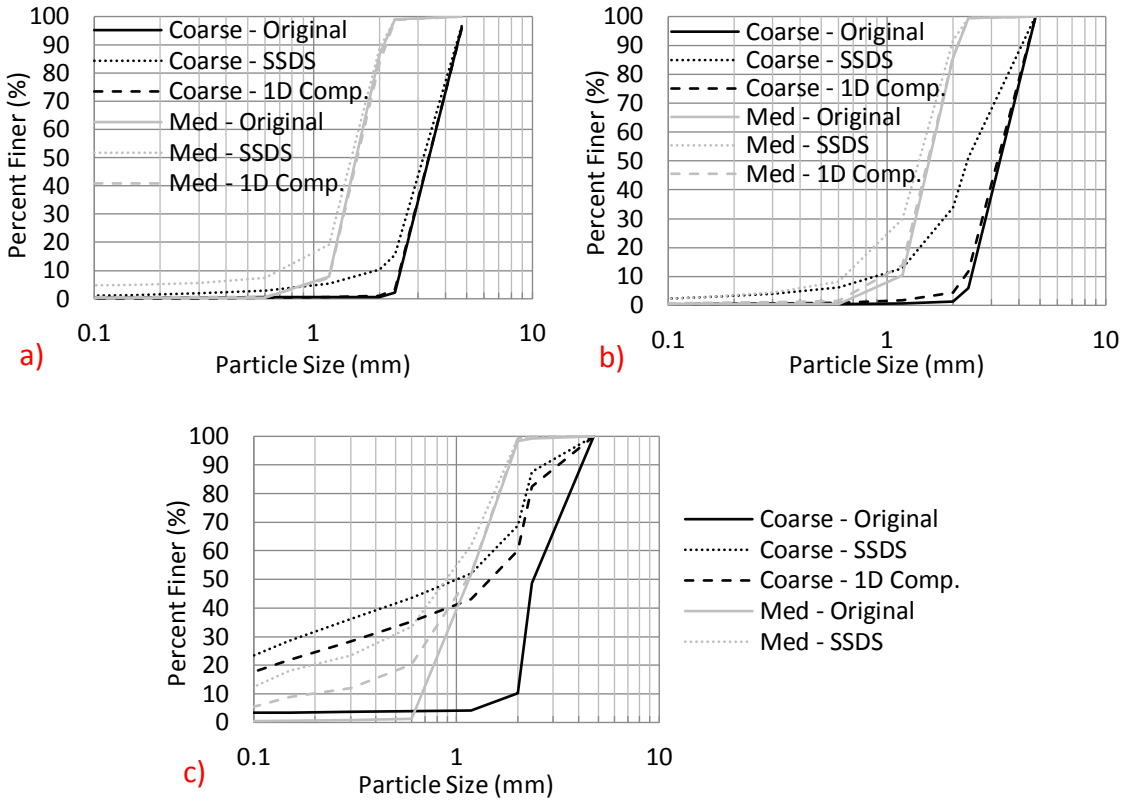

Figure 4.23 - Comparison of sieve analyses from 1D Compression and SSDS tests at 1600 kPa normal stress. a) Kling, b) Limestone, c) Poraver.

4.4 Peak Shear Strength (φ_p')

The main purpose of this thesis is to investigate the effects of suppression of dilation on shear strength of crushable granular materials. Peak shear strength values from each direct shear test were used to calculate the angle of friction using Eqn. 2.1. Figure 4.24 and Figure 4.25 show the peak friction angles (φ_p') versus average normal stress for SSDS and LSDS tests, respectively. Generally, φ_p' is highest at low normal stresses and decreases as normal stress increases. This behaviour is expected as it follows the slope of the curved failure envelope caused by the materials dilatancy (see Figure 2.5, section 2.3.1). Values of φ_p' for Coarse and Medium limestone seem to stabilize as normal stresses approach 600 kPa. This is because suppression of dilation for these soils is nearly total and they are beginning to approach their critical state (see Fig. 4.5d and 4.7d). It was also observed that, despite dilation for Coarse and Medium Poraver being fully suppressed (fully contractive behaviour) and visible Type A behaviour at high normal stresses was observed, φ_p' continued to decrease in both SSDS and LSDS tests. Based on the stress-dilatancy response of Poraver from Figure 4.13 and 4.15, the critical state had been reached at some normal stress <400 kPa, and so φ_p' should be stable throughout the high stress range, according to Coloumb's friction model; however, this is not the case here. Based on the large differences in the normalized stress-strain curves for Poraver, there are significant structural and behavioural changes occurring within this high stress range. It is likely that Poraver has reached such a large extent of particle crushing that its behaviour can no longer be described using Coulomb's friction model.

For the natural soils of Limestone and Kling sand, increasing particle size results in an increase in φ_p' for both the high and low range of normal stresses. This is in agreement with findings from Leslie (1969), Kirkpatrick (1965) and Dai et al. (2016). However, Poraver showed a decrease in φ_p' with particle size at high normal stresses, while at low stresses, Poraver behaved more like the natural soils where the larger particles resulted in higher φ_p'. Interestingly, Marachi et al. (1972) reported that triaxial tests on

natural rockfill materials with particle diameters ranging from 0.5-6 inches under normal stresses of 5 MPa showed behaviour similar to that of the 1-4 mm diameter Poraver in the 400-600 kPa range - that shear strength decreased with increasing mean particle size. They also found that this is closely related to the grain breakage intensity (Marachi et al., 1972). The similarity between the rockfill and Poraver materials in this case is the proportion of internal flaws that are present, which are directly related to their crushability. It is well established that smaller particles tend to have higher crushing strength than larger particles due to the presence of flaws. This explains the difference in behaviour observed here. The normal stresses in the 25-50 kPa range are small enough so that particle rolling and sliding dominate for all materials, including Poraver. For the high stresses in the range of 400-600 kPa, particle breakage dominates and the larger internal flaws in the Coarse Poraver results in more crushing and therefore, a lower φ_p' than Medium Poraver. This is true for LSDS tests, but SSDS test results show that Medium Poraver exhibits more crushing than Coarse Poraver, yet Medium Poraver still has a higher value of φ_p'. It is uncertain where this discrepancy originates. It should be noted that at normal stresses of 1600 kPa, Coarse Poraver clearly exhibits more crushing than Medium Poraver in SSDS tests (see Figure 4.21 and 4.23), which is what should be expected.

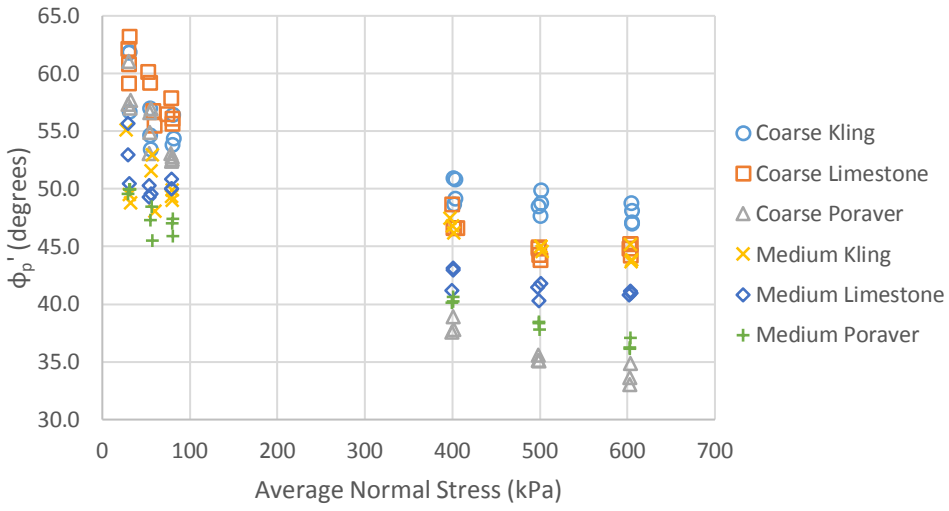

Figure 4.24 - Peak friction angles from SSDS tests.

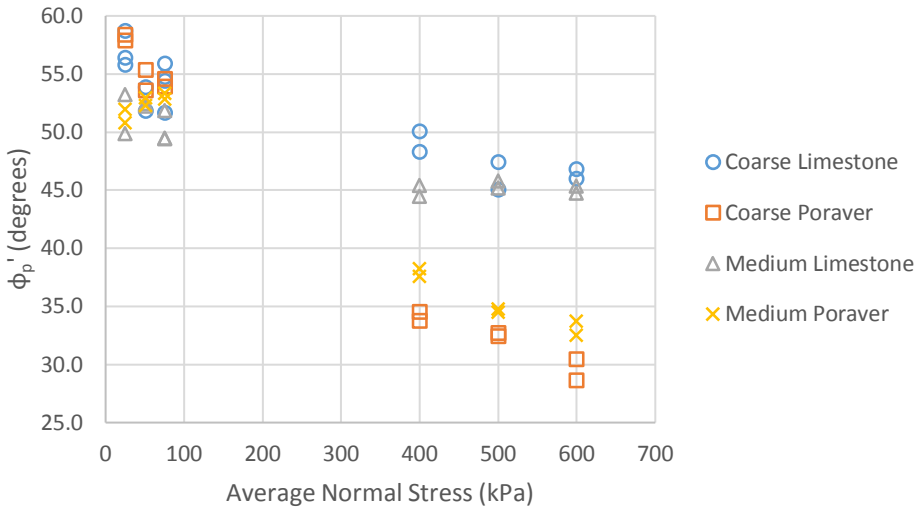

Figure 4.25 - Peak friction angles from LSDS tests.

For SSDS tests, it was observed that that Coarse Kling shows an average reduction in φ_p' of 8.1°, Coarse Limestone shows a reduction of 13.4°, and Coarse Poraver shows a reduction of 17.5° when the normal stresses were increased from 25-75 kPa to 400-600 kPa. This reduction seems to reflect the increasing crushability of the materials when dilation is suppressed. Medium fractions of Kling, Limestone and Poraver show average reductions in the peak friction angle of 5.2°, 9.5° and 9.5°, respectively – having much lower reduction in φ_p' than the coarser materials. Therefore, it seems that particle size has much larger effect on the peak friction angle than particle shape when dilation is suppressed. It is difficult to quantify the effects of particle shape on shear strength when dilation is suppressed due to the different crushability of the materials in this study, coupled with the fact that the variation caused by changing particle shape is likely to be very small.

4.4.1 Scale Effects

At high normal stresses, φ_p' from LSDS tests were, on average, 3° higher for Coarse Limestone and 3.7° higher for Medium Limestone than those determined from SSDS tests. These results are similar to those reported by Ni et al. (2000). However, the opposite trend was observed for Poraver. Values of φ_p' from LSDS tests for Coarse Poraver were 2.2° lower, and 3.2° lower for Medium Poraver when compared

to SSDS tests. This is likely due to the additional suppression of dilation and particle breakage observed in the LSDS tests.

For low normal stresses, φ'_p from LSDS tests for Coarse Limestone were 3.8° higher on average than those from SSDS tests, and were approximately the same for Medium Limestone. Values of φ'_p were roughly the same for Coarse Poraver at low normal stresses, and 4.5° higher on average for LSDS tests on Medium Poraver compared to SSDS tests. There is no obvious trend here. However, one trend is that the overall reduction of φ'_p as normal stresses increase from 25 to 75 kPa is less for LSDS tests than for SSDS.

4.5 Critical State Shear Strength (φ'_{cs})

Critical state friction angles (φ'_{cs}) were determined for all SSDS direct shear tests where the value of shear strength at critical state could be established, using eqn. 2.1. A plot of φ'_{cs} versus average normal stress for SSDS tests is presented below in Figure 4.26. For coarse granular materials, values of φ'_{cs} decreased by 7-9.5° as normal stress is increased from the 25-75 kPa range to the 400-600 kPa range. For the medium fractions, this effect is much less pronounced or non-existent, where φ'_{cs} is similar between the high and low stress ranges. It seems that particle size is the main cause of this since the crushability and suppression of dilation for each soil varied considerably.

For both Coarse and Medium Poraver, φ'_{cs} decreases as normal stress is increased from 400 to 600 kPa, where dilation is fully suppressed. This is similar to what was observed for φ'_p. Similar findings were also reported by Kikumoto et al. (2010) and Hamidi et al. (2009), who attribute this behaviour to excessive changes in gradation due to crushing. Within the 400-600 kPa normal stress range, Limestone and Kling sands show that values of φ'_{cs} stay the same, or slightly increase as normal stress increases. These findings were similar to Sadarakimi and Olsen (2011), who stated that the increase is due to the broadening of the GSD, but also to increased angularity from particle rupture. It seems that given the unique particle structure and crushing behaviour of Poraver, the crushed particles would not necessarily

be more angular, which could partially explain the different trend at critical state compared to Limestone and Kling. It could also be that the magnitude of the reduction of φ'_{cs} is directly correlated with the increase in fines content due to crushing (Ghafghazi et al., 2014), since particle breakage for Poraver resulted in the production of more fine particles (<75 microns) than for Limestone or Kling sand.

In almost all loading cases, the coarse fractions for each soil type resulted in a value of φ'_{cs} greater than their medium fractions, which is in agreement with Dai et al. (2016). The only exception is Poraver in the 400-600 kPa normal stress range, where φ'_{cs} for the two fractions are comparable and likely influenced by the extent of particle breakage.

For the natural soils, including Poraver at low stresses, φ'_{cs} increases with increasing particle angularity. Limestone shows the highest values of φ'_{cs}, followed by Kling sand, with Poraver having the lowest φ'_{cs} of the three – again, with the exception of Poraver at high stresses due to excessive crushing. These results are in line with the prevailing evidence in the literature (Koerner, 1970; Chan & Page, 1997; Ni et al., 2000; Sukumaran & Ashmawy, 2001). As the normal stresses increase to 400-600 kPa, the difference in φ'_{cs} for soils due to particle shape is much smaller than what was observed at low stresses. Therefore, particle shape seems to have less influence on φ'_{cs} as normal stresses increase and dilation is suppressed.

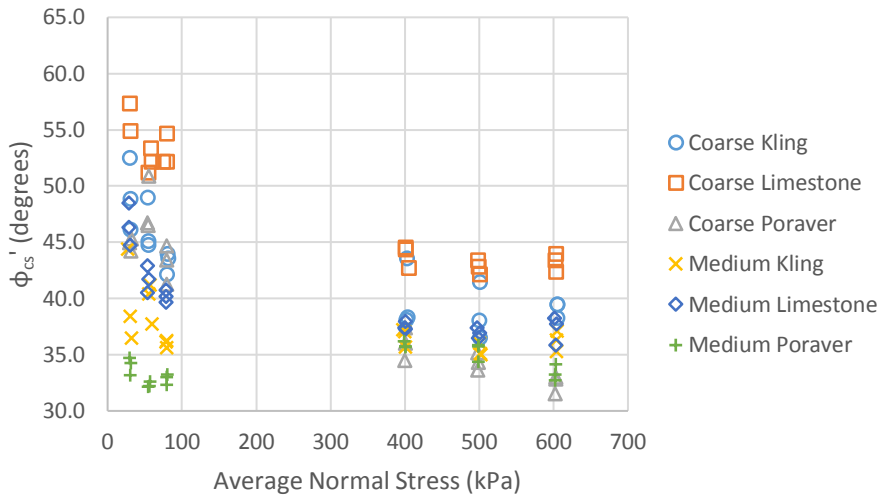

Figure 4.26 – Critical State Friction Angles from SSDS tests.

4.5.1 Cyclic Direct Shear Tests

Cyclic direct shear tests were performed using the SSDS apparatus to evaluate the effect of additional strain on the shear strength at critical state. Due to time constraints, only a limited number of tests were performed, which focused on materials where critical states from conventional tests were the least consistent. Results for cyclic tests performed at 600 kPa and 75 kPa normal load are shown below in Figure 4.27, while the remaining results can be found in Appendix D. The number of cycles for each test ranged between 5 and 8. Dilation data for all tests showed continued contractive behaviour after 8 cycles with no indication that contraction was nearing completion. Many more cycles would be required before volume change and particle breakage would cease. Most tests showed a notable reduction in critical state shear strength and seemed to converge at a consistent value for several of the final cycles, with the exception of Coarse Poraver at 75 kPa normal stress (Figure 4.27c), where the critical state consistently converged near the first cycle. Conversely, Coarse Limestone at 75 kPa normal stress showed significant reduction in critical state strength. This trend was consistent for 25 kPa and 50 kPa tests, which can be see from the plot of φ'_{cs} versus average normal stress for Coarse Limestone in Figure 4.28. Values of φ'_{cs} for Coarse Limestone reduced approximately 8° on average after a minimum of 5 cycles. This brought φ'_{cs}

at low stresses to values comparable to that of high stresses. This is likely because the relatively large, flat and angular particles of limestone require more strain to rearrange themselves efficiently. Also, limestone particles have likely become more rounded after breakage of surface asperities during shearing. For the high normal stress range, the additional cycles caused a marginal reduction in critical state friction angle. Scale effects could not be investigated here since the LSDS apparatus is not designed to perform cyclic tests.

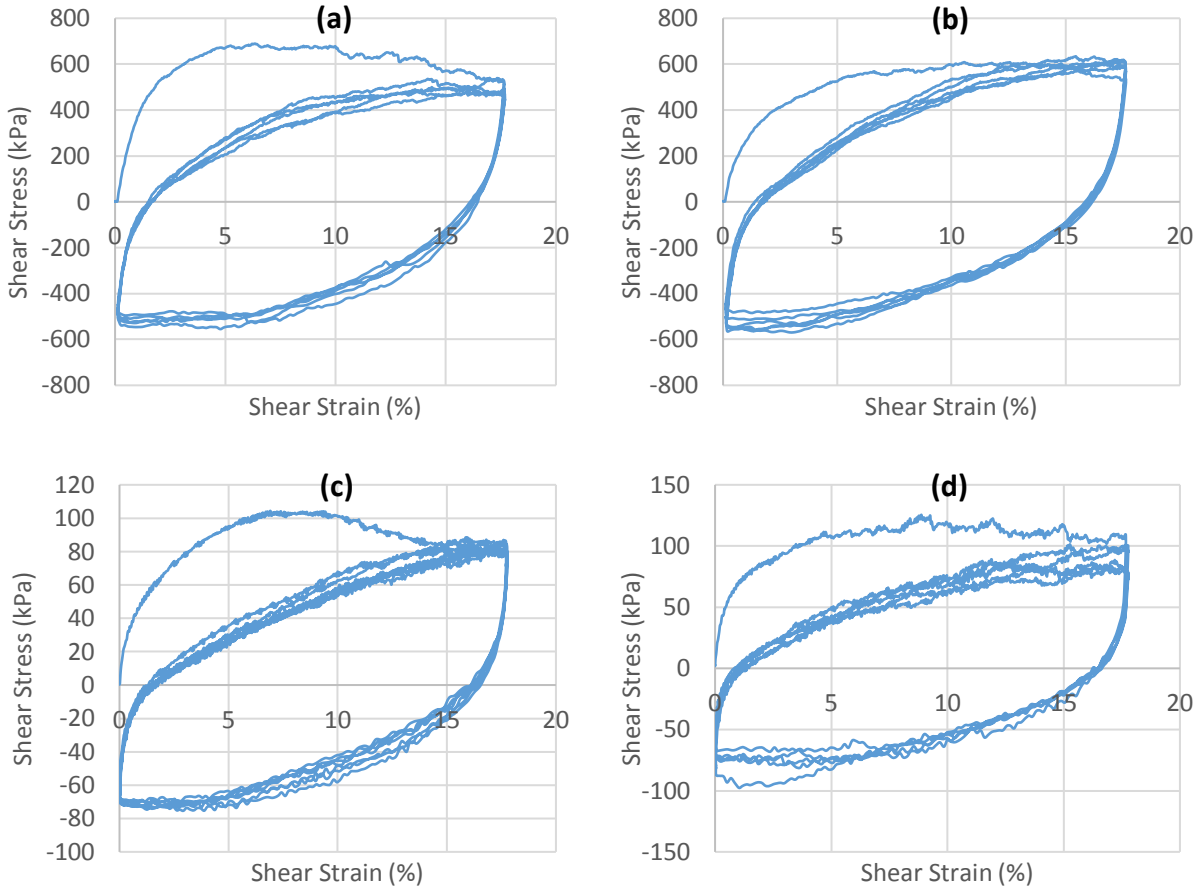

Figure 4.27 - Cyclic SSDS test results for a) Coarse Kling at 600 kPa, b) Coarse Limestone at 600 kPa, c) Coarse Poraver at 75 kPa, d) Coarse Limestone at 75 kPa.

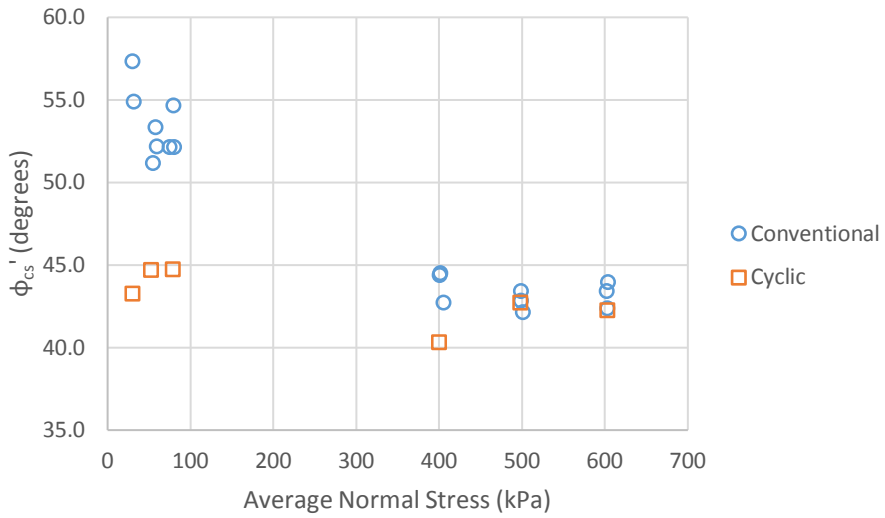

Figure 4.28 – Comparison of critical state friction angles determined from conventional SSDS with cyclic SSDS tests for Coarse Limestone.

4.5.2 Scale Effects

It was difficult to obtain good quality data on φ'_{cs} for LSDS tests for a few reasons. Firstly, there were less replicates performed due to the time consuming nature of the testing and soil preparation process, which reduced confidence in the data. Second, the total shear strain was often not large enough for the soil to have reached critical state. Finally, normal stresses for the LSDS high stress tests were corrected incrementally throughout the test creating a 'stepped' appearance of the stress-strain curves. Therefore, friction angles were assessed at 12% shear strain for both SSDS and LSDS tests to evaluate scale effects. This was the minimum shear strain achieved for some tests, and was chosen in order to accommodate all test results. Shear stresses at 12% shear strain for all tests occurred post-peak, and were generally on the downward trend towards critical state.

A plot showing the friction angle at 12% strain ($\varphi'_{12\%}$) versus average normal stress is shown below in Figure 4.29. When dilation is suppressed at high stresses, $\varphi'_{12\%}$ for Limestone was higher for LSDS tests than for SSDS tests and vise-versa for Poraver. This is the same trend as was observed for the peak friction angles (see section 4.4.1). In addition, $\varphi'_{12\%}$ for Poraver reduced continually as normal stress

increased, while Limestone tended to stabilize. This effect was also observed with $\varphi'_{12\%}$, and was deemed to be caused by difference in crushability and particle structure of the two materials. Generally, a significant reduction in $\varphi'_{12\%}$ was observed as the normal stress was increased from 25-75 kPa to 400-600 kPa range for the coarse fractions, while the medium fractions show a marginal increase or decrease in $\varphi'_{12\%}$.

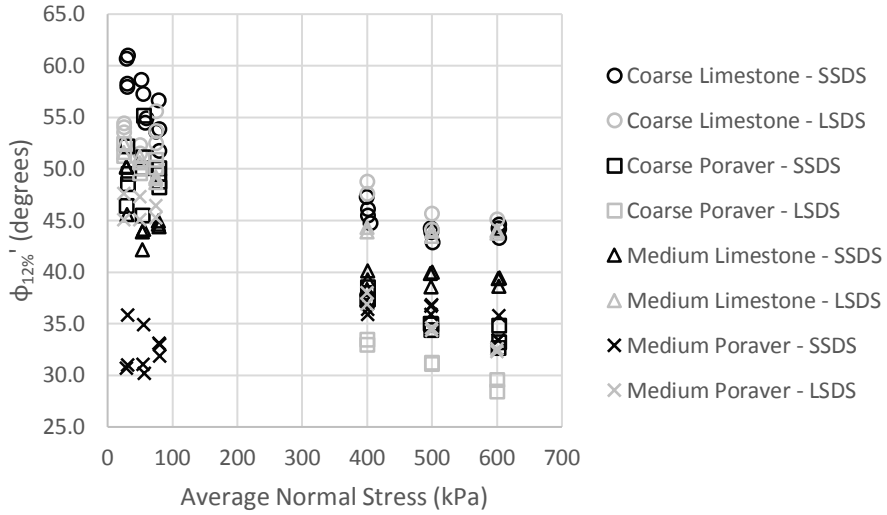

Figure 4.29 - Friction angle at 12% shear strain versus average normal stress for SSDS and LSDS tests.

4.6 Rotation of Top Cap

The rotation of the top cap was restricted on the SSDS apparatus in an attempt to limit errors in measuring dilation and to help reduce non-uniformities present in the sample. To achieve this, a top cap was manufactured to create a more snug fit inside the upper shear box, and was equipped with a set-screw to tighten against the button load cell to restrict rotational movement. Performance was evaluated by performing several SSDS tests with the original free-to-move top cap while measuring vertical displacement at the upstream and downstream ends, and comparing with similar tests using the new top cap. The results of SSDS tests performed on Coarse Limestone showing dilation and top cap rotation data are presented in Figure 4.30. Top cap rotation data for all tests can be found in Appendix E.

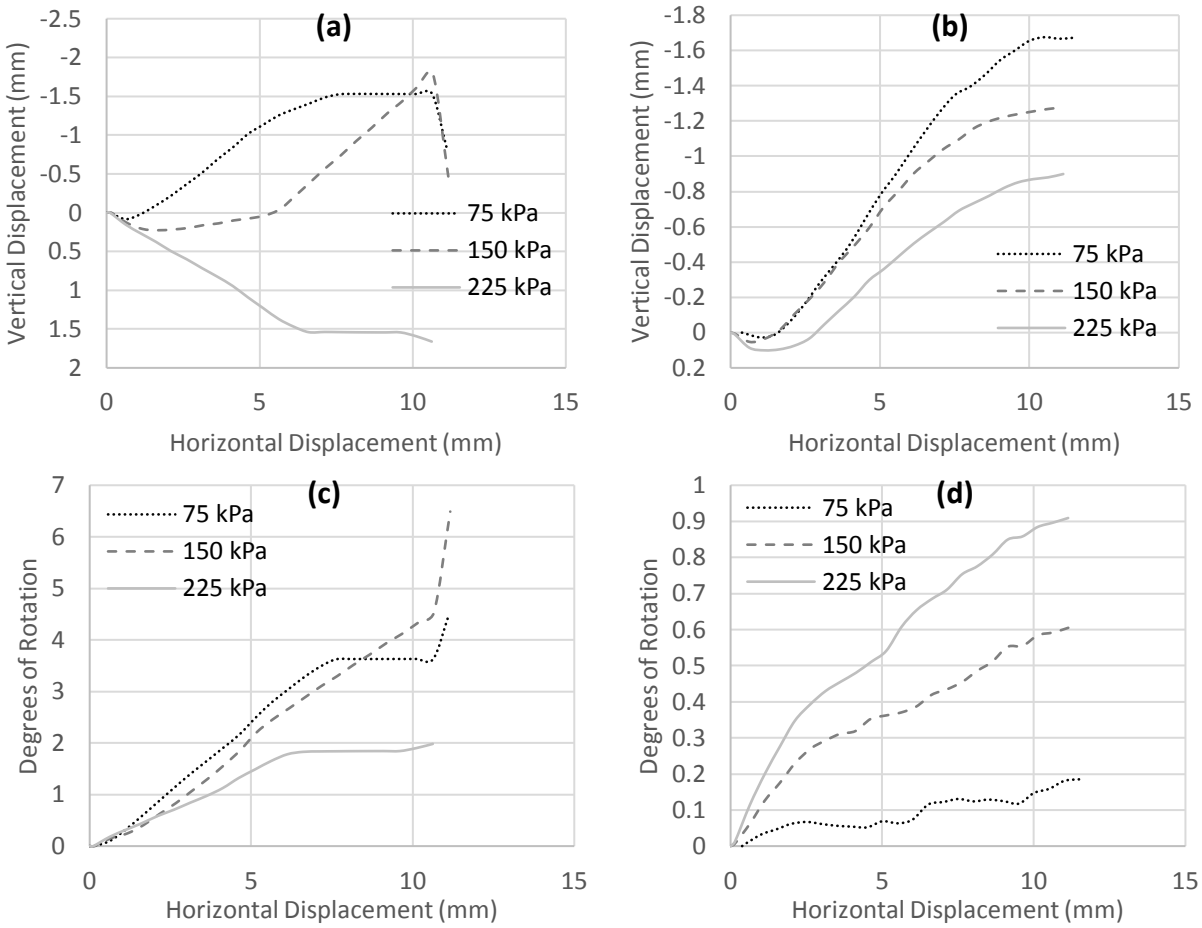

Figure 4.30 – Dilation and top cap rotation data for Coarse Limestone with a,c) original free-to-rotate top cap and, b,d) new top cap with restricted rotation.

It was observed that the new top cap significantly decreased the amount of rotation from in the range of 2-6°, to less than 1°. When using the free-to-rotate top cap (Fig. 4.30c) the amount of rotation reduced as the normal stress increased. While this effect is not captured in Figure. 4.30d, this was generally true for most tests performed in this thesis. Therefore, the new top cap had the largest impact on tests performed in the low stress range. One noticeable effect is that the dilation measurements were much more consistent when the rotation of the top cap was restricted, particularly as the normal stress becomes larger than 200 kPa (Figure 4.30b). Given the focus on suppression of dilation in this thesis, the modification of restricting rotation of the top cap was successful and has allowed for much improved data collection on dilation response during SSDS tests.

Chapter 5 – Conclusions and Recommendations

5.1 Summary

The direct shear test is a common and simple method for determining the shear strength of granular materials. However, despite its widespread use researchers are skeptical of the reliability of the direct shear test due to non-uniformities in the sample and the common overestimation of peak shear strength. The literature review has identified several gaps in the knowledge related to the mechanical behaviour of granular materials in direct shear, particularly related to the determination of the peak and critical state friction angle when dilation is restricted and particle breakage occurs. Therefore, the following hypotheses were examined through a laboratory investigation:

1. Suppression of dilation during shear does not only affect the magnitude of peak shear strength, but can also affect the magnitude of critical state (large strain) shear strength of granular materials.
2. Suppression of dilation is more critical for rounded sands than it is for angular sands.
3. Size of the shear box (vis-à-vis particle size of the sand) is more critical for tests in which the normal loading suppresses the sand's tendency to dilate.

The laboratory investigation involved a series of direct shear tests conducted on three different crushable materials – Kling sand, Limestone sand, and Poraver expanded glass beads – in order to investigate the effects of suppression of dilation on shear strength. Each material type had different particle shapes and was divided into Coarse and Medium fractions so that effects of particle shape and particle size could be studied. Tests were performed on both small-scale (SSDS) and large-scale (LSDS) direct shear boxes so that effects of scale could also be investigated. Modifications have been made to

the SSDS apparatus, namely the top cap was redesigned so that the samples tendency to rotate could be reduced and therefore dilation measurements could be improved.

5.2 Conclusions

Based on the laboratory testing results, the following conclusions were drawn:

- The stress-strain and dilatancy behaviour of the materials tested can be accurately described using Coulomb's Friction Model. Suppression of dilation increases as normal load increases, while the materials peak behaviour becomes reduced as it transitions from Type B (strain softening) to Type A (strain hardening) behaviour. This type of behaviour was observed for all materials tested; however, each material has its own 'threshold' value of normal stress corresponding to 'Pt. C' on Coulomb's curved failure envelope, which is related to the soils crushability. Soils that are more crushable will require less normal stress to reach 'Pt. C', i.e. transition from Type B to Type A behaviour.
- Larger particle sizes tend to result in more dilative response than smaller particle sizes. Alternatively, smaller particle sizes tend to result in more contractive behaviour than larger particles. It was also observed that (relatively) constant volume is reached sooner (i.e. at smaller shear strains) for smaller particle sizes when compared to larger particle sizes. This is due to the smaller particle circumference to be overcome by rolling and climbing, which requires less energy and less volume than for larger particles.
- Sample size has a significant effect on suppression of dilation. All materials showed more contractive behaviour when performing LSDS tests when compared to SSDS tests. This is likely due to the following reasons: reduction in boundary effects, an increase in the overall volume of voids in the larger shear box, and that total shear displacements were 3 to 5 times larger in LSDS tests than SSDS tests.

- It was observed that the normalized stress-strain curves shifted downwards as normal stress increased for all materials. However, the magnitude of this shift was greatest for Poraver, having the highest crushability, and the least for Kling sand, having the lowest crushability. It can be concluded that the magnitude of the downward shift is reflective of the changing gradation of the soil caused by particle breakage.
- The particle crushing behaviour of Poraver does not seem to follow the behaviour described in the literature due to its manufactured porous internal structure, making it difficult to adequately compare with the natural soils in this study.
- Generally, φ_p' is highest at low normal stresses and decreases as normal stress is increased, following the behaviour described by Coulomb's Friction Model. Values of φ_p' for natural soils begin to stabilize as the critical state is reached; however, values of φ_p' for Poraver continue to decrease despite having apparently reached critical state. This is due to the large extent of crushing observed in Poraver in the high stress range and resulting change in gradation.
- Natural soils showed an increase in φ_p' as particle size increased for both high and low stresses, in agreement with the literature. Poraver showed a decrease in φ_p' with particle size at high stresses, while at low stresses behaved like the natural soils. This behaviour is due to the large presence of internal flaws and high crushability of Poraver.
- The effects of suppression of dilation (i.e. increasing normal stresses) on φ_p' due to particle shape are minimal, and difficult to quantify due to the different crushability of the materials in this study. Particle size likely has a much greater effect on φ_p' than particle shape when dilation is suppressed.
- At high normal stresses, φ_p' was 3-4^o higher for Limestone, and 2-3^o lower for Poraver in LSDS tests when compared to SSDS tests.

- For coarse fractions of all soils, φ'_{cs} was found to decrease between 7-9.5^{o} as dilation was suppressed at high normal stresses. This effect was much less pronounced or non-existent for medium fractions, indicating that φ'_{cs} decreases with increasing particle size.
- For natural soils, including Poraver at low stresses, φ'_{cs} increases with increasing particle angularity, which is in line with evidence from the literature. The only exception is for Poraver at high stresses due to excessive crushing. As the normal stresses increase to 400-600 kPa, the difference in φ'_{cs} for soils due to particle shape is much smaller than what was observed at low stresses. Therefore, particle shape seems to have less influence on φ'_{cs} as normal stresses increase and dilation is suppressed.
- When dilation is suppressed at high stresses, $\varphi'_{12\%}$ for Limestone was higher for LSDS tests than for SSDS tests and vise-versa for Poraver. In addition, $\varphi'_{12\%}$ for Poraver reduced continually as normal stress increased, while Limestone tended to stabilize. This effect was also observed with φ'_{p}, and was deemed to be caused by difference in crushability and particle structure of the two materials.
- It was observed that the new top cap significantly decreased the amount of rotation from in the range of 2-6^{o}, to less than 1^{o}. Also, when using the free-to-rotate top cap, the amount of rotation reduced as suppression of dilation increased. Therefore, the new top cap had the largest impact on tests performed in the low stress range. Modifications made to the top cap to limit rotation were successful and provided improved measurement of dilation response.

This study was successful in addressing hypothesis no. 1, as it was determined that suppression of dilation during shear affects the magnitude of both φ'_{p} and φ'_{cs}. Some conclusions were drawn related to hypotheses no. 2 and 3 (i.e. particle size and scale effects as they relate to suppression of dilation); however, further testing is required to better understand these relations.

5.3 Recommendations

To better address hypothesis no. 2 – suppression of dilation is more critical for rounded sands than it is for angular sands – further testing should be completed on materials which have different particle shape, but comparable crushing strength. The large difference in crushing behaviour between Limestone and Poraver beads made it difficult to isolate effects of particle size from the results. Part of the difficulty for selecting testing materials in this thesis was due to the restrictions on maximum normal stress imposed by the testing equipment. Perhaps existing equipment could be modified or new equipment acquired, to allow for higher applied normal stresses, which could induce adequate suppression of dilation on a broader range of materials. Scale effects could have been more thoroughly investigated with more time, since LSDS tests required significantly more time to prepare and run tests. Modifications could be made to the high stress set-up on the LSDS apparatus to increase consistency of the applied load.

Further investigation could be conducted into how normal load changes as shearing takes place while dilation is suppressed, and whether or not these changes might contribute to the errors observed in conventional direct shear tests. This might involve using existing pneumatic pressure system, or modifying and using a hydraulic system to get a more immediate pressure response. LSDS apparatus would need to be modified so that normal load data could be collected along with data it currently collects on shear strength and horizontal and vertical displacement.

Analysis on φ'_{cs} could be improved by running more cyclic direct shear tests on all materials for all trials, rather than select trials only. Time constraints prevented this to some degree, but also equipment capabilities. The LSDS apparatus is not designed to run cyclic tests, which limits the quality of data that can be produced to study scale effects on φ'_{cs}. Also, sieve analyses should be run after cyclic tests as well as 'static' tests to investigate how much additional particle breakage occurs as the soils continue to shear at larger strains.

Further 1D compression testing on all materials, but in particular, Limestone and Kling would be worthwhile to see how the proportion of particle breakage due to shearing versus 1D compression changes as B_r increases. This could provide more insight on how the crushing behaviour of Poraver compares to mineral soils, in this case Limestone and Kling sand. Finally, while running 1D compression tests, the relationship between particle crushing and creep could be investigated.

Bibliography

Arslan, H., Baykal, G. & Sture, S., 2009. Analysis of the influence of crushing on the behaviour of granular materials under shear. *Granular Matter,* 11(2), pp. 87-97.

Barden, L., Ismail, H. & Tong, P., 1969. Plane Strain Deformation of Granular Material at Low and High Pressures. *Geotechnique,* 19(4), pp. 441-452.

Bareither, C., Benson, C. & Edil, T., 2008. Comparison of shear strength of sand backfills meaured in small-scale and large-scale direct shear tests. *Canadian Geotechnical Journal,* 45(9), pp. 1224-1236.

Budhu, M., 2011. *Soil Mechanics and Foundations.* 3rd ed. New York: John Wiley and Sons.

Casagrande, A., 1936. Characteristics of cohensionless soils affecting the stability of slopes and earth fills. *Journal of Boston Society of Civil Engineers,* 23(1), pp. 13-32.

Cerato, A. & Lutenegger, A., 2006. Specimen Size and Scale Effects of Direct Shear Box Tests of Sands. *Geotechnical Testing Journal,* 29(6), pp. 507-516.

Chan, L. & Page, N., 1997. Particle fractal and load effects on internal friction in powders. *Powder Technology,* Volume 90, pp. 259-266.

Cho, G., Dodds, J. & Santamarina, J., 2006. Particle Shape Effects on Packing Density, Stiffness, and Strength: Natural and Crushed Sands. *Journal of Geotechnical and Geoenvironmental Engineering,* 132(5), pp. 591-602.

Coduto, D., 2001. *Foundation Analysis and Design.* Upper Saddle River, NJ: Pretence Hall.

Dai, B., Yang, J. & Zhou, C., 2016. Observed Effects of Interparticle Friction and Particle Size on Shear Behaviour of Granular Materials. *International Journal of Geomechanics,* 16(1), p. 04015011.

Dai, B., Yang, J. & Zhou, C., 2016. Observed Effects of Interparticle Friction and Particle Size on Shear Behaviour of Granular Materials. *International Journal of Geomechanics,* 16(1), p. 04015011.

Daouadji, A., Hicher, P. Y. & Rahma, A., 2001. An elastoplastic model for granular materials taking into account grain breakage. *European Journal of Mechanics,* Volume 20, pp. 113-137.

Dounias, G. & Potts, D., 1993. Numerical Analysis of Drained Direct and Simple Shear Tests. *Journal of Geotechnical Engineering,* 119(12), pp. 1870-1891.

Dyer, M., 1985. *Observation of stress distribution in crushed glass with application to soil reinforcement,* Oxford: University of Oxford.

Ezaoui, A., Lecompte, T., Di Benedetto, H. & Garcia, E., 2011. Effects of various loading stress paths on the stress-strain properties and on crushability of an industrial soft granular material. *Granular Matter,* 13(4), pp. 283-301.

Ghafghazi, M., Shuttle, D. A. & DeJong, J. T., 2014. Particle breakage and the critical state of sand. *Soils and Foundations,* 54(3), pp. 451-461.

Guo, P. & Su, X., 2007. Shear strength, interparticle locking, and dilatancy of granular materials. *Canadian Geotechnical Journal,* Volume 44, pp. 579-591.

Guo, P. & Su, X., 2007. Shear strength, interparticle locking, and dilatancy of granular materials. *Canadian Geotechnical Journal,* 44(5), pp. 579-591.

Hamidi, A., Azini, E. & Masoudi, B., 2009. Impact of gradation on the shear strength-dilation behaviour of well graded sand-gravel mixtures. *Scientia Iranica,* 19(3), pp. 393-402.

Hamidi, A., Azini, E. & Masoudi, B., 2012. Impact of gradation on the shear strength-dilation behaviour of well graded sand-gravel mixtures. *Scientia Iranica,* 19(3), pp. 393-402.

Hardin, B., 1985. Crushing of Soil Particles. *Journal of Geotechnical Engineering,* 111(10), pp. 1177-1192.

Harehdasht, S. A. et al., 2018. Influence of particle size and gradation on shear strength-dilation relation of granular materials. *Canadian Geotechnical Journal,* 00(00), pp. 1-20.

Hattamleh, O. A., Al Shalabi, F., Al Qablan, H. & Al-Rousan, T., 2010. Effect of grain crushing and bedding plane inclination on Aquaba sand behaviour. *Bulletin of Engineering Geology and the Environment,* Volume 69, pp. 41-49.

Igwe, O., Fukuoka, H. & Sassa, K., 2012. The Effect of Relative Density and Confining Stress on Shear Properties of Sands with Varying Grading. *Geotechnical and Geological Enginering,* Issue 30, pp. 1207-1229.

Jaeger, J., 1969. Failure of rocks under tensile conditions. *International Journal of Rock Mechanics and Mining Science,* Volume 4, pp. 219-227.

Jardine, R. K. R. Z. L. a. T. C., 1999. *Some fundamental aspects of the pre-failure behaviour of granular soils.* Torino, Italy, In Proceedings of the 2nd International Symposium on Pre-failure Deformation Characteristics of Geomaterials.

Jewell, R., 1989. Direct shear tests on sand. *Geotechnique,* 39(2), pp. 309-322.

Karimpour, H. & Lade, P., 2010. Time effects relate to crushing in sand. *Geotechnical and Geoenvironmental Engineering,* 9(136), pp. 1209-1219.

Kikumoto, M., Wood, D. M. & Russell, A., 2010. Particle Crushing and Deformation Behaviour. *Soils and Foundations,* 50(4), pp. 547-563.

Kirkpatrick, W., 1965. Effects of grain size and graditing on the shearing behaviour of granular materials. *Proceedings of the 6th International Conference on Soil Mechanics and Foundation Engineering,* Volume 1, pp. 273-277.

Koerner, R., 1970. Effect of particle characteristics on soil strength.. *Journal of the Soil Mechanics and Foundation Engineering Division, ASCE,* 96(SM4), pp. 1221-1234.

Konrad, J. & Salami, Y., 2017. Particle breakage in granular materials - a conceptual framework. *Canadian Geotechnical Journal,* pp. 1-10.

Krumbein, W. & Sloss, L., 1963. *Stratigraphy and sedimentation.* 2nd ed. San Francisco: Freeman.

Lade, P. & Yamamuro, J., 1996. Undrained Sand Behaviour in Axisymmetric Tests at High Pressures. *Journal of Geotechnical Engineering,* 122(2), pp. 120-129.

Lade, P., Yamamuro, J. & Bopp, P., 1996. Significance of Particle Crushing in Granular Materials. *Journal of Geotechnical Engineering,* 122(4), pp. 309-316.

Lambe, T. & Whitman, R., 1969. *Soil Mechanics.* New York: John Wiley and Sons.

Lee, D., 1992. *The angles of friction of granular fills,* Cambridge, UK: University of Cambridge.

Lee, K. & Farhoomand, I., 1967. Compressibility and Crushing of Granular Soil in Anisotropic Triaxial Compression. *Canadian Geotechnical Journal,* 4(1), pp. 68-86.

Leslie, D., 1969. Relationship between shear strength, gradation and index properties. *Proceedings of the 7th International Conference on Soil Mechanics and Foundation Engineering,* pp. 212-222.

Lings, M. & Dietz, M., 2004. An improved direct shear apparatus for sand. *Geotechnique,* 54(4), pp. 245-256.

Li, Y. & Aydin, A., 2010. Behaviour of rounded granular materials in direct shear: Mechanisms and quantification of fluctuations. *Engineering Geology,* 115(1-2), pp. 96-104.

Mandelbrot, B., 1982. *The fractal geometry of nature.* New York: Freeman.

Marachi, N., Chan, C. & Seed, H., 1972. Evaluation of properties of rockfill materials. *Journal of Soil Mechanics,* 98(SM1), pp. 95-112.

Marsal, R., 1967. Large-Scale Testing of Rockfill Materials. *Journal of the Soil Mechanics and Foundations Division,* 93(2), pp. 27-43.

McDowell, G. & Bolton, M., 1998. On the micromechanics of crushable aggregates. *Geotechnique,* 48(5), pp. 667-679.

McDowell, G., Bolton, M. & Robertson, D., 1996. The fractal crushing of granular materials. *Journal of the Mechanics of Physics of Solids,* 44(12), pp. 2079-2101.

Mitchel, J. & Soga, K., 2005. *Fundamentals of Soil Behaviour.* 3rd ed. Hoboken, NJ: John Wiley and Sons.

Muir Wood, D. & Maeda, K., 2008. Changing grading of soil: effect on critical states. *Acta Geotechnica,* Volume 3, pp. 3-14.

Negussey, D., Wijewickreme, W. & Vaid, Y., 1988. Constant-volume friction angle of granular materials. *Canadian Geotechnical Journal,* 25(1), pp. 50-55.

Ni, Q., Powrie, W., Zhang, X. & Harkness, R., 2000. *Effect of Particle Properties on Soil Behaviour: 3-D Numerical Modeling of Shearbox Tests.* Denver, Colorado, ASCE, pp. 58-70.

Nobari, E. & Duncan, J., 1973. *Effect of reservoir filling on stresses and movements in earth and rockfilil dams,* Berkeley, California: Office of Reservoir Services, University of California.

Palmer, A. & Sanderson, T., 1991. Fractal crushing of ice and brittle solids. *Proceedings of the Royal Society of London A,* Volume 433, pp. 469-477.

Potts, D., Dounias, G. & Vaughan, P., 1987. Finite element analysis of the direct shear box test. *Geotechnique,* 37(1), pp. 11-23.

Powers, M., 1953. A new roundness scale for the sedimentary particles. *Journal of Sedimentary Petrology,* Volume 23, pp. 117-119.

Qiu, J., Tatsuoka, F. & Uchimura, T., 2000. Constant Pressure and Constant Volume Direct Shear Tests on Reinforced Sand. *Soils and Foundations,* 40(4), pp. 1-17.

Reynolds, O., 1885. On the Dilatancy of Media Composed of Rigid Particles in Contact. With Experimental Illustrations. *Philosophical Magazine and Journal of Science,* 20(127), pp. 469-481.

Roscoe, K., Schofield, A. & Wroth, C., 1958. On The Yielding of Soils. *Geotechnique,* 8(1), pp. 22-53.

Rowe, P. W., 1962. The stress-dilatancy relation for static equilibrium of an assembly of particles in contact. *Proceedings of the Royal Society A,* pp. 500-527.

Sadrekarimi, A. & Olson, S. M., 2011. Critical state friction angle of sands. *Geotechnique,* 61(9), pp. 771-783.

Sharma, J., 2010. *CE328 Lecture Note #11 - Shear Strength of Soils Part 1: The Friction Model.* Saskatoon, SK: University of Sasketchewan.

Shibuya, S., Mitachi, T. & Tamate, S., 1997. Interpretation of direct shear bo testing of sands as quasi-simple shear. *Geotechnique,* 47(4), pp. 769-790.

Simoni, A. & Houlsby, G., 2006. The Direct Shear Strength and Dilatancy of Sand-gravel Mixtures. *Geotechnical and Geological Engineering,* 24(3), pp. 523-549.

Skempton, A., 1958. Arthur Langtry Bell (1874-1956) and His Contribution to Soil Mechanics. *Geotechnique,* 8(4), pp. 143-157.

Sowers, G., Williams, R. & Wallace, T., 1965. Compressibility of broken rock and the settlement of rockfills. *Proceedings from the 6th Conference on Soil Mechanics and Foundation Engineering (Montreal),* Volume II, pp. 561-565.

Steacy, S. & Sammis, C., 1991. An automation for fractal patterns of fragmentation. *Nature,* 353(6341), pp. 250-252.

Sukumaran, B. & Ashmawy, A., 2001. Quantitative characterization of the geometry of discrete particles. *Geotechnique,* 51(7), pp. 19-27.

Taylor, D., 1948. *Fundamentals of soil mechanics.* New York: John Wiley and Sons.

Turcotte, D., 1986. Fractals and fragmentation. *Journal of Geophysical Research,* 91(B2), pp. 1921-1926.

Turcotte, D., 1997. *Fractals and chaos in geology and geophysics.* Cambridge, UK: Cambridge University Press.

Tyler, S. & Wheatcraft, S., 1992. Fractal scaling of soil particle-size distributions: analysis and limitations. *Soil Science Society of America Journal,* 56(2), pp. 362-369.

Vallejo, L., Lobo-Guerrero, S. & Chik, Z., 2005. A Network of Fractal Force Chains and Their Effect in Granular Materials Under Compression. *Proceedings from Fractals in Engineering,* pp. 67-80.

Wang, J., Cheng, Y., Zhang, H. & Deng, D., 2015. Effects of particle size on compaction behaviour and particle crushing of crushed sandstone-mudstone particle mixture. *Environmental Earth Sciences,* 73(12), pp. 8053-8059.

Weibull, W., 1951. A statistical distribution function of wide applicability. *Journal of Applied Mechanics,* Volume 18, pp. 293-297.

Yamamuro, J. & Lade, P., 1996. Drained Sand Behaviour in Axisymmetric Tests at High Pressures. *Journal of Geotechnical Engineering,* 122(2), pp. 109-119.

Zhang, L. & Thornton, C., 2007. A numerical examination of the direct shear test. *Geotechnique,* 57(4), pp. 343-354.

Appendix A – Sieve Analyses at Low Stresses

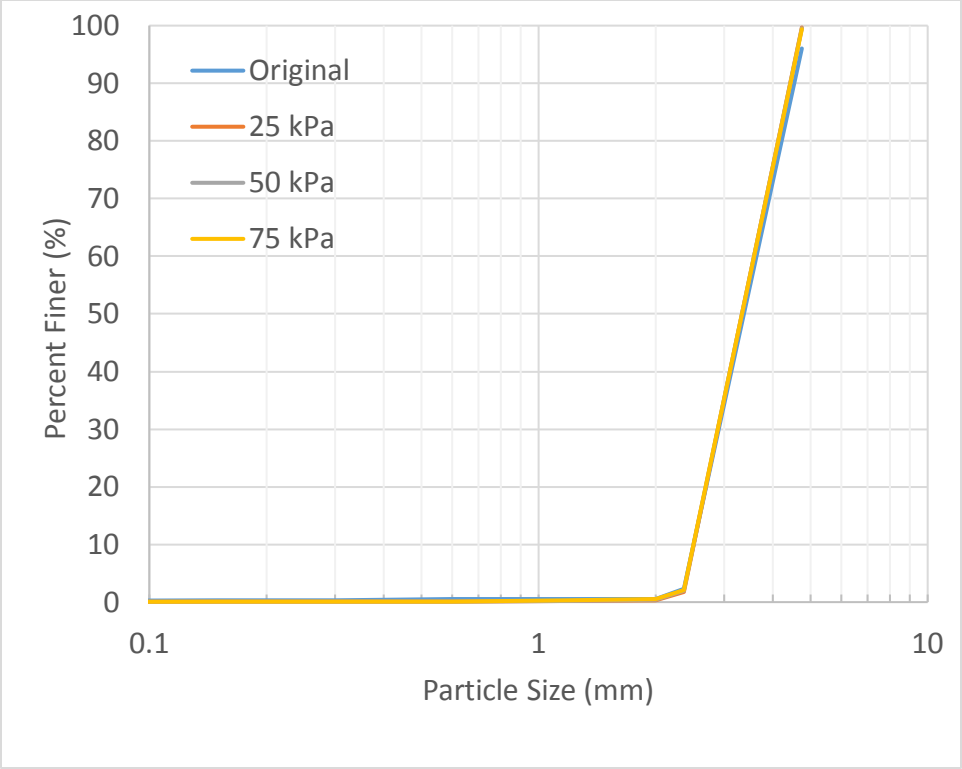

Sieve Analyses for Coarse Kling – SSDS

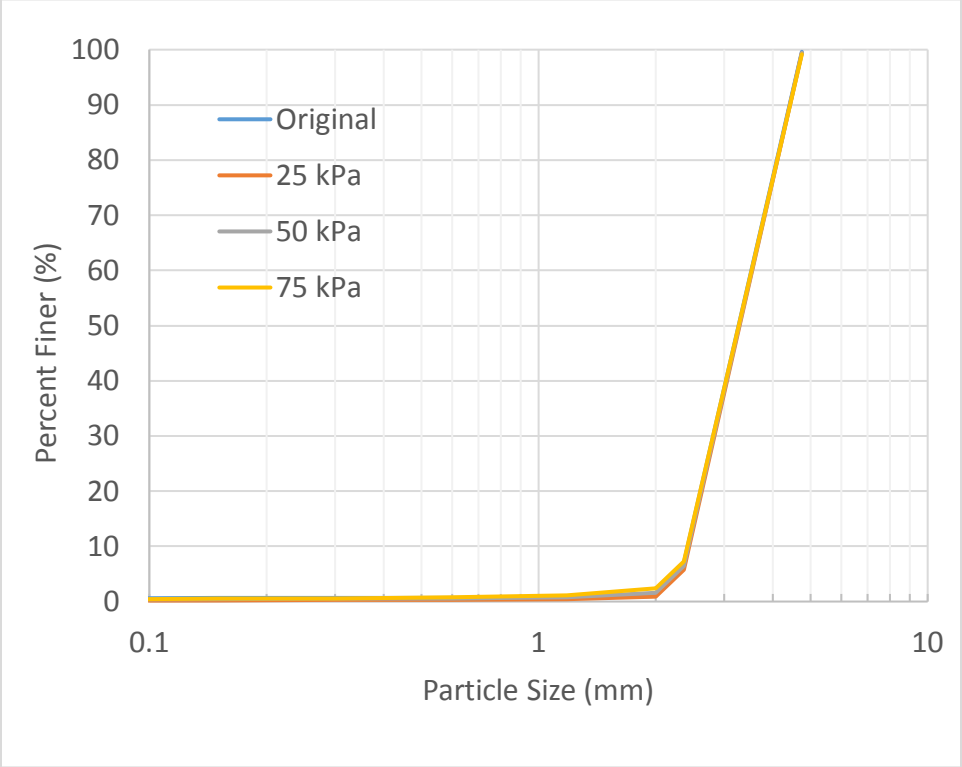

Sieve Analyses for Coarse Limestone – SSDS

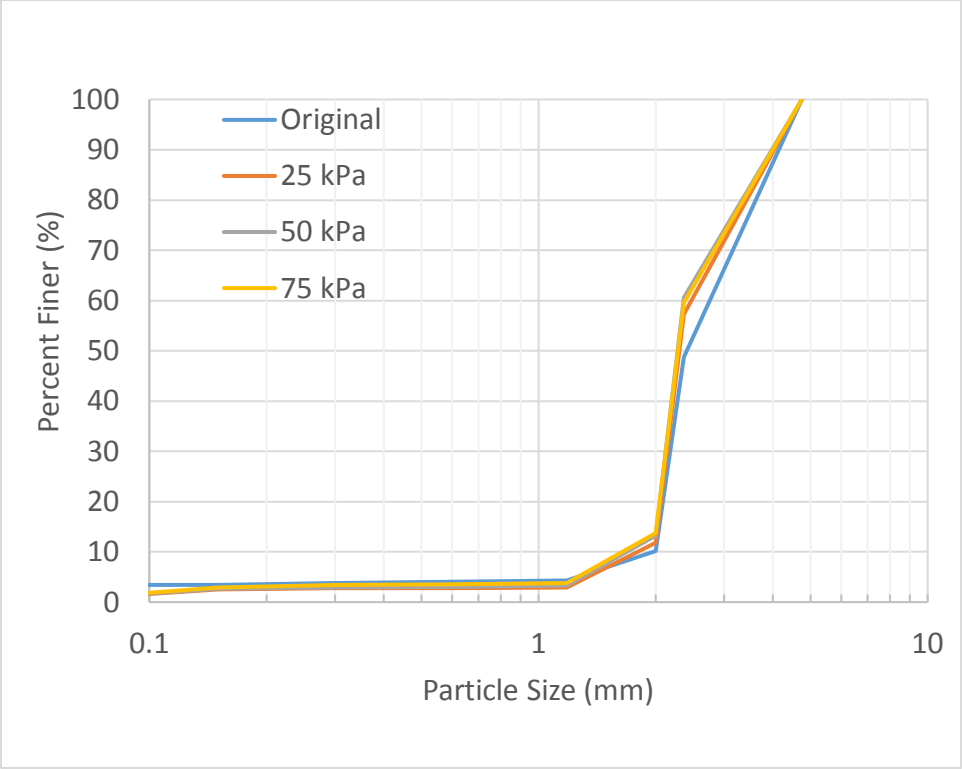

Sieve Analyses for Coarse Poraver – SSDS

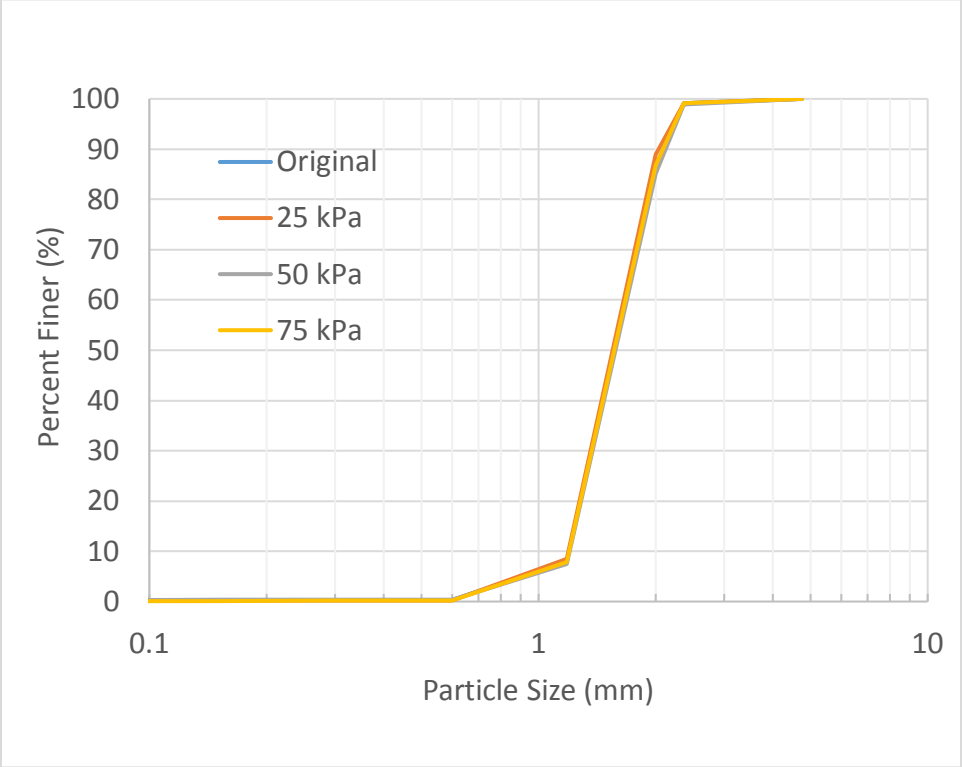

Sieve Analyses for Medium Kling – SSDS

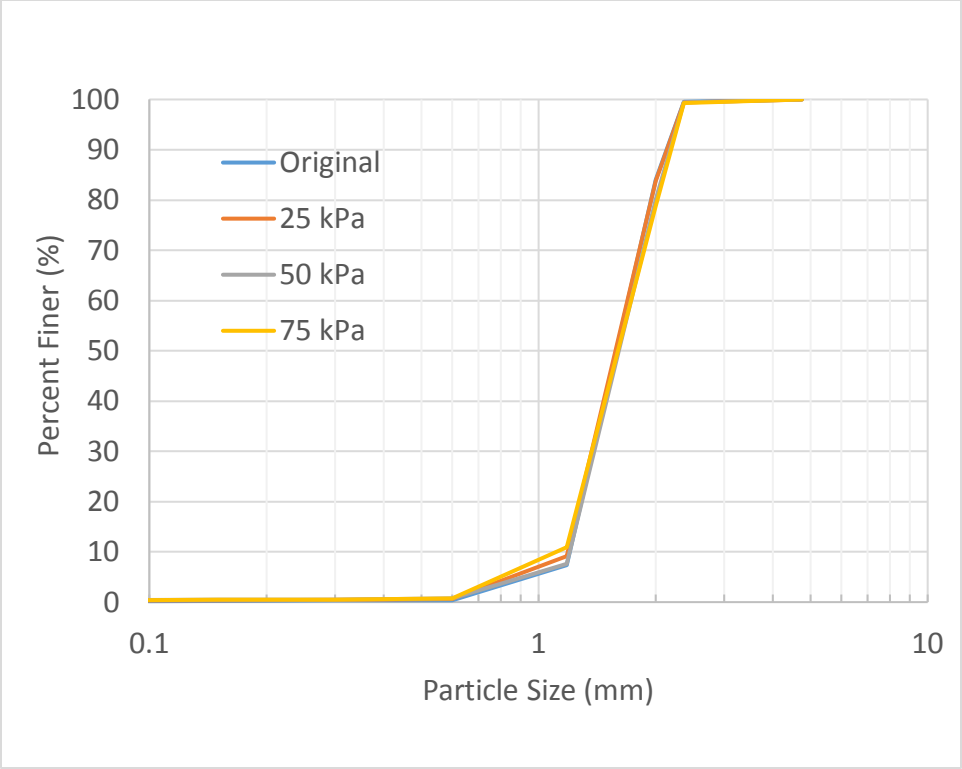

Sieve Analyses for Medium Limestone – SSDS

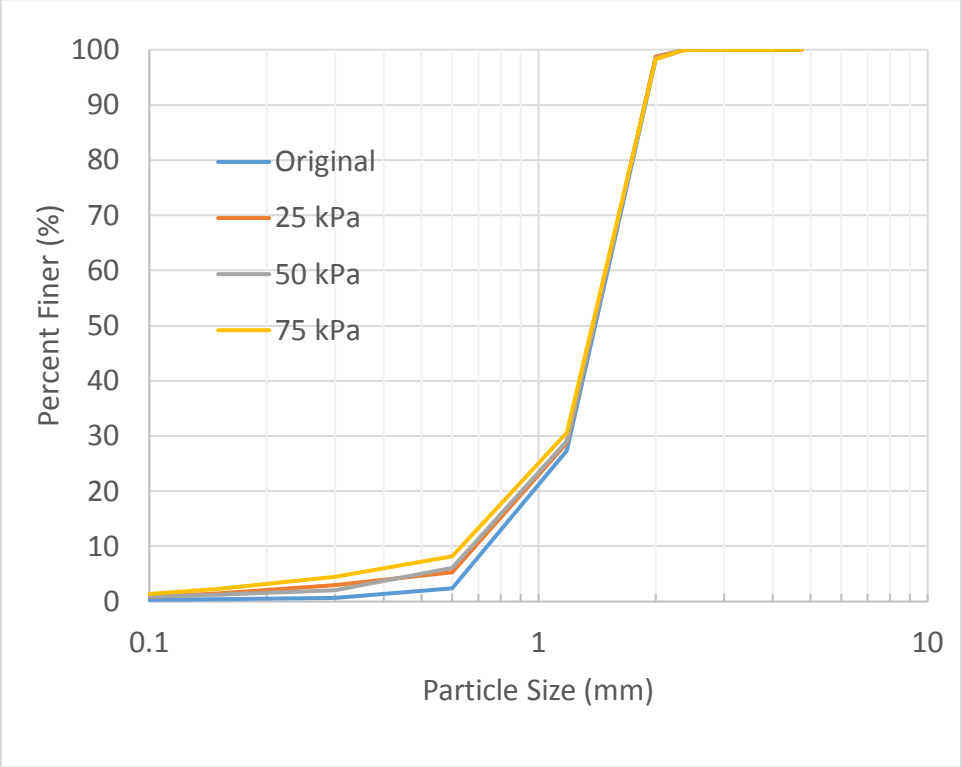

Sieve Analyses for Medium Poraver – SSDS

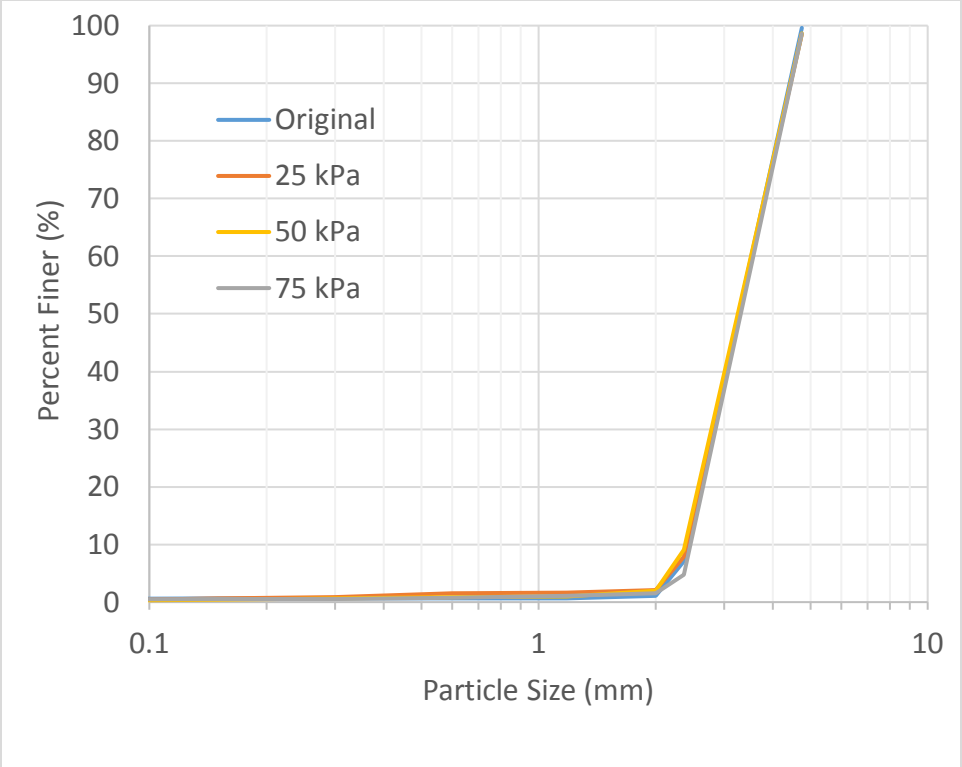

Sieve Analyses for Coarse Limestone – LSDS

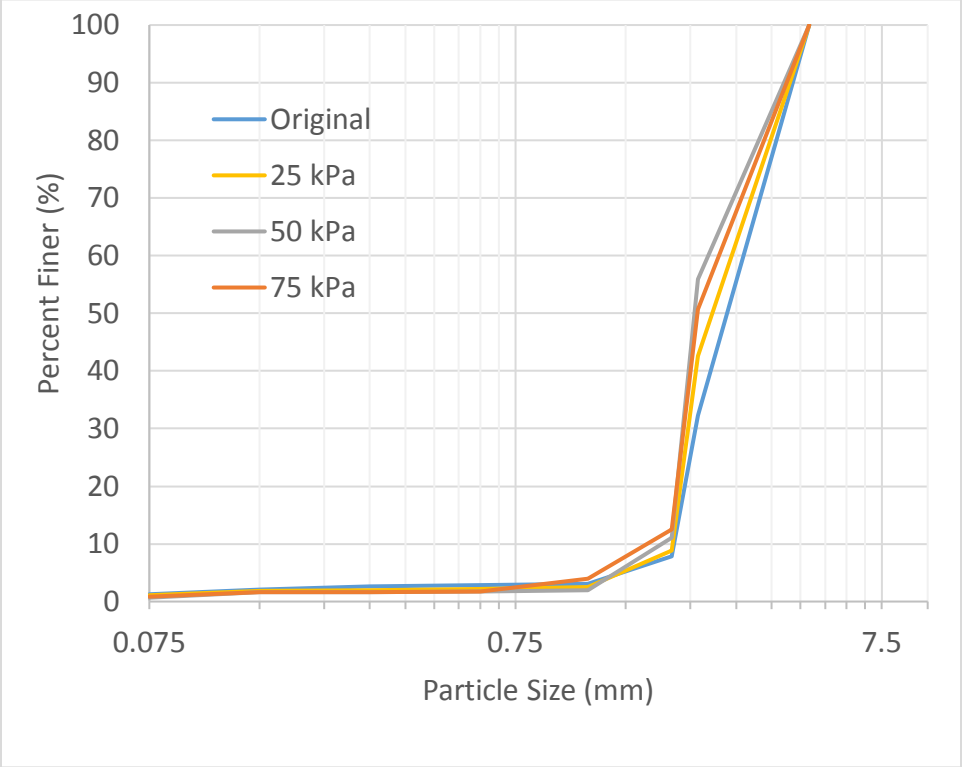

Sieve Analyses for Coarse Poraver – LSDS

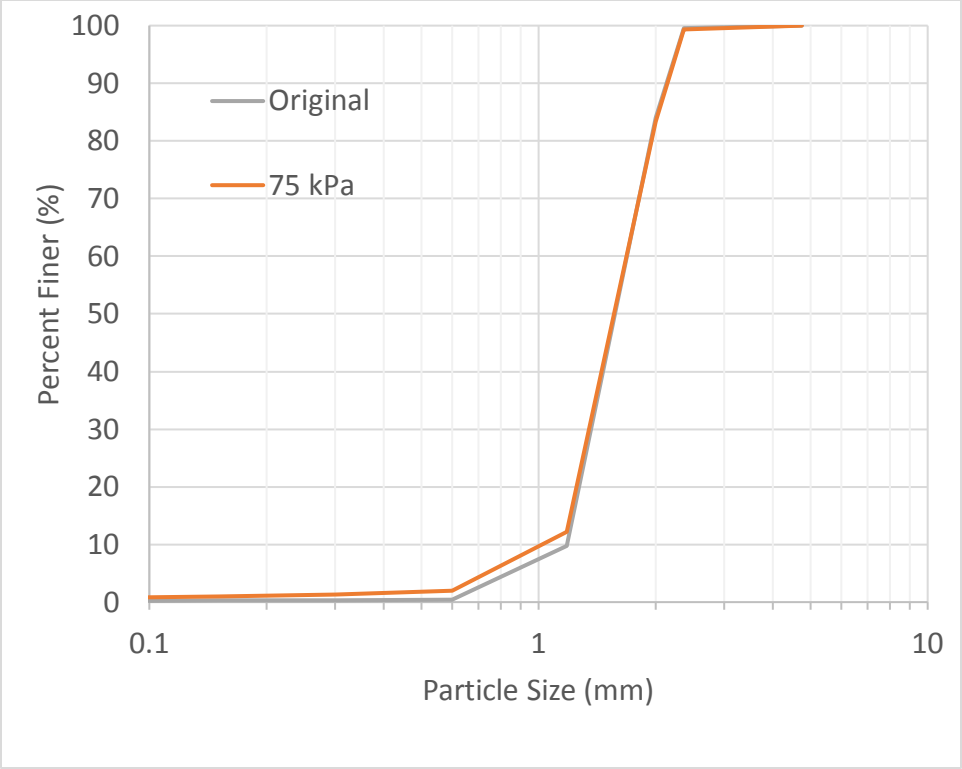

Sieve Analyses for Medium Limestone – LSDS

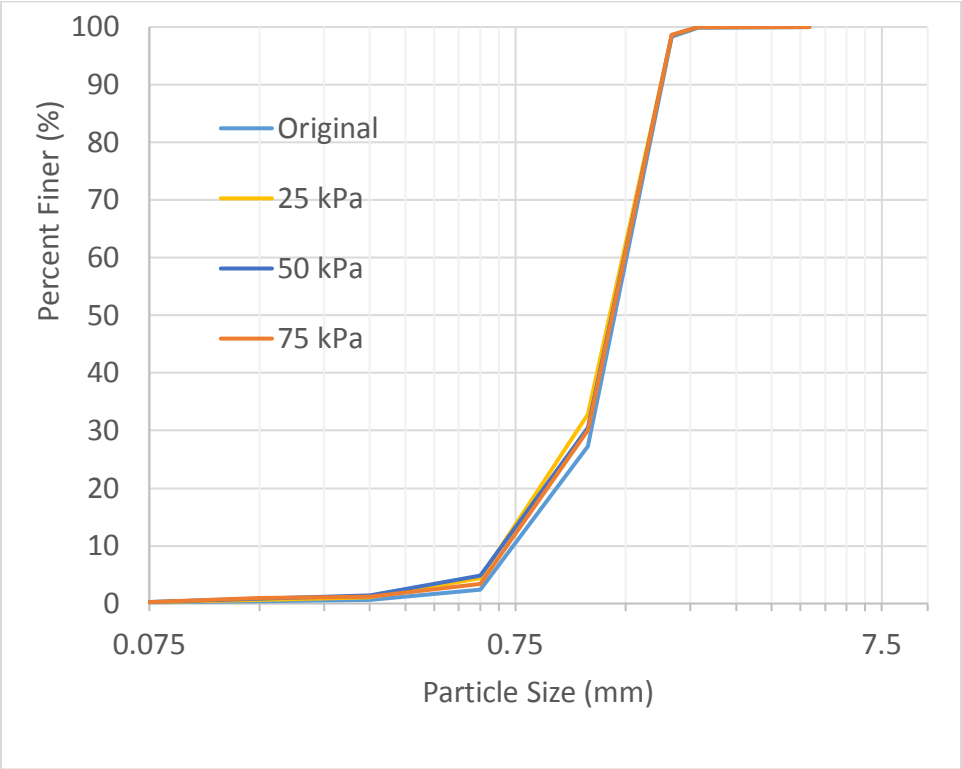

Sieve Analyses for Medium Poraver – LSDS

Appendix B – Shear Strength Data

Material	Gradation	Apparatus	Load Range	Test No.	ρ (g/cm³)	Nom. $\sigma_{v'}$ (kPa)	Avg. σ_v' (kPa)	τ_p (kPa)	τ_{cs} (kPa)	$\tau_{12\%}$ (kPa)	ϕ'_p	ϕ'_{cs}	α_p	$\phi'_{12\%}$	Comments
Kling	Coarse	SSDS	High	2	1.57	400	403.3	467.2	318.9	393.2	49.2	38.3	10.9	44.3	
Kling	Coarse	SSDS	High	4	1.57	400	401.4	456.5	315.3	369.6	48.7	38.2	10.5	42.6	
Kling	Coarse	SSDS	High	25	1.57	400	403.1	494.7	383.8	428.8	50.8	43.6	7.2	46.8	
Kling	Coarse	SSDS	High	5	1.58	500	500.9	571.9	442.7	490.2	48.8	41.5	7.3	44.4	
Kling	Coarse	SSDS	High	6	1.56	500	500.7	595.0	371.1	504.7	49.9	36.5	13.4	45.2	
Kling	Coarse	SSDS	High	7	1.56	500	500.0	549.0	391.3	456.7	47.7	38.0	9.6	42.4	
Kling	Coarse	SSDS	High	8	1.57	600	605.0	652.1	498.3	573.0	47.1	39.5	7.7	43.4	
Kling	Coarse	SSDS	High	9	1.56	600	604.7	648.8	477.4	560.3	47.0	38.3	8.7	42.8	
Kling	Coarse	SSDS	High	10	1.58	600	605.1	674.7	499.0	588.3	48.1	39.5	8.6	44.2	
Kling	Coarse	SSDS	High	1	1.57	1600	1585.7	1445.4	1371.7	1415.0	42.3	40.9	1.5	41.7	
Kling	Coarse	SSDS	High	25	1.57	400	400.8	494.7	325.7	428.8	51.0	39.1	11.9	46.9	*Cyclic
Kling	Coarse	SSDS	High	26	1.58	500	498.1	563.3	386.5	489.1	48.5	37.8	10.7	44.5	*Cyclic
Kling	Coarse	SSDS	High	27	1.57	600	603.9	689.4	468.0	626.0	48.8	37.8	11.0	46.0	*Cyclic
Kling	Coarse	SSDS	Low	12	1.57	25	30.7	46.8	35.1	34.8	56.8	48.9	7.9	48.6	
Kling	Coarse	SSDS	Low	20	1.56	25	29.8	55.7	38.9	44.7	61.8	52.5	9.3	56.3	
Kling	Coarse	SSDS	Low	21	1.56	25	30.7	57.5	32.0	40.8	61.9	46.2	15.7	53.1	
Kling	Coarse	SSDS	Low	14	1.55	50	54.7	73.8	54.9	57.1	53.5	45.2	8.3	46.2	
Kling	Coarse	SSDS	Low	15	1.54	50	54.1	76.3	62.2	56.1	54.7	49.0	5.7	46.0	
Kling	Coarse	SSDS	Low	22	1.55	50	54.6	84.2	54.2	62.0	57.0	44.8	12.2	48.6	
Kling	Coarse	SSDS	Low	19	1.56	75	80.1	109.6	72.6	83.2	53.8	42.2	11.7	46.1	
Kling	Coarse	SSDS	Low	23	1.58	75	80.9	122.0	78.0	94.6	56.5	44.0	12.5	49.5	
Kling	Coarse	SSDS	Low	24	1.56	75	81.5	114.0	77.6	83.0	54.4	43.6	10.8	45.5	
Limestone	Coarse	SSDS	High	22	1.45	400	401.4	425.3	395.0	417.0	46.7	44.5	2.1	46.1	
Limestone	Coarse	SSDS	High	23	1.43	400	400.9	424.3	392.6	407.6	46.6	44.4	2.2	45.5	
Limestone	Coarse	SSDS	High	24	1.43	400	405.5	429.4	374.6	401.7	46.6	42.7	3.9	44.7	
Limestone	Coarse	SSDS	High	25	1.44	500	500.5	481.0	453.3	464.9	43.9	42.2	1.7	42.9	
Limestone	Coarse	SSDS	High	26	1.43	500	498.4	497.5	471.8	479.0	44.9	43.4	1.5	43.9	
Limestone	Coarse	SSDS	High	27	1.42	500	498.9	486.6	462.8	485.6	44.3	42.8	1.4	44.2	
Limestone	Coarse	SSDS	High	29	1.42	600	603.5	608.2	582.8	586.6	45.2	44.0	1.2	44.2	

Limestone	Coarse	SSDS	High	30	1.42	600	602.0	599.0	569.8	586.4	44.9	43.4	1.4	44.2	
Limestone	Coarse	SSDS	High	60	1.47	600	603.2	587.6	550.7	568.7	44.3	42.4	1.9	43.3	
Limestone	Coarse	SSDS	High	6	1.45	1600	1585.7	1321.1	1301.9	1270.0	39.8	39.4	0.4	38.7	
Limestone	Coarse	SSDS	High	48	1.44	400	399.6	454.9	339.3	433.0	48.7	40.3	8.4	47.3	*Cyclic
Limestone	Coarse	SSDS	High	49	1.44	500	498.1	495.6	460.5	485.7	44.9	42.8	2.1	44.3	*Cyclic
Limestone	Coarse	SSDS	High	54	1.44	600	603.0	608.6	548.4	595.1	45.3	42.3	3.0	44.6	*Cyclic
Limestone	Coarse	SSDS	Low	31	1.42	25	30.2	50.7	n/a	48.9	59.2	n/a	n/a	58.3	
Limestone	Coarse	SSDS	Low	32	1.42	25	30.3	54.2	47.2	48.3	60.8	57.4	3.5	58.0	
Limestone	Coarse	SSDS	Low	40	1.44	25	31.1	61.7	44.3	56.1	63.3	54.9	8.3	61.0	
Limestone	Coarse	SSDS	Low	34	1.41	50	54.5	91.5	67.7	84.8	59.2	51.2	8.1	57.3	
Limestone	Coarse	SSDS	Low	36	1.41	50	59.5	86.6	76.7	84.7	55.5	52.2	3.3	54.9	
Limestone	Coarse	SSDS	Low	41	1.44	50	57.9	88.4	77.9	81.1	56.8	53.4	3.4	54.5	
Limestone	Coarse	SSDS	Low	6	1.43	75	74.3	112.4	95.7	101.0	56.5	52.2	4.4	53.6	
Limestone	Coarse	SSDS	Low	42	1.45	75	80.1	119.2	103.1	109.8	56.1	52.2	3.9	53.9	
Limestone	Coarse	SSDS	Low	43	1.43	75	79.5	116.6	112.2	101.0	55.7	54.7	1.0	51.8	
Limestone	Coarse	SSDS	Low	51	1.44	25	29.5	55.9	27.8	52.7	62.2	43.3	18.9	60.7	*Cyclic
Limestone	Coarse	SSDS	Low	53	1.43	50	52.3	91.2	51.8	85.9	60.2	44.7	15.5	58.7	*Cyclic
Limestone	Coarse	SSDS	Low	46	1.44	75	78.6	125.4	78.0	119.5	57.9	44.8	13.1	56.6	*Cyclic
Poraver	Coarse	SSDS	High	14	0.23	400	401.4	311.7	291.9	306.8	37.8	36.0	1.8	37.4	
Poraver	Coarse	SSDS	High	15	0.22	400	399.7	308.0	274.4	304.6	37.6	34.5	3.1	37.3	
Poraver	Coarse	SSDS	High	16	0.23	400	400.7	323.8	306.4	319.4	38.9	37.4	1.5	38.6	
Poraver	Coarse	SSDS	High	17	0.22	500	499.1	350.8	340.3	341.5	35.1	34.3	0.8	34.4	
Poraver	Coarse	SSDS	High	18	0.22	500	498.1	351.0	331.2	349.2	35.2	33.6	1.6	35.0	
Poraver	Coarse	SSDS	High	19	0.23	500	498.4	356.5	351.2	348.2	35.6	35.2	0.4	34.9	
Poraver	Coarse	SSDS	High	20	0.23	600	602.6	392.3	369.7	386.3	33.1	31.5	1.5	32.7	
Poraver	Coarse	SSDS	High	21	0.22	600	603.3	420.5	389.1	419.9	34.9	32.8	2.1	34.8	
Poraver	Coarse	SSDS	High	22	0.22	600	602.9	401.7	392.0	394.4	33.7	33.0	0.6	33.2	
Poraver	Coarse	SSDS	High	13	0.23	1600	1585.7	652.8	569.9	580.9	22.4	19.8	2.6	20.1	
Poraver	Coarse	SSDS	Low	23	0.22	25	32.6	51.5	32.9	38.2	57.7	45.3	12.4	49.6	
Poraver	Coarse	SSDS	Low	24	0.22	25	31.6	48.7	30.8	35.8	57.0	44.2	12.8	48.6	
Poraver	Coarse	SSDS	Low	32	0.22	25	30.2	54.6	30.2	38.9	61.0	45.0	16.1	52.2	

Poraver	Coarse	SSDS	Low	26	0.22	50	55.5	85.3	68.2	79.8	56.9	50.9	6.1	55.2	
Poraver	Coarse	SSDS	Low	27	0.23	50	54.5	82.8	57.5	67.7	56.6	46.5	10.1	51.1	
Poraver	Coarse	SSDS	Low	28	0.23	50	54.3	77.3	57.7	65.0	54.9	46.7	8.2	50.1	
Poraver	Coarse	SSDS	Low	29	0.22	75	79.8	105.2	70.1	95.5	52.8	41.3	11.5	50.1	
Poraver	Coarse	SSDS	Low	30	0.22	75	79.4	103.2	78.6	88.9	52.4	44.7	7.7	48.2	
Poraver	Coarse	SSDS	Low	31	0.22	75	80.1	104.6	75.8	91.5	52.6	43.4	9.1	48.8	
Poraver	Coarse	SSDS	Low	33	0.22	25	29.7	46.4	21.2	31.2	57.4	35.5	21.8	46.4	*Cyclic
Poraver	Coarse	SSDS	Low	34	0.23	50	53.7	71.5	41.3	54.6	53.1	37.5	15.5	45.5	*Cyclic
Poraver	Coarse	SSDS	Low	35	0.23	75	78.3	104.2	73.1	91.7	53.1	43.0	10.1	49.5	*Cyclic
Kling	Medium	SSDS	High	2	1.58	400	397.2	432.7	301.6	309.2	47.4	37.2	10.2	37.9	
Kling	Medium	SSDS	High	3	1.56	400	401.3	418.4	288.3	296.3	46.2	35.7	10.5	36.4	
Kling	Medium	SSDS	High	4	1.56	400	400.4	426.2	302.2	314.6	46.8	37.0	9.7	38.2	
Kling	Medium	SSDS	High	5	1.59	500	500.8	501.2	363.9	381.9	45.0	36.0	9.0	37.3	
Kling	Medium	SSDS	High	6	1.57	500	502.4	495.3	351.4	381.8	44.6	35.0	9.6	37.2	
Kling	Medium	SSDS	High	7	1.59	500	501.3	501.7	352.3	388.3	45.0	35.1	9.9	37.8	
Kling	Medium	SSDS	High	8	1.55	600	603.7	607.7	443.4	463.4	45.2	36.3	8.9	37.5	
Kling	Medium	SSDS	High	9	1.57	600	604.4	577.5	427.7	456.5	43.7	35.3	8.4	37.1	
Kling	Medium	SSDS	High	10	1.58	600	605.0	580.9	457.8	455.1	43.8	37.1	6.7	37.0	
Kling	Medium	SSDS	High	1	1.58	1600	1585.7	1376.8	1183.3	1296.1	41.0	36.7	4.2	39.3	
Kling	Medium	SSDS	Low	11	1.56	25	30.8	36.0	24.4	23.8	49.5	38.4	11.1	37.7	
Kling	Medium	SSDS	Low	12	1.56	25	32.1	36.7	23.8	24.2	48.8	36.5	12.3	37.0	
Kling	Medium	SSDS	Low	13	1.59	25	27.2	39.1	26.7	29.0	55.1	44.4	10.7	46.8	
Kling	Medium	SSDS	Low	14	1.58	50	57.2	75.8	50.1	54.8	53.0	41.2	11.7	43.8	
Kling	Medium	SSDS	Low	15	1.58	50	60.1	66.9	46.4	46.6	48.1	37.7	10.4	37.8	
Kling	Medium	SSDS	Low	16	1.56	50	55.6	70.0	47.3	48.9	51.6	40.4	11.1	41.4	
Kling	Medium	SSDS	Low	17	1.57	75	79.8	91.9	58.5	58.5	49.0	36.3	12.8	36.3	
Kling	Medium	SSDS	Low	20	1.59	75	79.7	94.6	57.1	63.4	49.9	35.6	14.3	38.5	
Kling	Medium	SSDS	Low	21	1.60	75	79.0	91.9	57.7	58.2	49.3	36.2	13.2	36.4	
Limestone	Medium	SSDS	High	15	1.47	400	400.7	373.3	305.1	337.2	43.0	37.3	5.7	40.1	
Limestone	Medium	SSDS	High	16	1.48	400	401.1	376.3	313.1	327.8	43.2	38.0	5.2	39.3	
Limestone	Medium	SSDS	High	17	1.48	400	399.7	349.6	305.6	315.6	41.2	37.4	3.8	38.3	

Limestone	Medium	SSDS	High	18	1.47	500	497.4	439.6	380.5	414.9	41.5	37.4	4.1	39.8	
Limestone	Medium	SSDS	High	19	1.49	500	500.7	447.4	376.4	420.2	41.8	36.9	4.8	40.0	
Limestone	Medium	SSDS	High	20	1.50	500	499.0	423.0	369.2	397.6	40.3	36.5	3.8	38.6	
Limestone	Medium	SSDS	High	21	1.48	600	601.8	519.2	474.3	493.8	40.8	38.2	2.5	39.4	
Limestone	Medium	SSDS	High	22	1.44	600	603.2	526.6	436.2	482.2	41.1	35.9	5.2	38.6	
Limestone	Medium	SSDS	High	23	1.48	600	603.9	524.6	467.4	496.6	41.0	37.7	3.2	39.4	
Limestone	Medium	SSDS	High	14	1.45	1600	1585.7	1228.5	1213.6	1203.5	37.8	37.4	0.3	37.2	
Limestone	Medium	SSDS	Low	24	1.47	25	30.5	36.9	30.2	31.1	50.5	44.7	5.7	45.6	
Limestone	Medium	SSDS	Low	25	1.48	25	29.1	38.5	30.4	34.9	53.0	46.3	6.6	50.2	
Limestone	Medium	SSDS	Low	26	1.47	25	29.1	42.6	32.9	35.0	55.7	48.5	7.1	50.2	
Limestone	Medium	SSDS	Low	27	1.47	50	53.8	62.5	45.9	48.7	49.3	40.5	8.8	42.2	
Limestone	Medium	SSDS	Low	28	1.46	50	53.9	64.8	50.1	51.8	50.3	42.9	7.4	43.9	
Limestone	Medium	SSDS	Low	29	1.47	50	55.9	65.6	49.8	54.2	49.6	41.7	7.9	44.1	
Limestone	Medium	SSDS	Low	30	1.46	75	78.9	94.1	67.9	78.8	50.0	40.7	9.3	45.0	
Limestone	Medium	SSDS	Low	31	1.47	75	79.4	94.6	67.0	77.6	50.0	40.2	9.8	44.4	
Limestone	Medium	SSDS	Low	32	1.48	75	79.1	97.1	65.5	78.0	50.8	39.7	11.2	44.6	
Poraver	Medium	SSDS	High	14	0.28	400	399.6	337.0	292.3	303.8	40.1	36.2	4.0	37.2	
Poraver	Medium	SSDS	High	15	0.28	400	400.7	344.2	288.3	295.2	40.7	35.7	4.9	36.4	
Poraver	Medium	SSDS	High	16	0.27	400	401.0	339.8	288.1	290.0	40.3	35.7	4.6	35.9	
Poraver	Medium	SSDS	High	17	0.29	500	499.0	394.9	359.3	361.1	38.4	35.8	2.6	35.9	
Poraver	Medium	SSDS	High	18	0.27	500	499.3	387.5	341.8	373.4	37.8	34.4	3.4	36.8	
Poraver	Medium	SSDS	High	19	0.27	500	498.8	396.7	360.4	371.4	38.5	35.8	2.6	36.7	
Poraver	Medium	SSDS	High	20	0.28	600	602.4	442.1	387.3	397.1	36.3	32.7	3.5	33.4	
Poraver	Medium	SSDS	High	21	0.28	600	603.2	456.3	409.4	434.5	37.1	34.2	2.9	35.8	
Poraver	Medium	SSDS	High	22	0.28	600	602.5	439.8	394.5	396.9	36.1	33.2	2.9	33.4	
Poraver	Medium	SSDS	High	13	0.27	1600	1585.7	978.9	n/a	903.6	31.7	n/a	n/a	29.7	
Poraver	Medium	SSDS	Low	24	0.28	25	30.8	36.7	20.2	18.5	50.0	33.2	16.8	31.0	
Poraver	Medium	SSDS	Low	25	0.26	25	31.5	37.4	21.4	22.7	50.0	34.2	15.7	35.8	
Poraver	Medium	SSDS	Low	32	0.26	25	29.7	34.9	20.6	17.6	49.6	34.7	14.9	30.7	
Poraver	Medium	SSDS	Low	26	0.26	50	57.4	58.5	36.7	33.4	45.6	32.6	12.9	30.2	
Poraver	Medium	SSDS	Low	27	0.27	50	54.9	59.6	34.5	33.1	47.3	32.2	15.2	31.0	

Poraver	Medium	SSDS	Low	28	0.26	50	56.2	63.4	35.4	39.2	48.4	32.2	16.2	34.9	
Poraver	Medium	SSDS	Low	29	0.26	75	80.3	82.9	52.6	49.9	45.9	33.2	12.7	31.9	
Poraver	Medium	SSDS	Low	30	0.27	75	79.8	85.6	50.5	52.0	47.0	32.3	14.7	33.1	
Poraver	Medium	SSDS	Low	31	0.26	75	80.3	87.4	52.1	52.1	47.4	33.0	14.4	33.0	
Limestone	Coarse	LSDS	High	55	1.42	400	n/a	449.4	445.3	438.2	48.3	48.1	0.3	47.6	
Limestone	Coarse	LSDS	High	56	1.42	400	n/a	477.8	475.6	457.1	50.1	49.9	0.1	48.8	
Limestone	Coarse	LSDS	High	57	1.42	500	n/a	544.6	533.9	511.9	47.4	46.9	0.6	45.7	
Limestone	Coarse	LSDS	High	58	1.43	500	n/a	501.3	498.4	484.6	45.1	44.9	0.2	44.1	
Limestone	Coarse	LSDS	High	16	1.43	600	n/a	639.9	n/a	n/a	46.8	n/a	n/a	n/a	
Limestone	Coarse	LSDS	High	17	1.42	600	n/a	621.2	619.8	602.4	46.0	45.9	0.1	45.1	
Limestone	Coarse	LSDS	Low	11	1.41	25	25.0	41.2	35.0	35.0	58.7	54.4	4.3	54.4	*11.4% strain rather than 12%
Limestone	Coarse	LSDS	Low	12	1.43	25	25.1	36.9	35.2	34.6	55.8	54.5	1.3	54.1	*11.4% strain rather than 12%
Limestone	Coarse	LSDS	Low	15	1.42	25	25.0	37.7	33.9	33.9	56.4	53.6	2.8	53.5	*11.4% strain rather than 12%
Limestone	Coarse	LSDS	Low	13	1.43	50	50.8	64.8	63.8	64.0	51.9	51.4	0.4	51.5	*11.4% strain rather than 12%
Limestone	Coarse	LSDS	Low	14	1.42	50	50.8	69.6	66.0	65.8	53.9	52.4	1.5	52.3	*11.4% strain rather than 12%
Limestone	Coarse	LSDS	Low	8	1.41	75	75.5	111.6	109.9	110.2	55.9	55.5	0.4	55.6	*11.4% strain rather than 12%
Limestone	Coarse	LSDS	Low	9	1.42	75	75.5	95.5	89.3	89.7	51.7	49.8	1.9	49.9	*11.4% strain rather than 12%
Limestone	Coarse	LSDS	Low	10	1.42	75	75.5	105.7	101.1	102.7	54.5	53.2	1.2	53.7	*11.4% strain rather than 12%
Limestone	Coarse	LSDS	Low	59	1.42	75	75.5	107.0	100.6	98.4	54.8	53.1	1.7	52.5	*11.4% strain rather than 12%
Poraver	Coarse	LSDS	High	1	0.22	400	n/a	275.5	n/a	259.4	34.6	n/a	n/a	33.0	
Poraver	Coarse	LSDS	High	2	0.22	400	n/a	267.6	264.9	264.5	33.8	33.5	0.3	33.5	
Poraver	Coarse	LSDS	High	3	0.22	500	n/a	317.8	n/a	301.8	32.4	n/a	n/a	31.1	
Poraver	Coarse	LSDS	High	4	0.22	500	n/a	321.5	n/a	303.0	32.7	n/a	n/a	31.2	
Poraver	Coarse	LSDS	High	5	0.22	600	n/a	352.8	352.5	339.9	30.5	30.4	0.0	29.5	
Poraver	Coarse	LSDS	High	6	0.23	600	n/a	328.1	324.6	324.8	28.7	28.4	0.3	28.4	
Poraver	Coarse	LSDS	Low	9	0.23	25	25.1	40.8	32.2	32.6	58.4	52.1	6.3	52.4	
Poraver	Coarse	LSDS	Low	10	0.24	25	25.2	40.2	31.1	31.4	57.9	51.0	6.9	51.3	
Poraver	Coarse	LSDS	Low	11	0.23	50	50.8	68.9	59.0	59.6	53.6	49.3	4.3	49.6	
Poraver	Coarse	LSDS	Low	12	0.23	50	50.9	73.8	55.0	60.9	55.4	47.2	8.2	50.1	
Poraver	Coarse	LSDS	Low	7	0.22	75	75.5	103.7	82.1	92.9	53.9	47.4	6.5	50.9	
Poraver	Coarse	LSDS	Low	8	0.22	75	75.5	106.3	81.0	90.6	54.6	47.0	7.6	50.2	

Limestone	Medium	LSDS	High	9	1.46	400	n/a	392.6	379.4	384.8	44.5	43.5	1.0	43.9	
Limestone	Medium	LSDS	High	10	1.48	400	n/a	405.9	394.5	390.7	45.4	44.6	0.8	44.3	
Limestone	Medium	LSDS	High	11	1.45	500	n/a	514.2	n/a	481.9	45.8	n/a	n/a	43.9	
Limestone	Medium	LSDS	High	12	1.45	500	n/a	503.5	500.2	473.9	45.2	45.0	0.2	43.5	
Limestone	Medium	LSDS	High	13	1.45	600	n/a	607.6	607.3	580.1	45.4	45.3	0.0	44.0	
Limestone	Medium	LSDS	High	33	1.46	600	n/a	594.8	594.3	574.8	44.8	44.7	0.0	43.8	
Limestone	Medium	LSDS	Low	1	1.46	25	25.1	33.5	32.5	32.7	53.2	52.3	0.9	52.5	*11.4% strain rather than 12%
Limestone	Medium	LSDS	Low	2	1.46	25	25.2	29.9	29.9	31.7	49.9	49.9	0.0	51.6	*11.4% strain rather than 12%
Limestone	Medium	LSDS	Low	4	1.48	50	50.9	66.2	63.4	63.3	52.5	51.3	1.2	51.2	*11.4% strain rather than 12%
Limestone	Medium	LSDS	Low	34	1.45	50	50.9	65.7	61.3	61.9	52.2	50.3	1.9	50.6	*11.4% strain rather than 12%
Limestone	Medium	LSDS	Low	6	1.46	75	75.5	88.4	86.4	86.9	49.5	48.8	0.7	49.0	*11.4% strain rather than 12%
Limestone	Medium	LSDS	Low	7	1.47	75	75.5	96.1	85.8	85.8	51.9	48.6	3.2	48.7	*11.4% strain rather than 12%
Limestone	Medium	LSDS	Low	8	1.47	75	75.5	88.1	86.3	87.4	49.4	48.8	0.6	49.2	*11.4% strain rather than 12%
Poraver	Medium	LSDS	High	1	0.27	400	n/a	315.4	301.8	312.1	38.3	37.0	1.2	38.0	
Poraver	Medium	LSDS	High	2	0.27	400	n/a	307.6	300.0	300.3	37.6	36.9	0.7	36.9	
Poraver	Medium	LSDS	High	3	0.28	500	n/a	343.6	342.6	341.5	34.5	34.4	0.1	34.3	
Poraver	Medium	LSDS	High	4	0.27	500	n/a	347.2	335.6	344.6	34.8	33.9	0.9	34.6	
Poraver	Medium	LSDS	High	5	0.27	600	n/a	382.5	381.8	378.7	32.5	32.5	0.1	32.3	
Poraver	Medium	LSDS	High	6	0.27	600	n/a	400.7	398.6	382.5	33.7	33.6	0.1	32.5	
Poraver	Medium	LSDS	Low	9	0.28	25	25.0	30.6	23.9	25.0	50.8	43.8	7.0	45.1	
Poraver	Medium	LSDS	Low	10	0.28	25	25.1	32.1	25.8	27.5	51.9	45.8	6.2	47.6	
Poraver	Medium	LSDS	Low	11	0.28	50	50.8	65.7	51.0	50.9	52.3	45.1	7.2	45.1	
Poraver	Medium	LSDS	Low	12	0.28	50	50.8	67.4	54.9	55.1	53.0	47.2	5.8	47.3	
Poraver	Medium	LSDS	Low	7	0.27	75	75.5	99.5	70.4	76.1	52.8	43.0	9.8	45.2	
Poraver	Medium	LSDS	Low	8	0.28	75	75.5	101.5	73.0	79.4	53.4	44.1	9.3	46.5	

Appendix C - Photographs

Coarse Kling – 25 kPa – SSDS

Coarse Kling – 50 kPa – SSDS

Coarse Kling – 75 kPa – SSDS

Coarse Kling – 400 kPa – SSDS

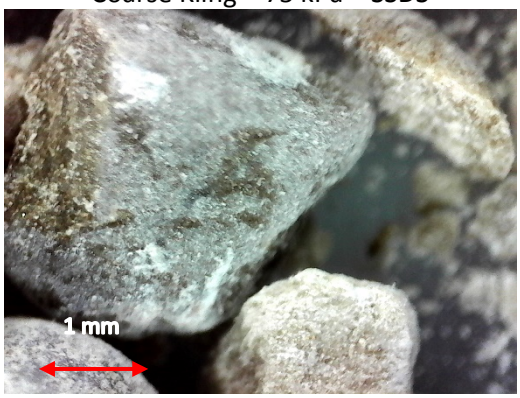

Coarse Kling – 500 kPa – SSDS

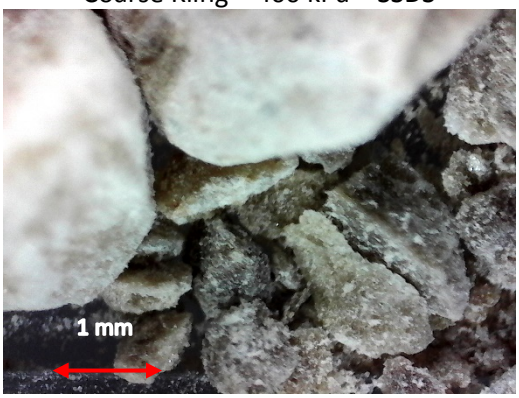

Coarser Kling – 600 kPa – SSDS

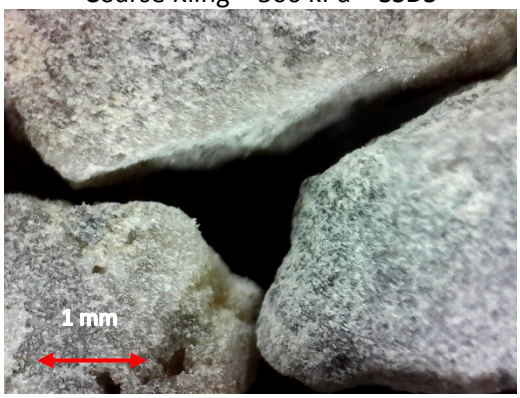

Coarse Limestone – 25 kPa – SSDS

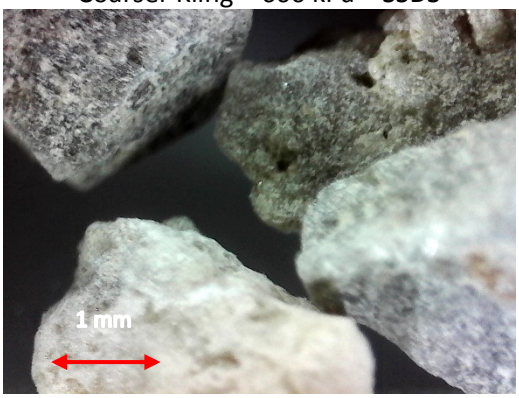

Coarse Limestone – 50 kPa – SSDS

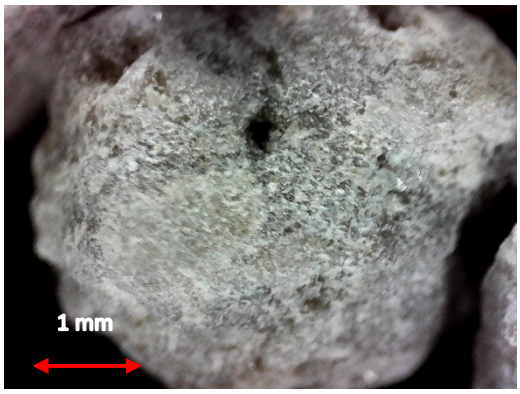

Coarse Limestone – 75 kPa – SSDS

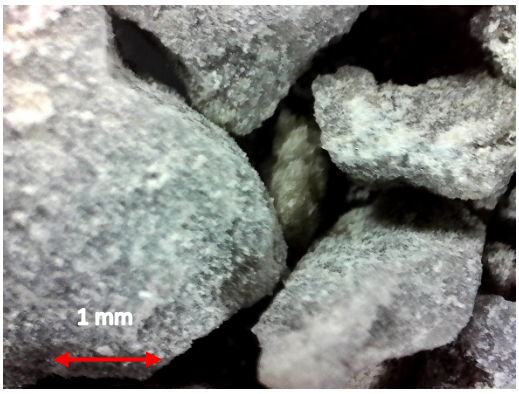

Coarse Limestone – 400 kPa – SSDS

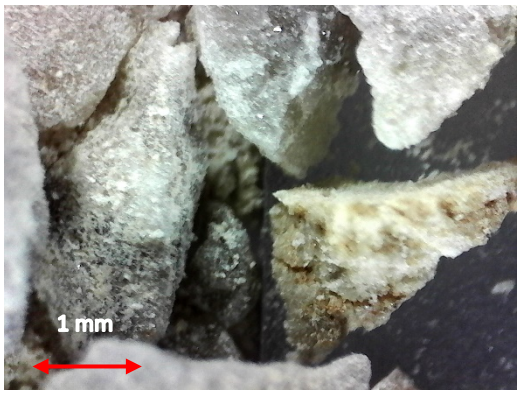

Coarse Limestone – 500 kPa – SSDS

Coarse Limestone – 600 kPa – SSDS

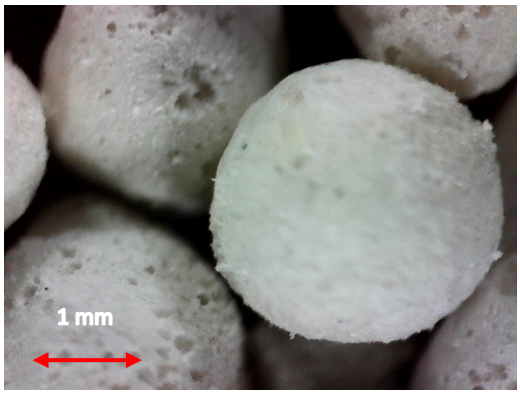

Coarse Poraver – 25 kPa – SSDS

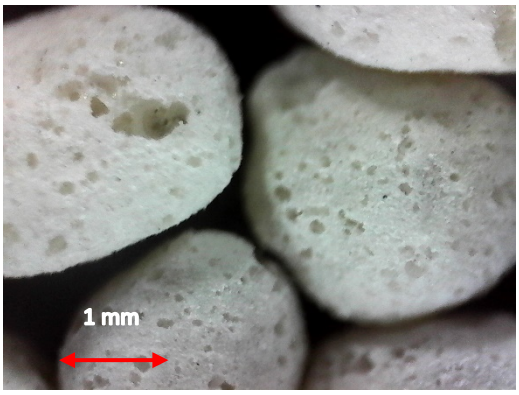

Coarse Poraver – 50 kPa – SSDS

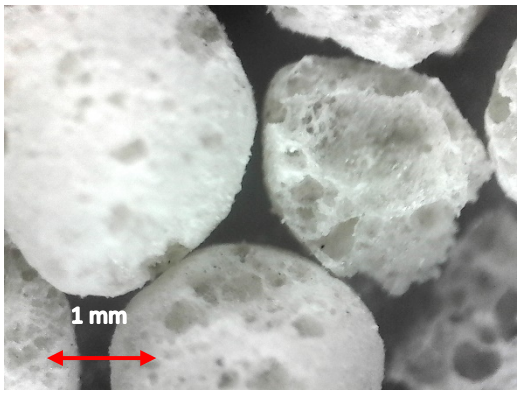

Coarse Poraver – 75 kPa – SSDS

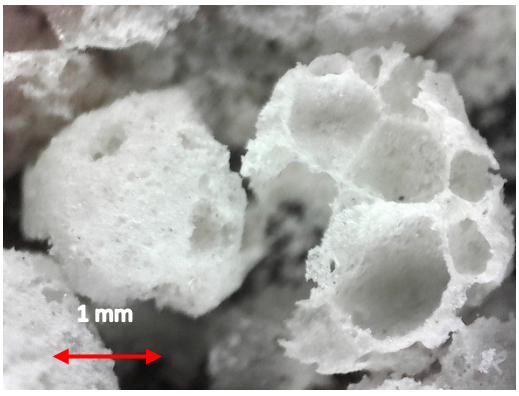

Coarse Poraver – 400 kPa - SSDS

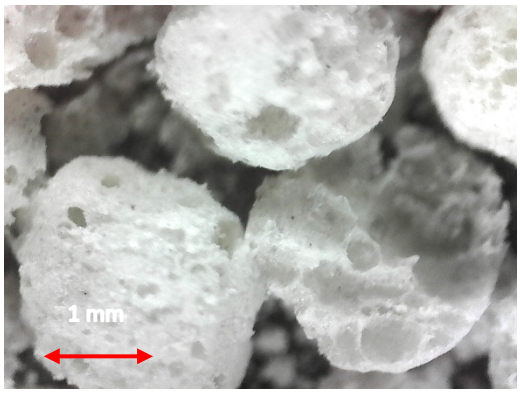

Coarse Poraver – 500 kPa - SSDS

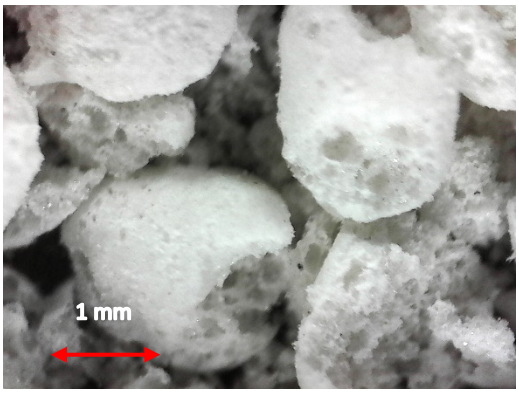

Coarse Poraver – 600 kPa - SSDS

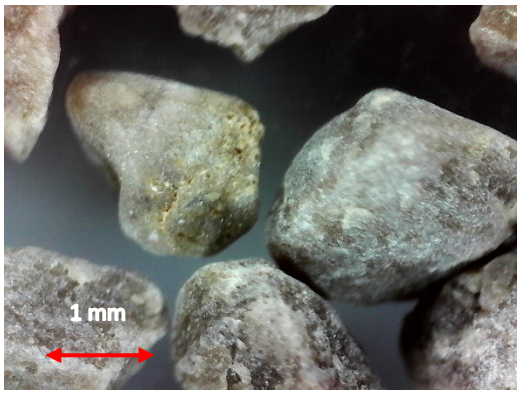

Medium Kling – 25 kPa – SSDS

Medium Kling – 50 kPa – SSDS

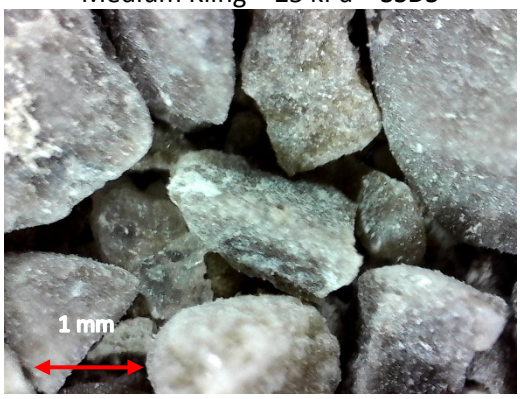

Medium Kling – 400 kPa – SSDS

Medium Kling – 500 kPa – SSDS

Medium Kling – 600 kPa – SSDS

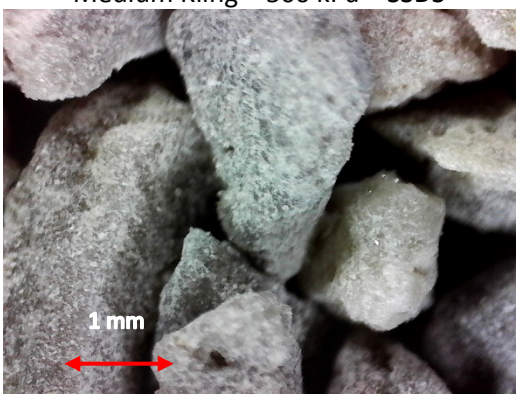

Medium Limestone – 25 kPa – SSDS

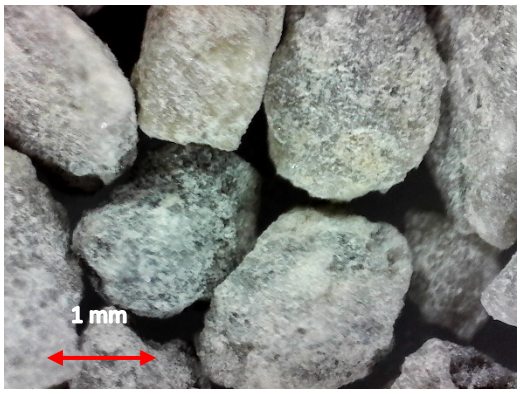

Medium Limestone – 50 kPa - SSDS

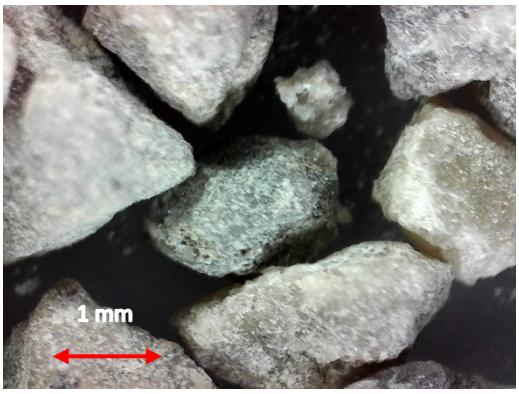

Medium Limestone – 75 kPa – SSDS

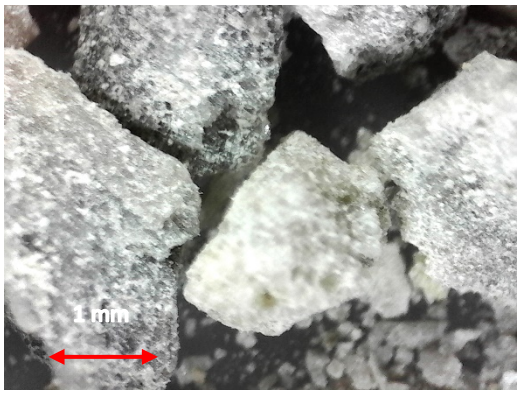

Medium Limestone – 400 kPa – SSDS

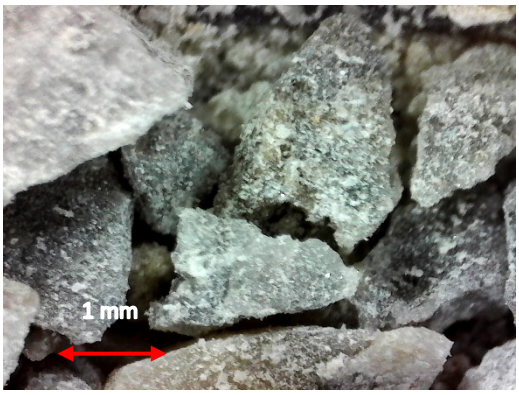

Medium Limestone – 500 kPa – SSDS

Medium Limestone – 600 kPa – SSDS

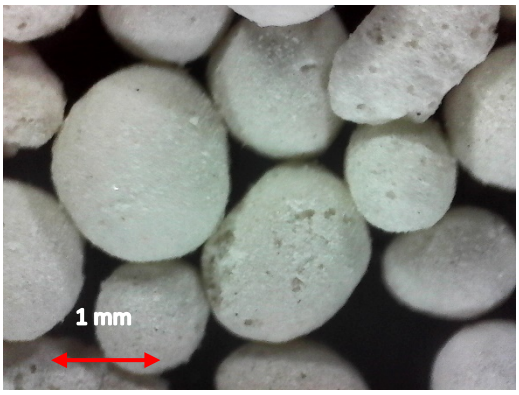

Medium Poraver – 25 kPa – SSDS

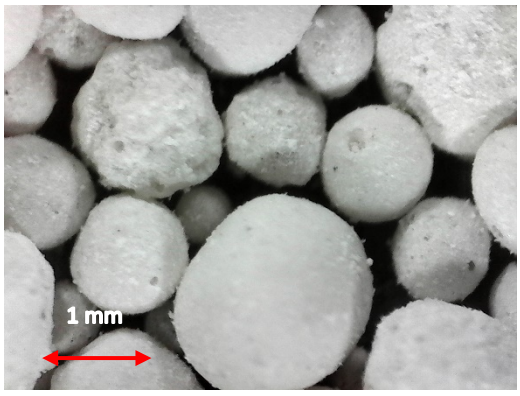

Medium Poraver – 50 kPa – SSDS

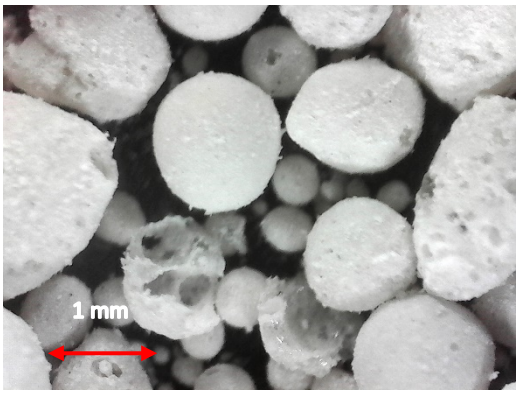

Medium Poraver – 75 kPa – SSDS

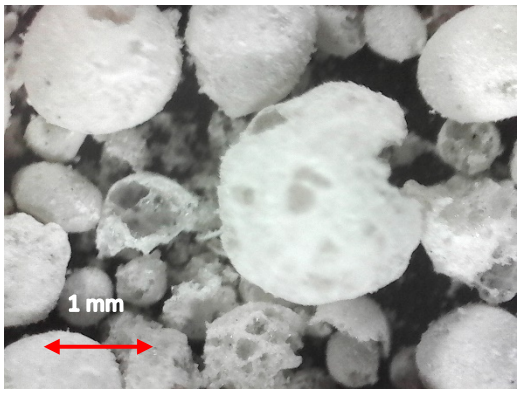

Medium Poraver – 400 kPa – SSDS

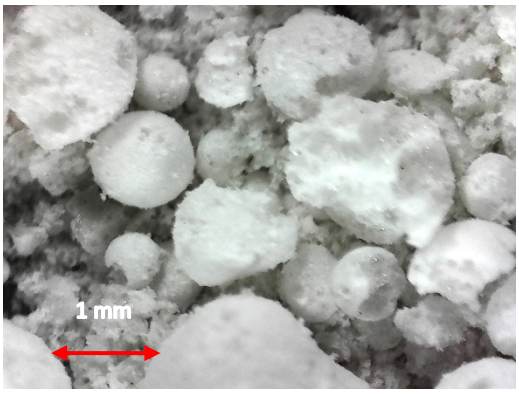

Medium Poraver – 500 kPa – SSDS

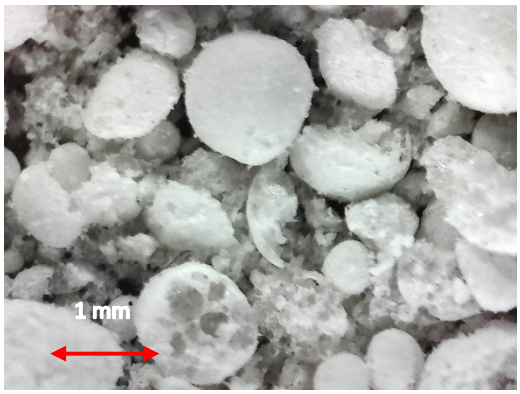

Medium Poraver – 600 kPa – SSDS

Coarse Limestone – 400 kPa – LSDS

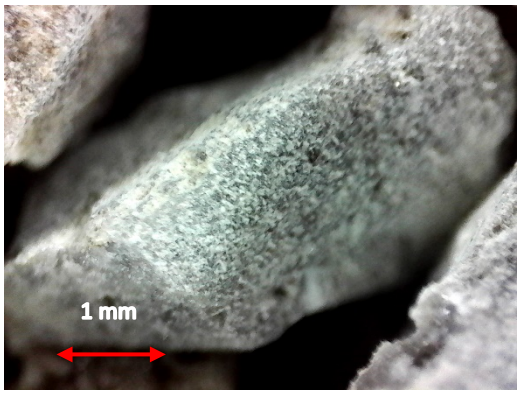

Coarse Limestone – 500 kPa – LSDS

Coarse Limestone – 600 kPa – LSDS

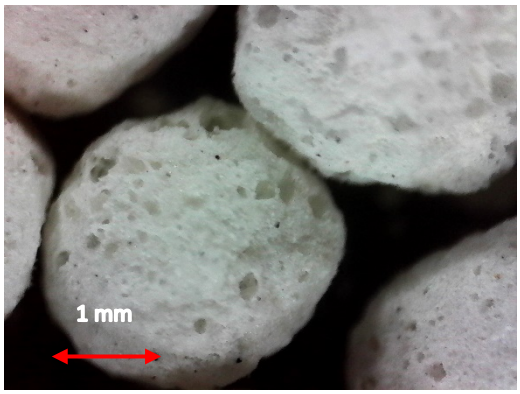

Coarse Poraver – 25 kPa – LSDS

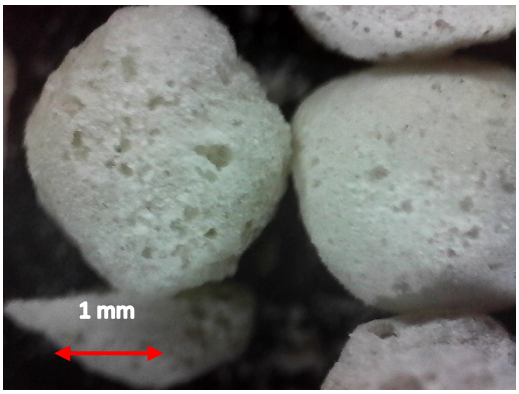

Coarse Poraver – 50 kPa – LSDS

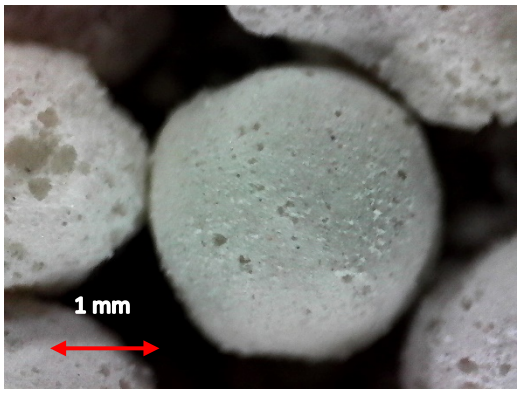

Coarse Poraver – 75 kPa – LSDS

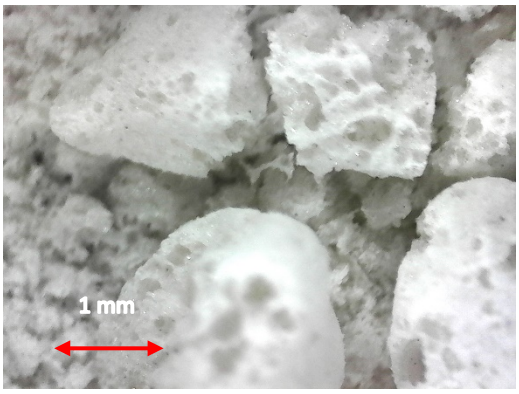

Coarse Poraver – 500 kPa – LSDS

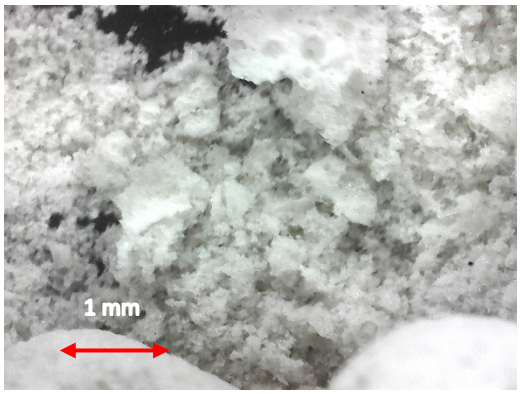

Coarse Poraver – 600 kPa – LSDS

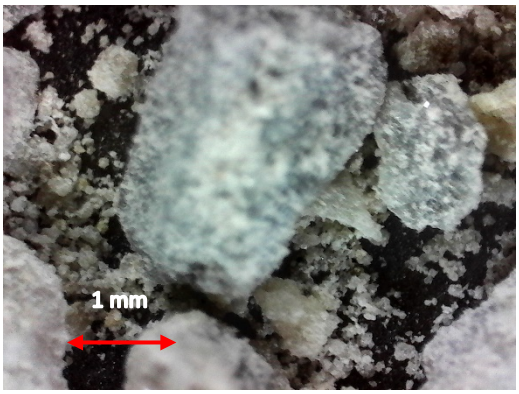

Medium Limestone – 400 kPa – LSDS

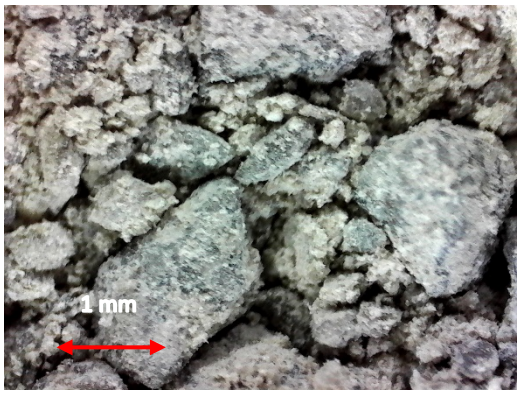

Medium Limestone – 500 kPa – LSDS

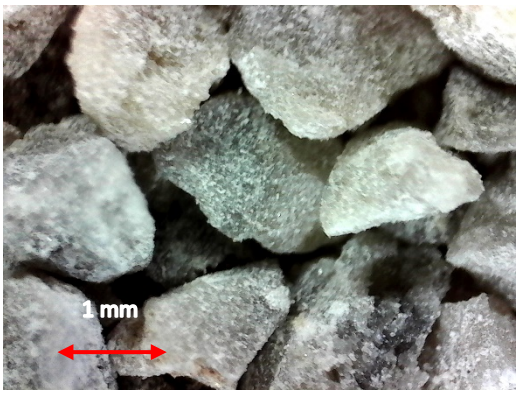

Medium Limestone – 600 kPa – SSDS

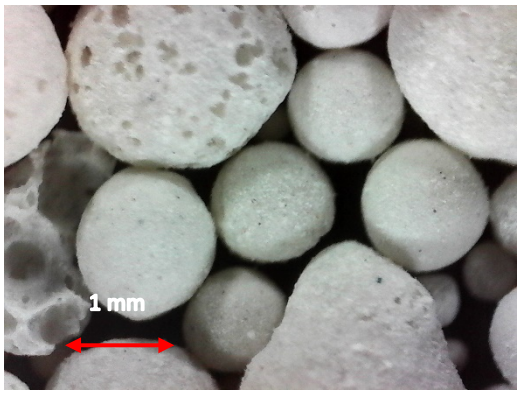

Medium Poraver – 25 kPa – LSDS

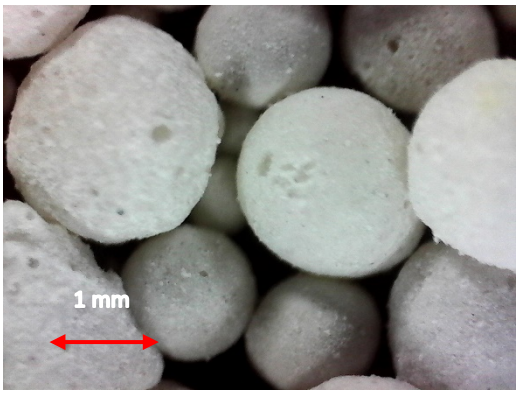

Medium Poraver – 50 kPa - LSDS

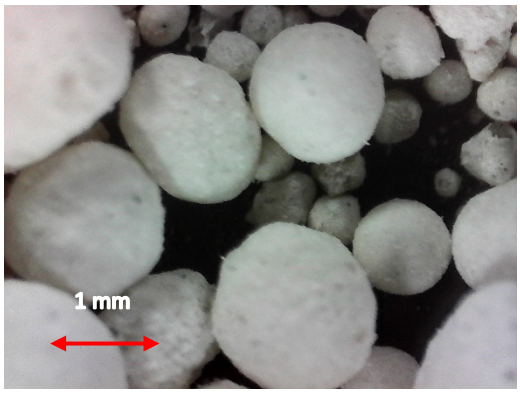

Medium Poraver – 75 kPa – LSDS

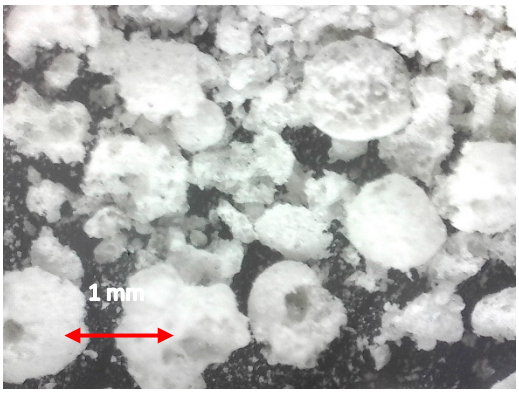

Medium Poraver – 400 kPa – LSDS

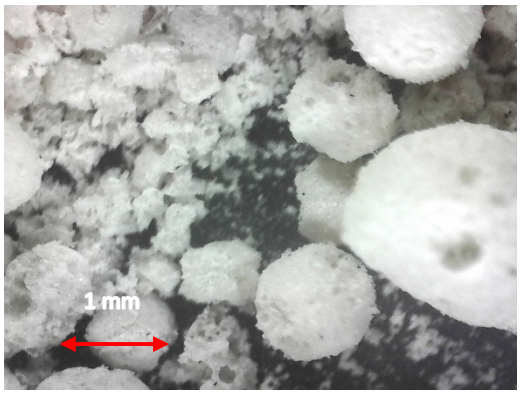

Medium Poraver – 500 kPa – LSDS

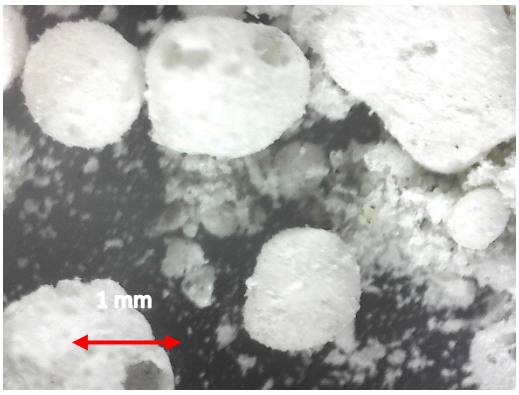

Medium Poraver – 600 kPa – LSDS

Appendix D – Cyclic Direct Shear Results

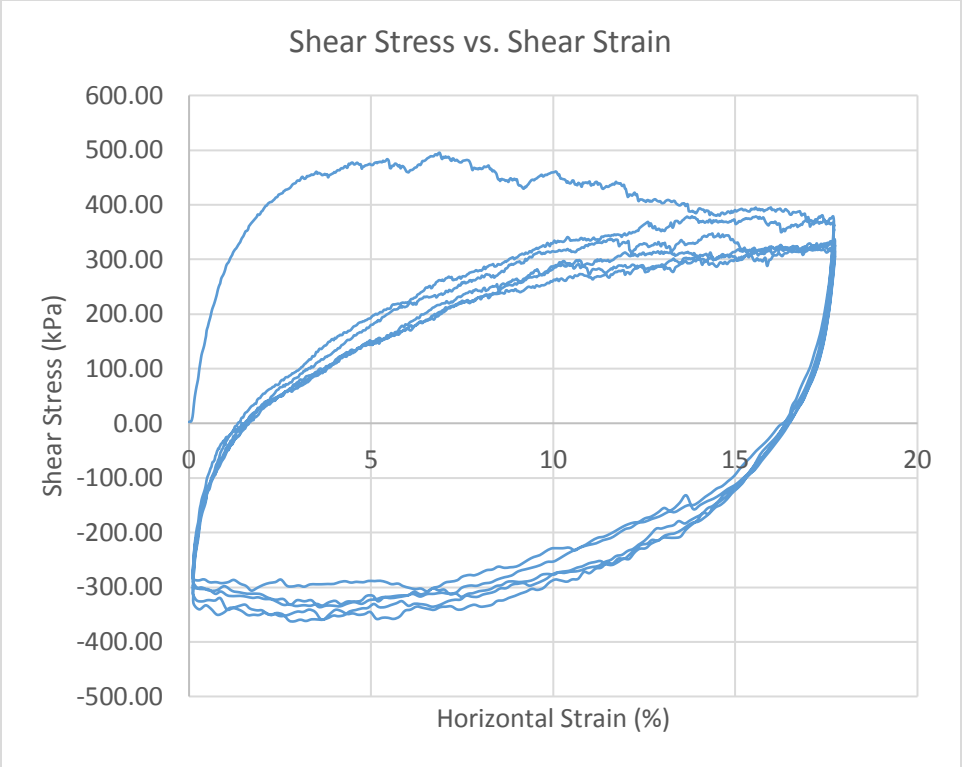

Coarse Kling – 400 kPa – Cyclic SSDS

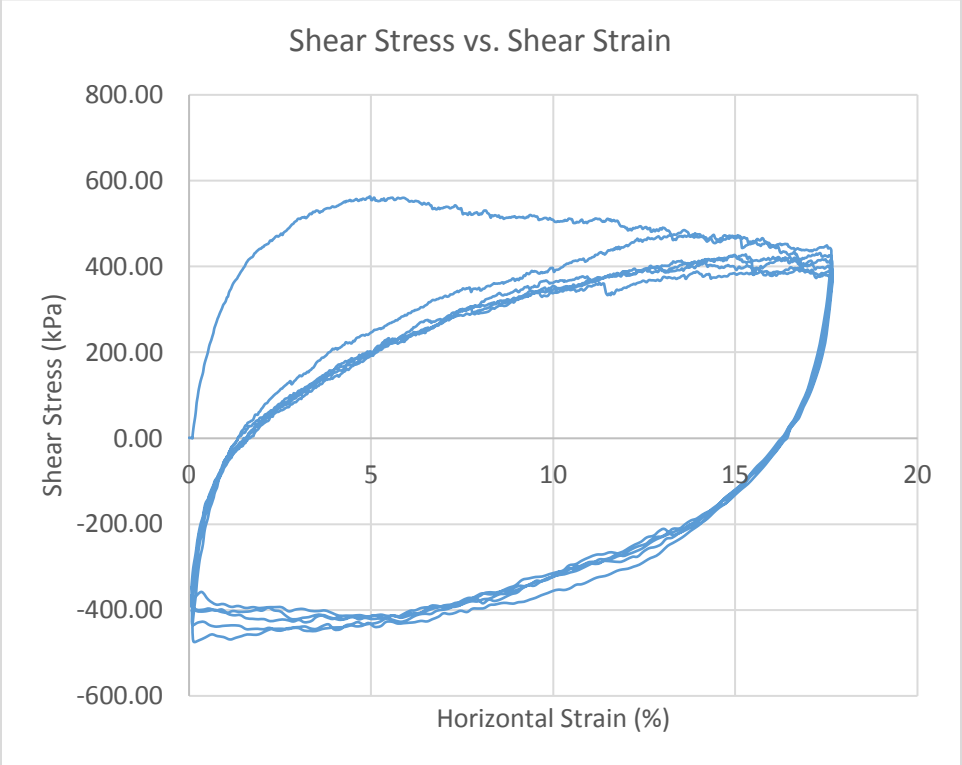

Coarse Kling – 500 kPa – Cyclic SSDS

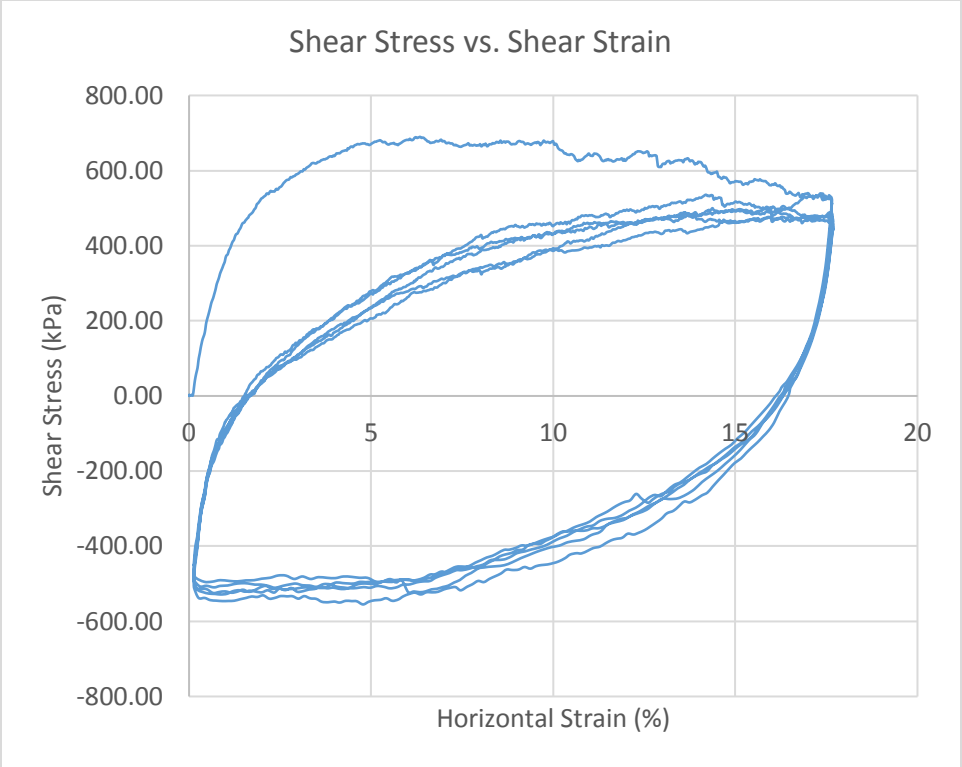

Coarse Kling – 600 kPa – Cyclic SSDS

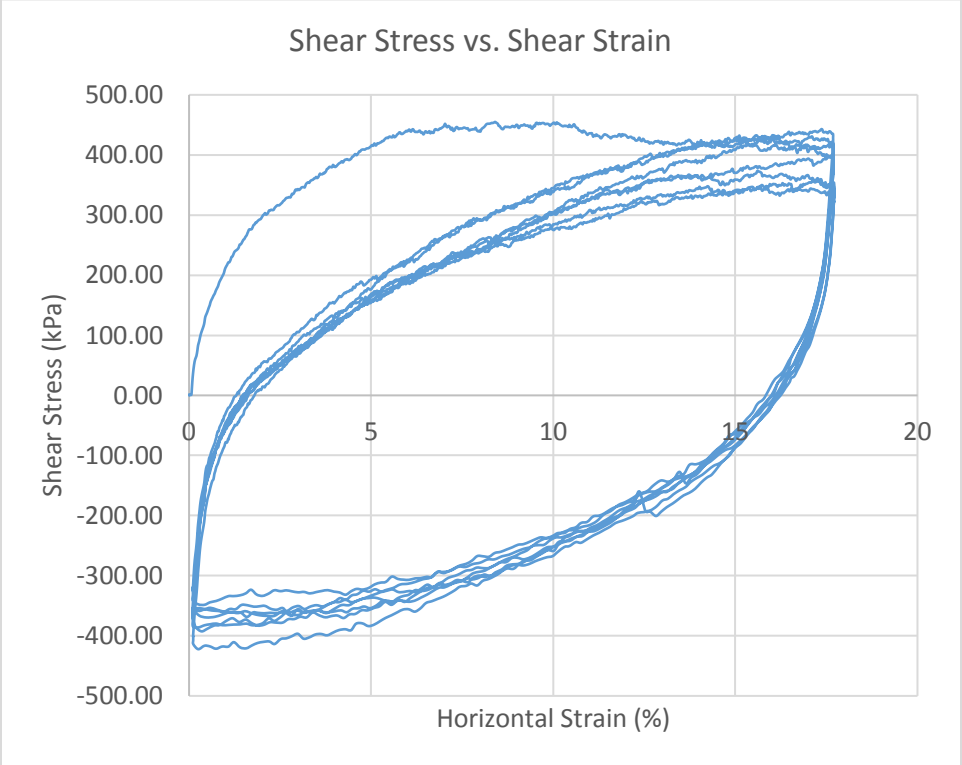

Coarse Limestone – 400 kPa – Cyclic SSDS

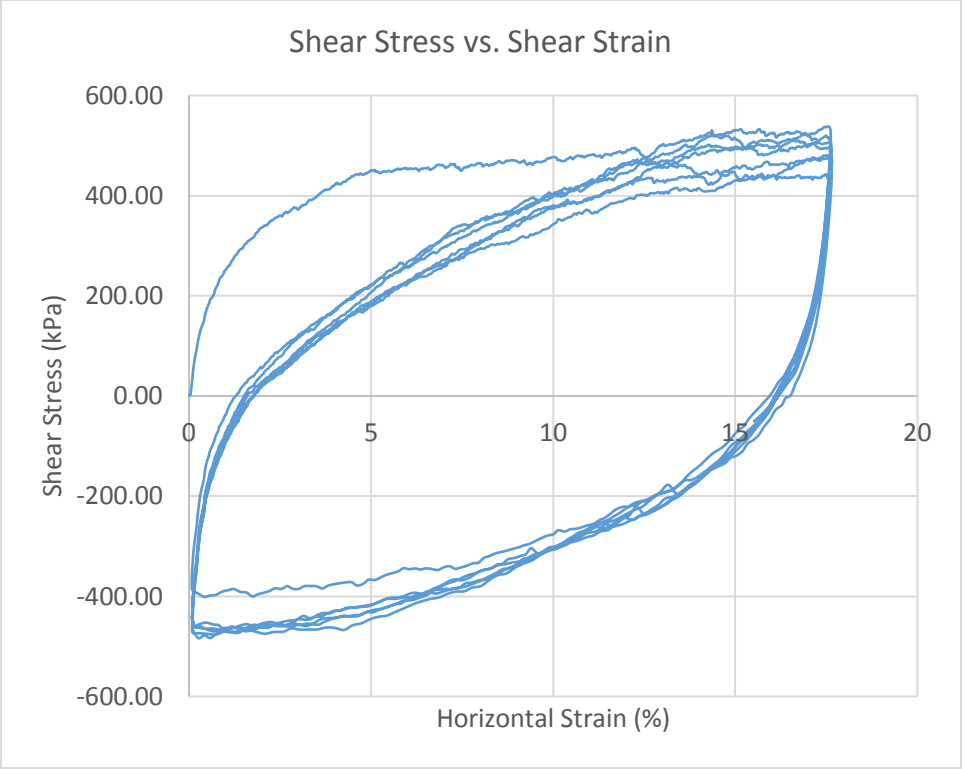

Coarse Limestone – 500 kPa – Cyclic SSDS

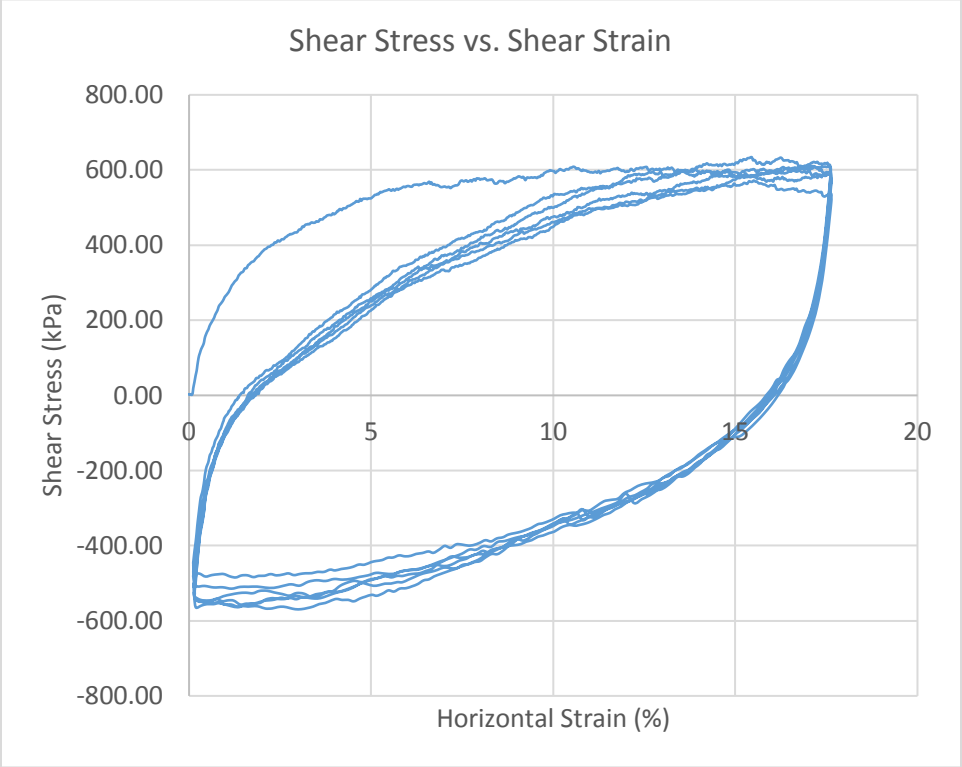

Coarse Limestone – 600 kPa – Cyclic SSDS

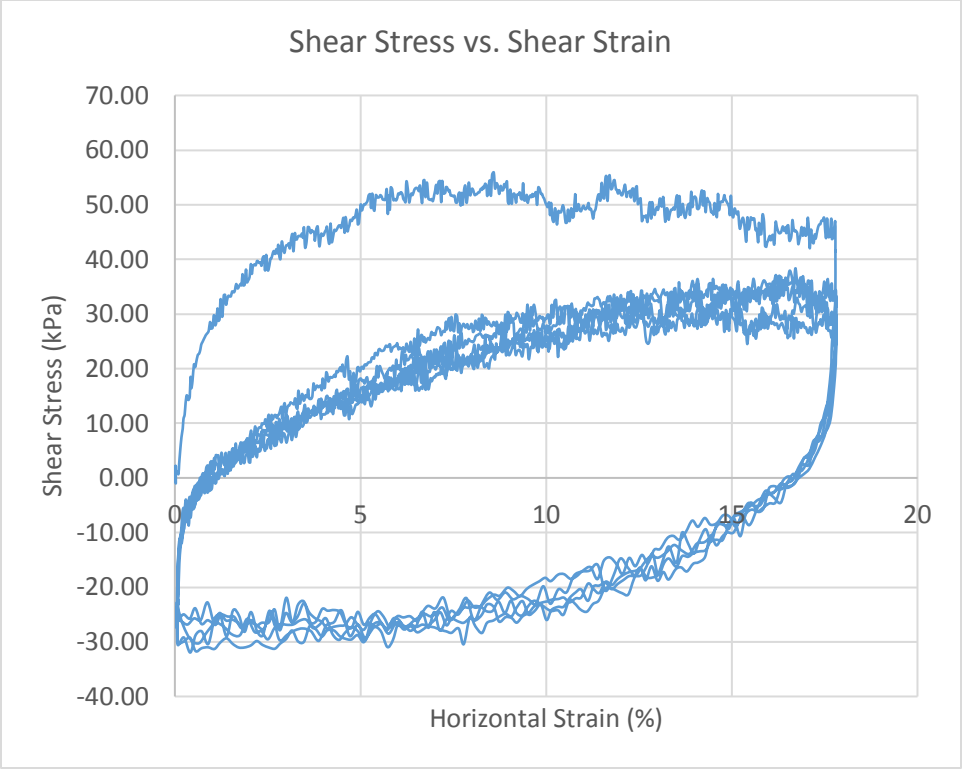

Coarse Limestone – 25 kPa – Cyclic SSDS

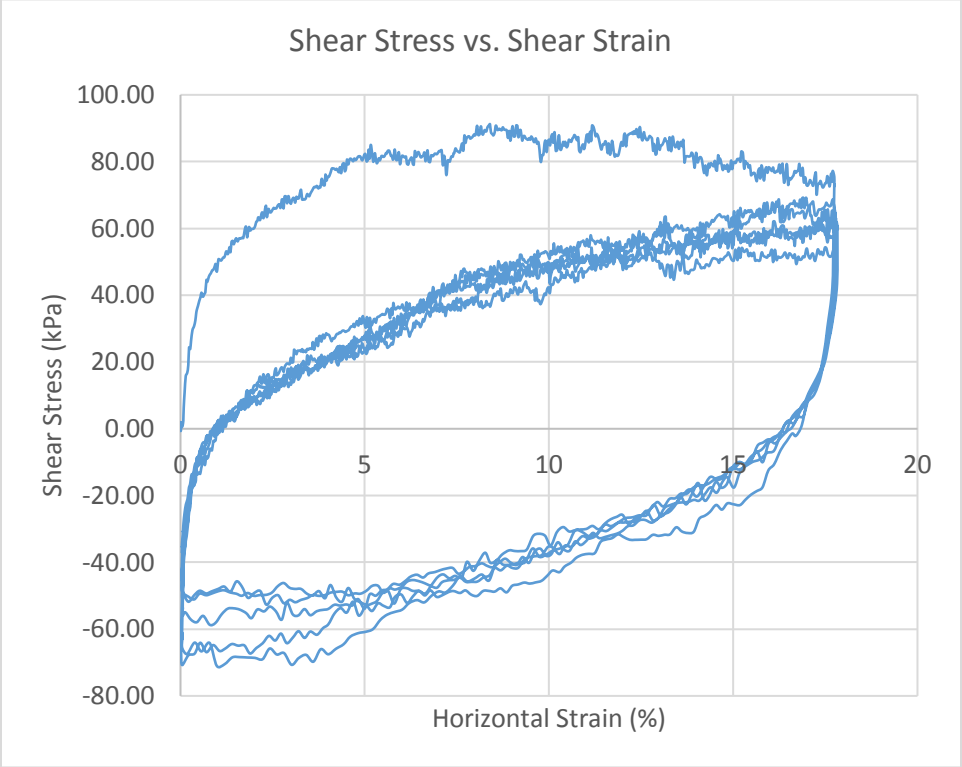

Coarse Limestone – 50 kPa – Cyclic SSDS

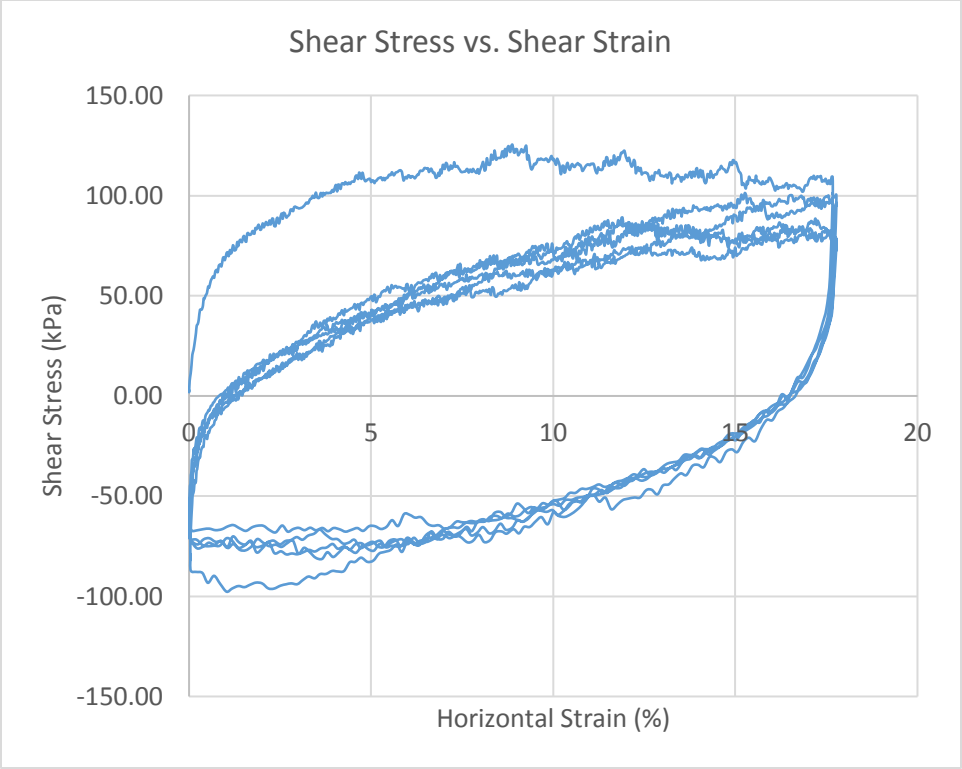

Coarse Limestone – 75 kPa – Cyclic SSDS

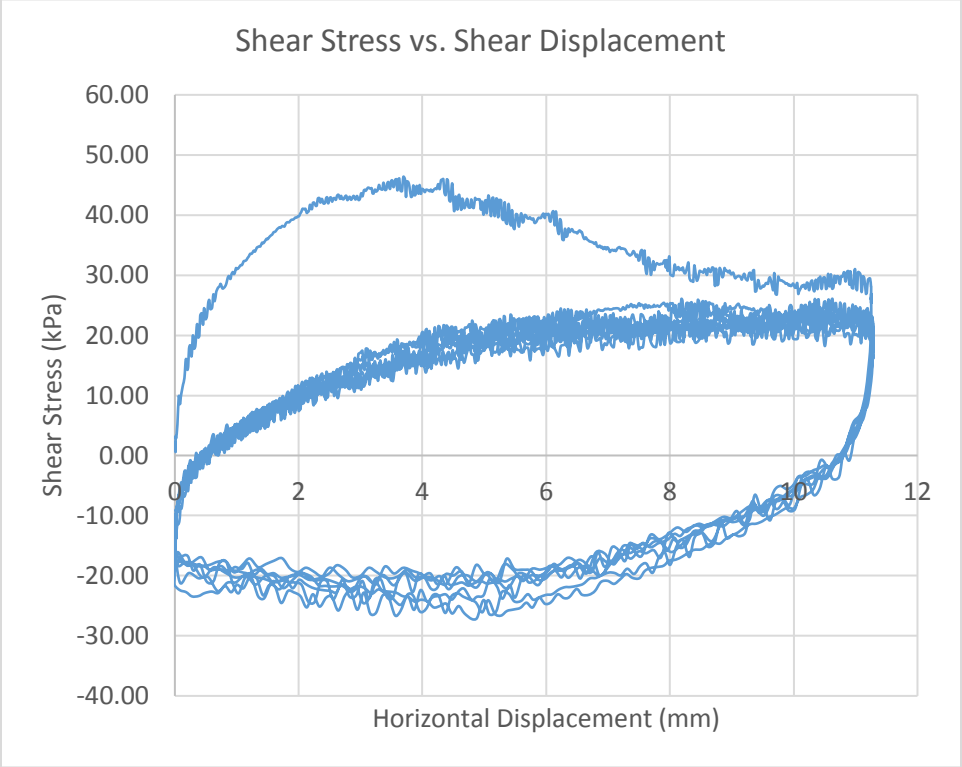

Coarse Poraver – 25 kPa – Cyclic SSDS

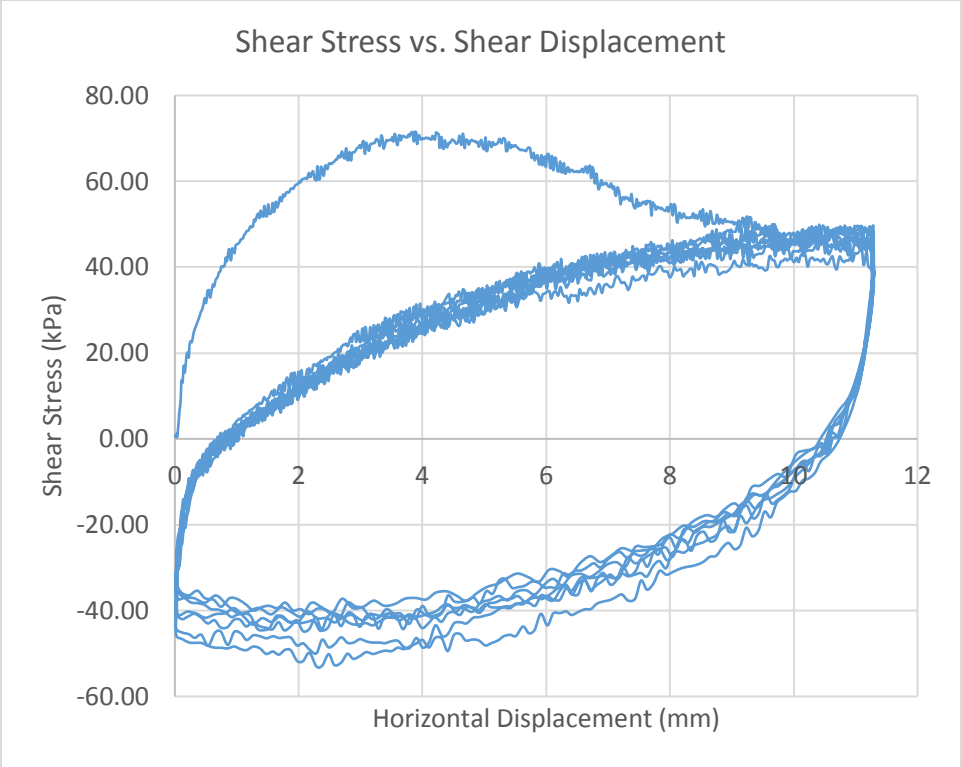

Coarse Poraver – 50 kPa – Cyclic SSDS

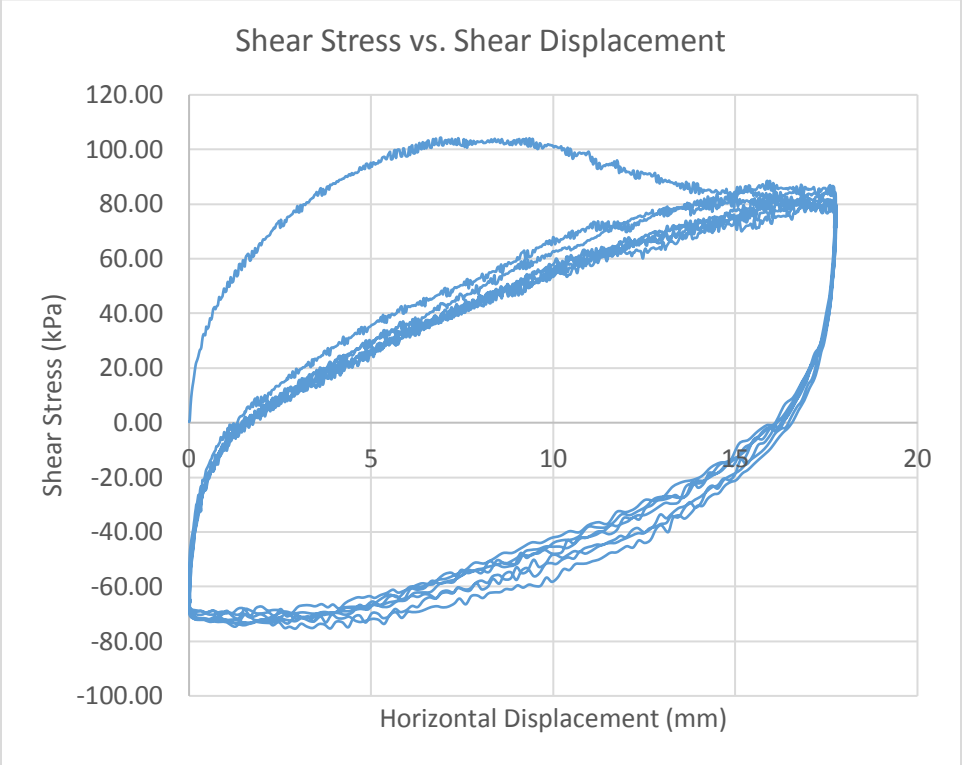

Coarse Poraver – 75 kPa – Cyclic SSDS

Appendix E – Top Cap Rotation Results

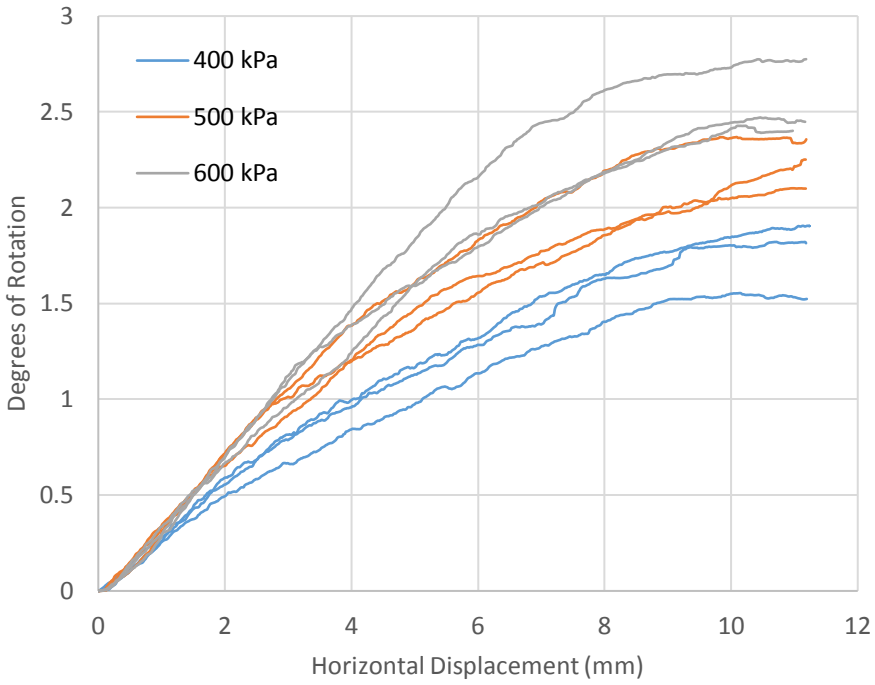

Coarse Kling – High Load – SSDS

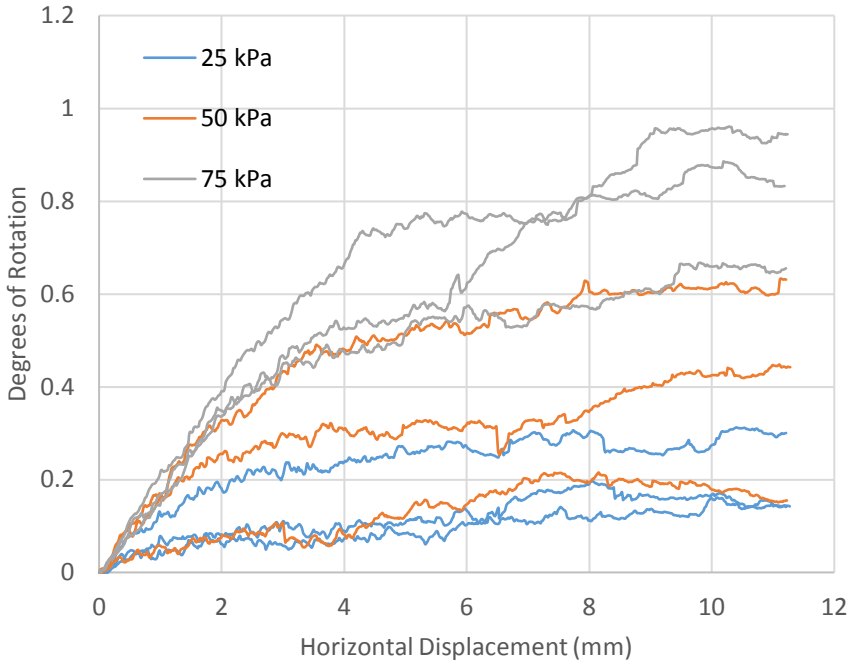

Coarse Kling – Low Load – SSDS

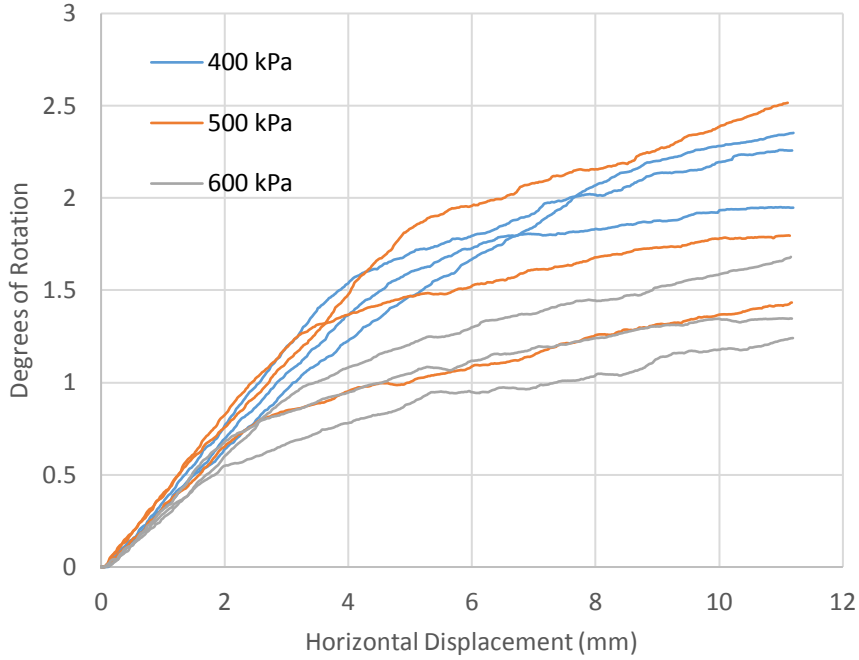

Coarse Limestone – High Load – SSDS

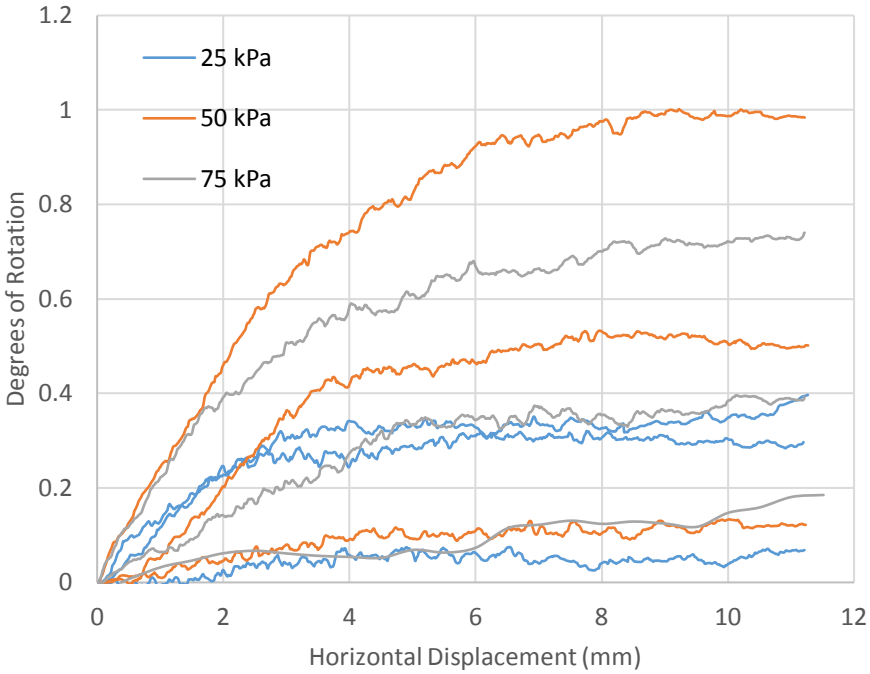

Coarse Limestone – Low Load – SSDS

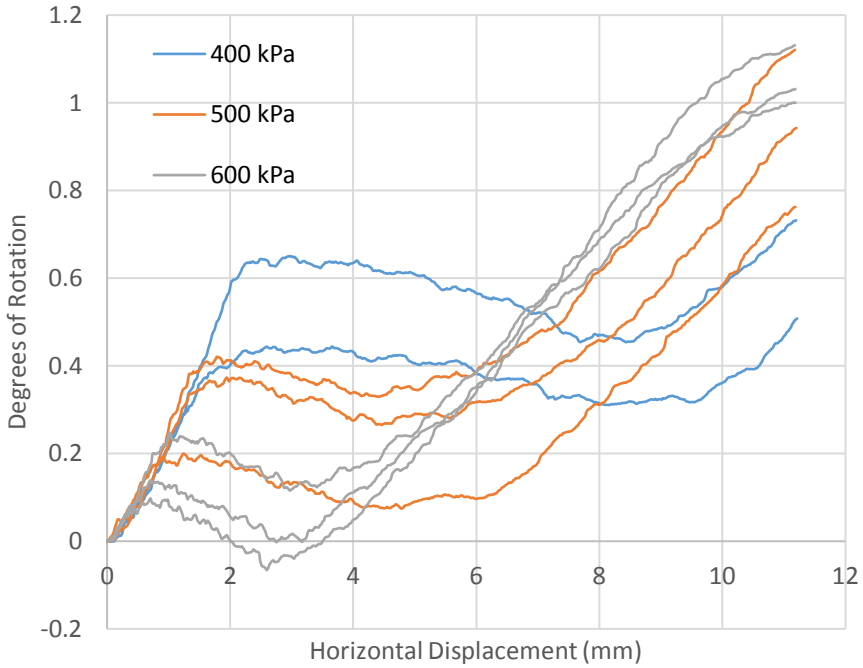

Coarse Poraver – High Load – SSDS

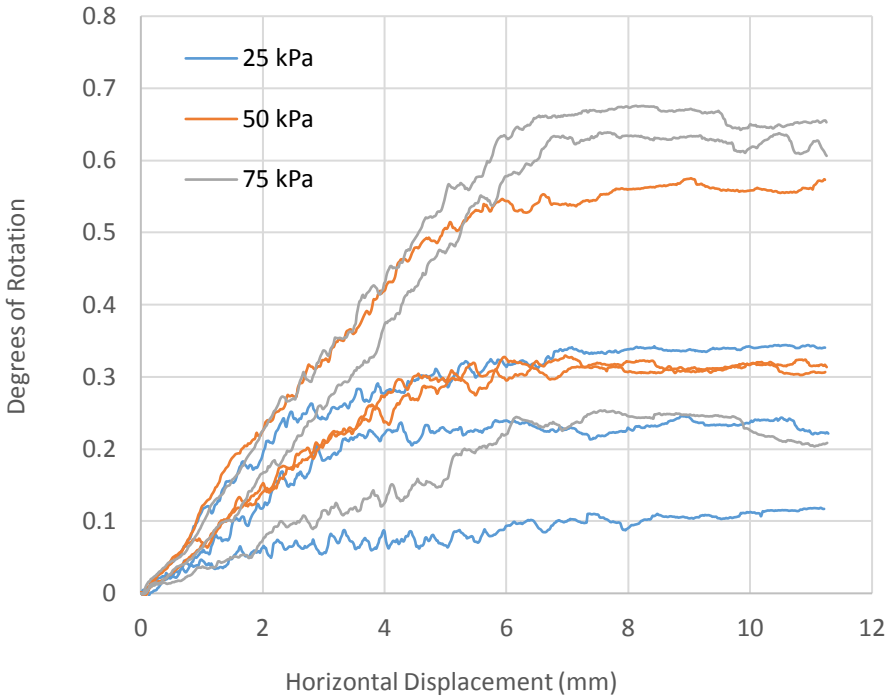

Coarse Poraver – Low Load – SSDS

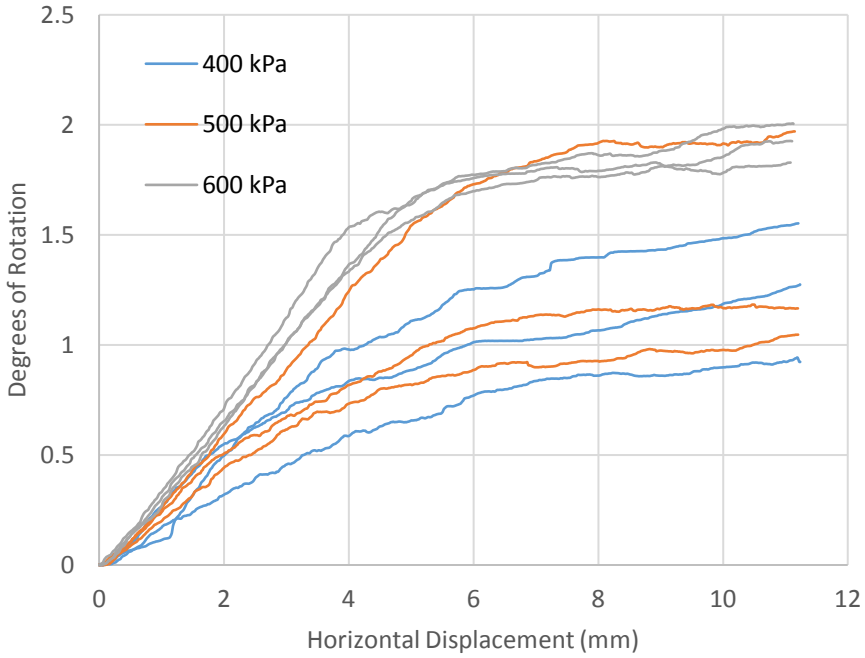

Medium Kling – High Load – SSDS

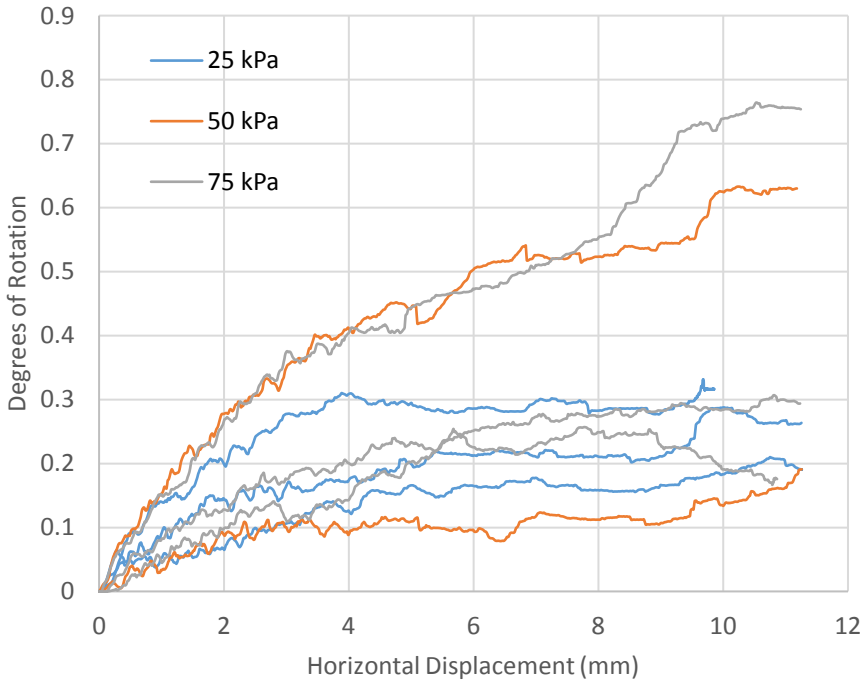

Medium Kling – Low Load – SSDS

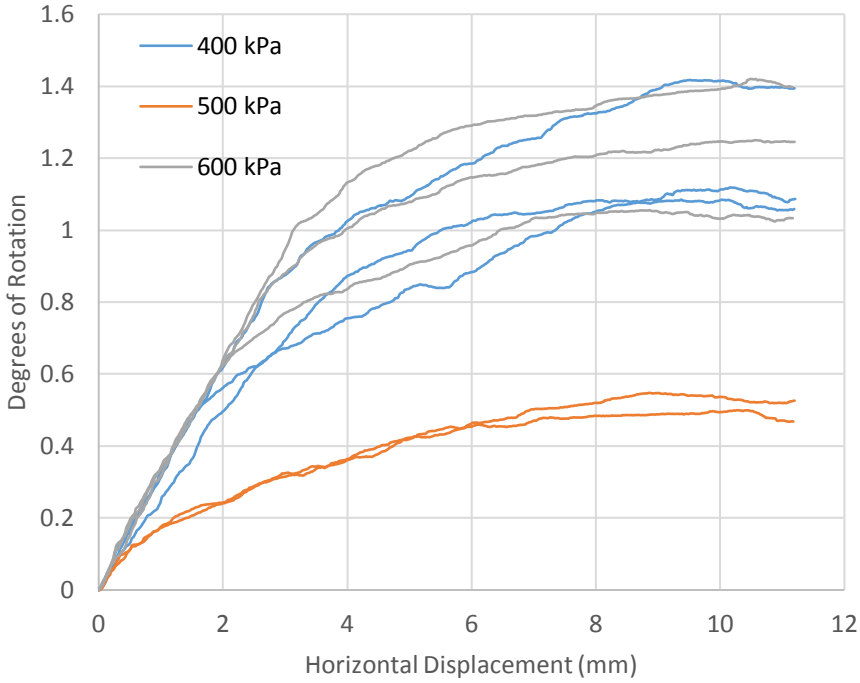

Medium Limestone – High Load – SSDS

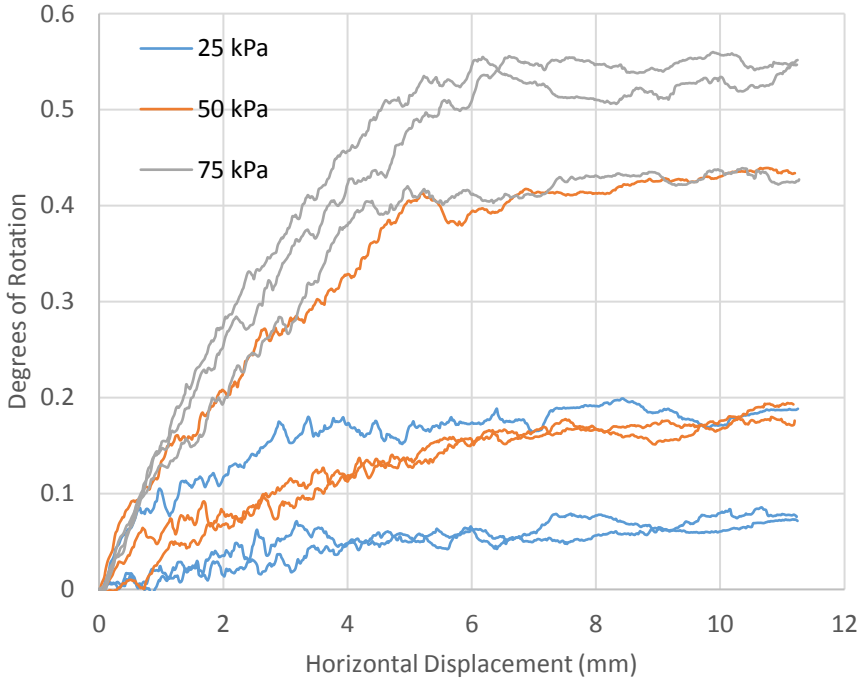

Medium Limestone – Low Load – SSDS

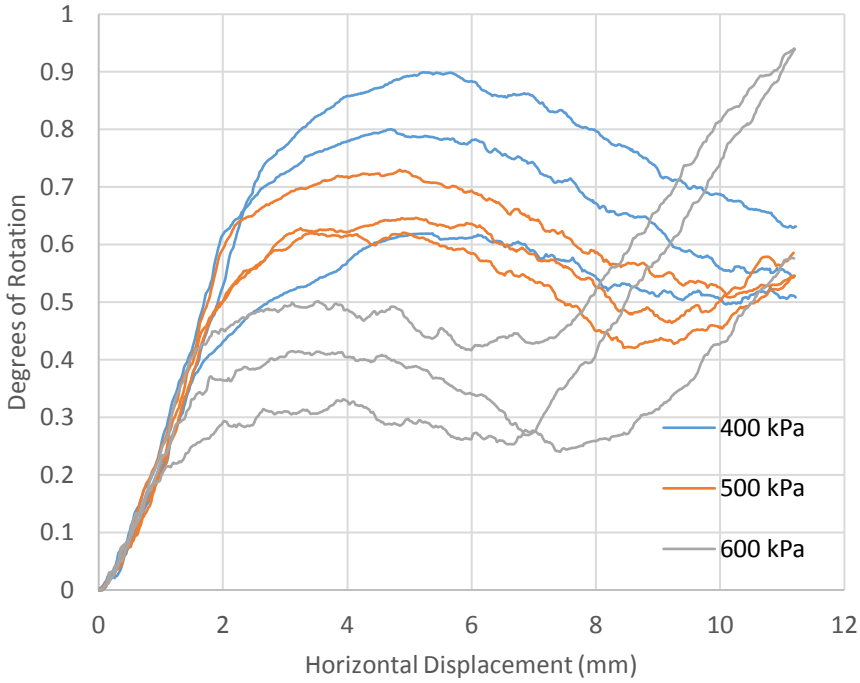

Medium Poraver – High Load – SSDS

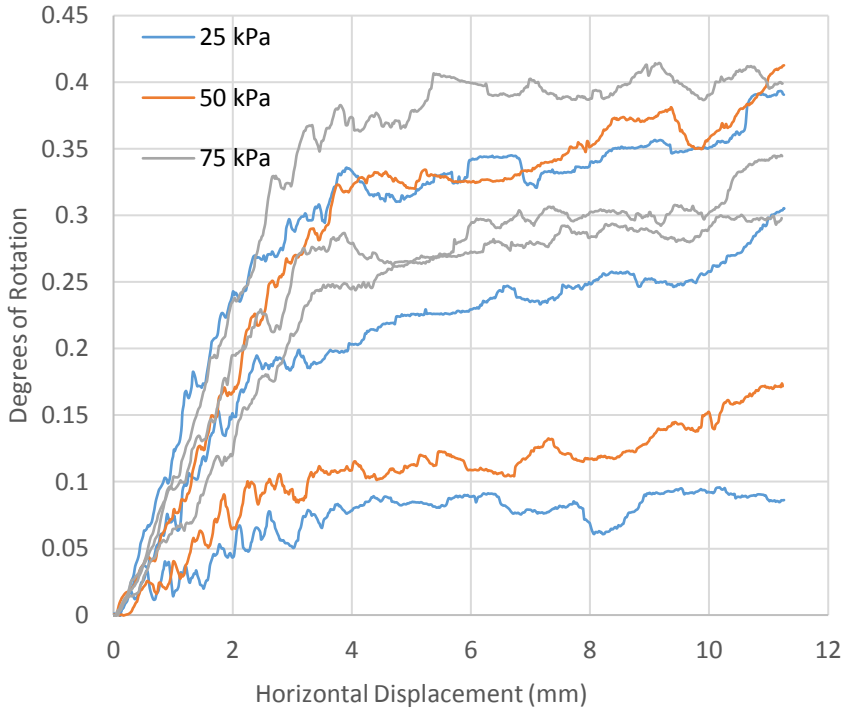

Medium Poraver – Low Load – SDSS

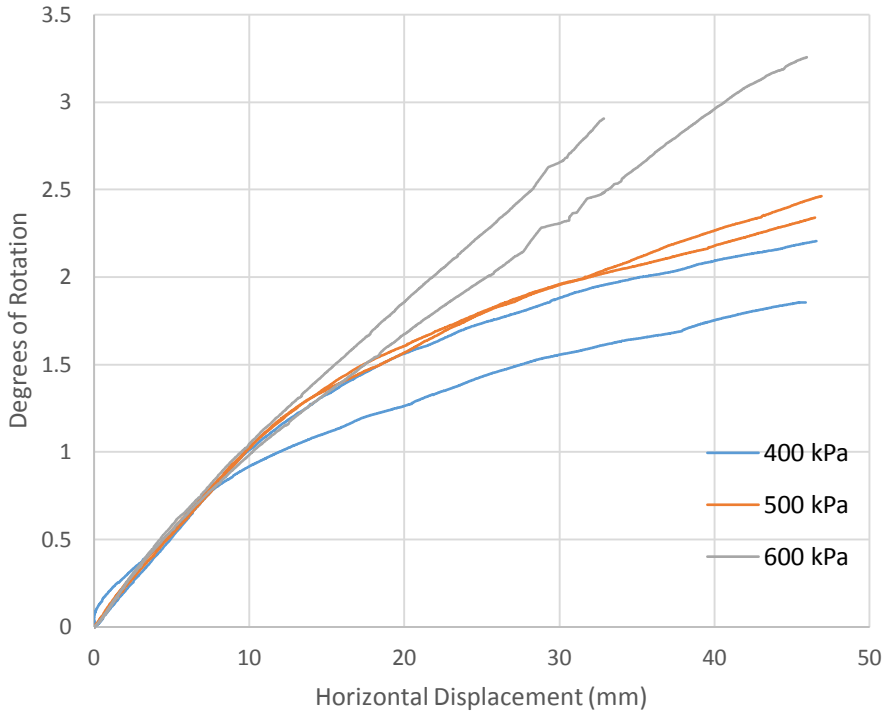

Coarse Limestone – High Load – LSDS

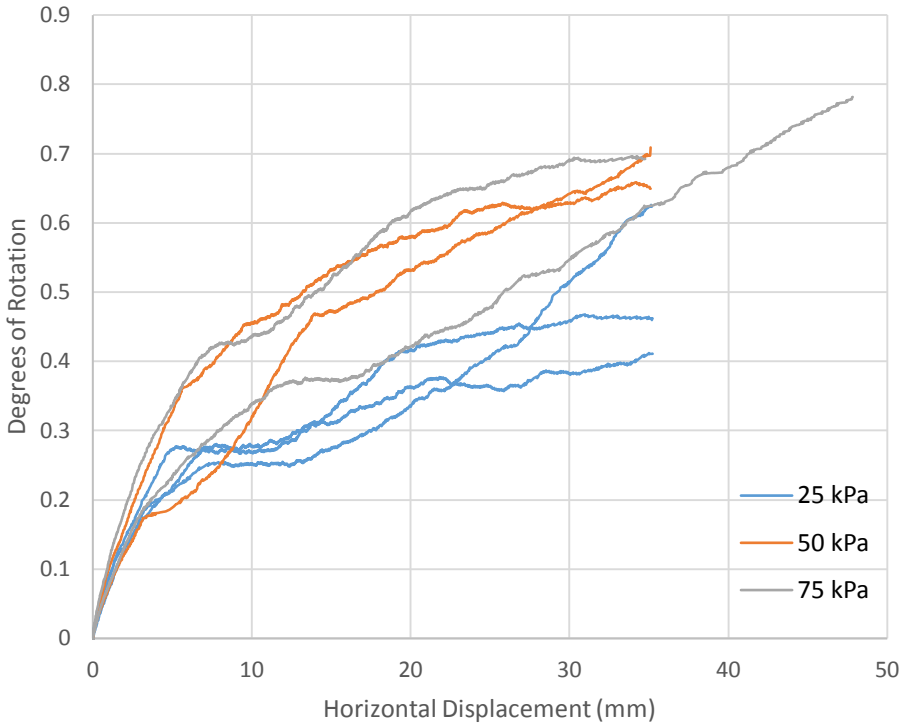

Coarse Limestone – Low Load – LSDS

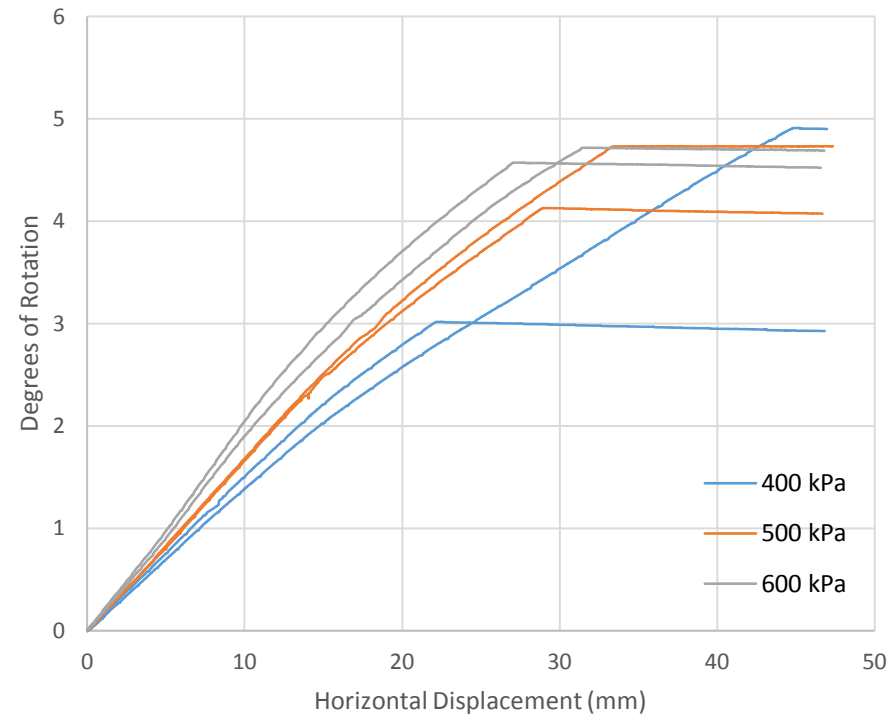

Coarse Poraver – High Load – LSDS

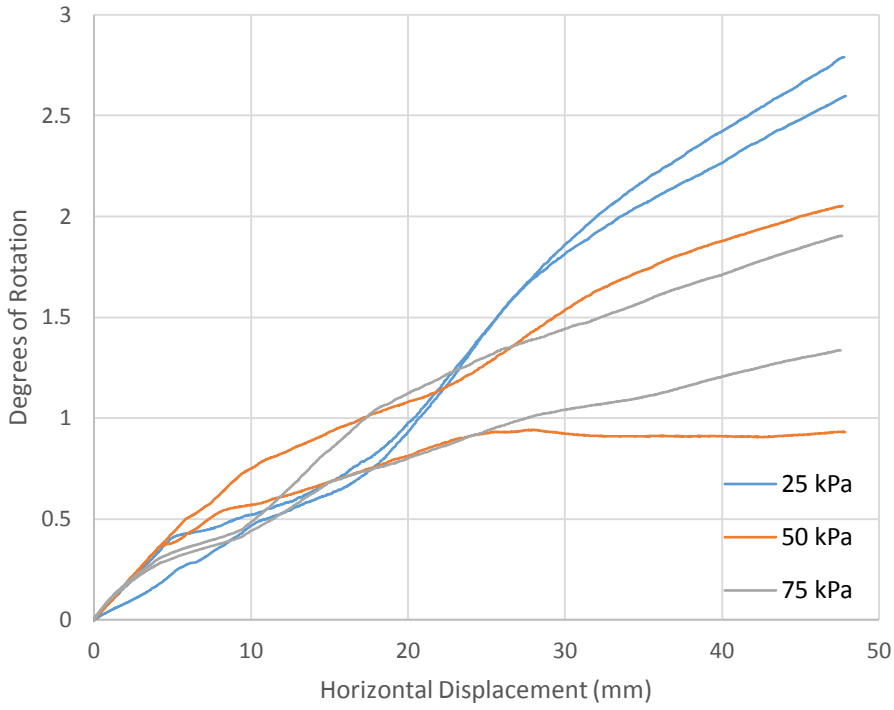

Coarse Poraver – Low Load – LSDS

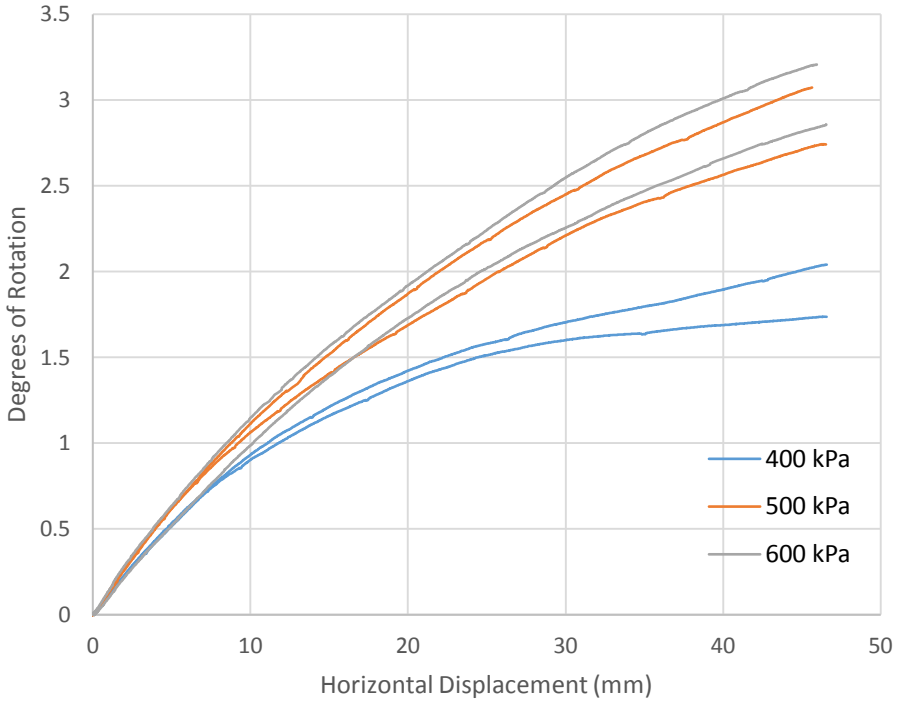

Medium Limestone – High Load – LSDS

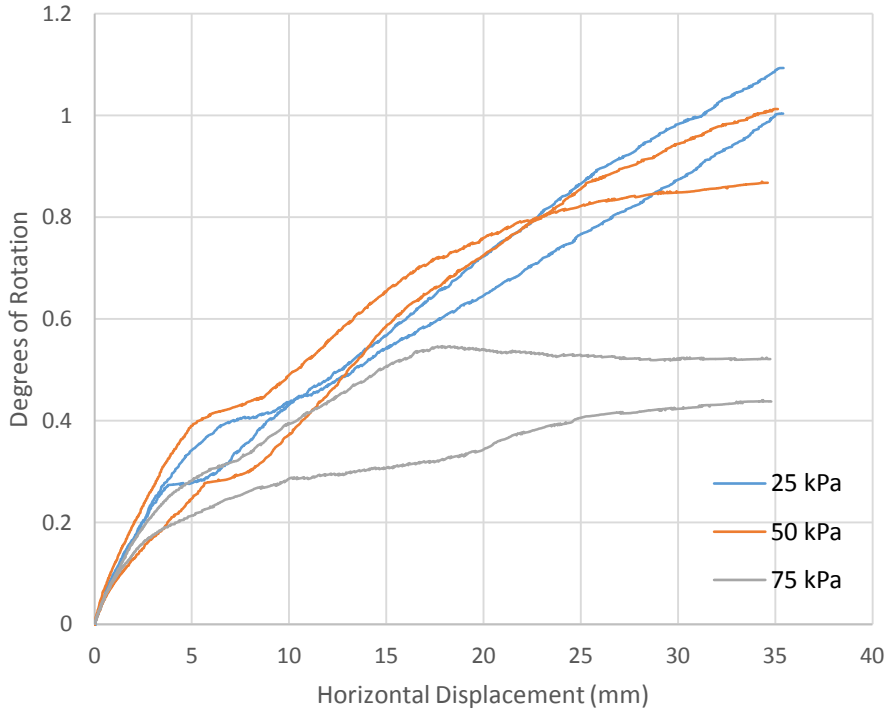

Medium Limestone – Low Load – LSDS

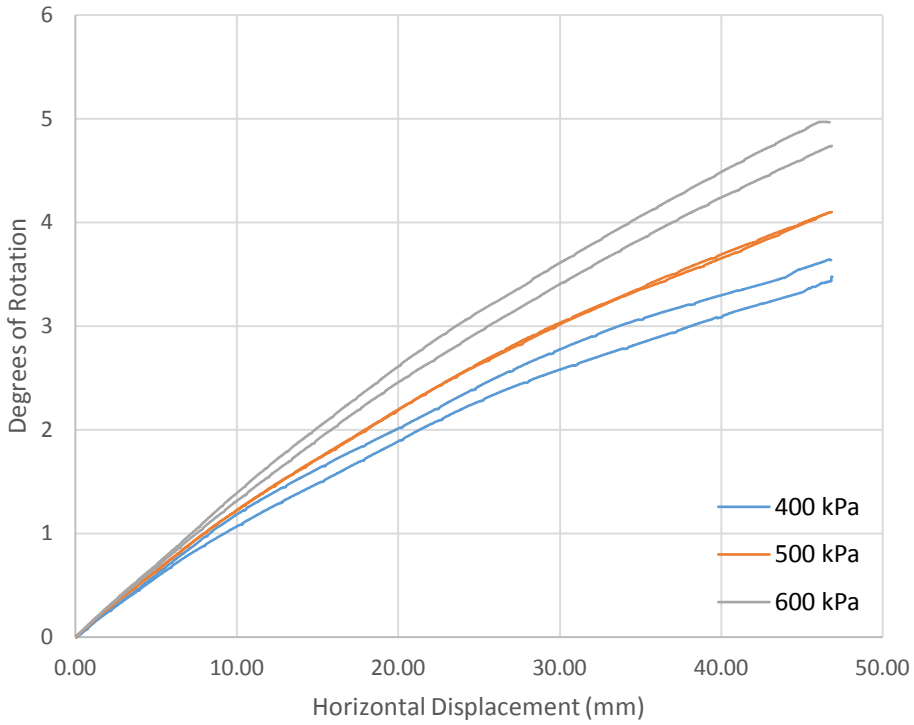

Medium Poraver – High Load – LSDS

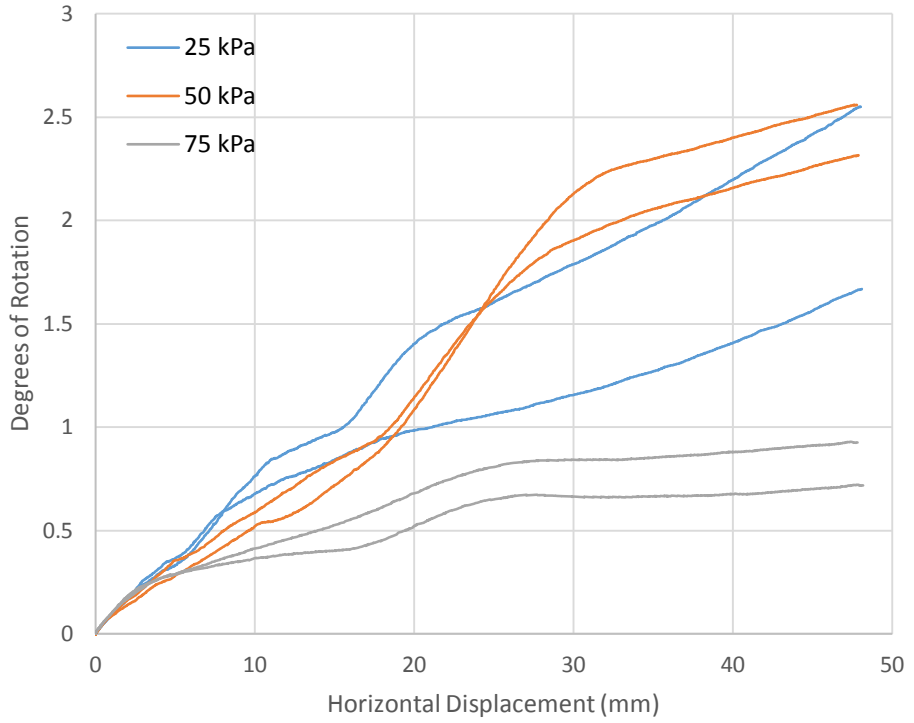

Medium Poraver – Low Load – LSDS